III International Symposium

TOPICAL PROBLEMS OF BIOPHOTONICS

OPTICAL BIOIMAGING

Chairs

Karsten König
Saarland University, Germany

Natalia Shakhova
Institute of Applied Physics RAS, Nizhny Novgorod Medical Academy, Russia

Bruce Tromberg
Beckman Laser Institute and Medical Clinic, UC Irvine, USA

Program Committee

Peter Andersen, Technical University of Denmark, Dept. of Photonics Engineering, Denmark

Stefan Andersson-Engels, Lund University, Sweden

Johannes de Boer, VU University Amsterdam, The Netherlands

Valentin Gelikonov, Institute of Applied Physics RAS, Russia

Jorge Ripoll, Institute of Electronic Structure & Laser – FORTH, Greece

Valery Tuchin, Saratov State University, Russia

FLOW MONITORING WITH LASCA

D.N. Agafonov[1], **P.A. Timoshina**[1], **M.A. Vilensky**[1], **I.V. Fedosov**[1], and **V.V. Tuchin**[1,2]

[1] Saratov State University, AgafonovDmitry@gmail.com
[2] Institute of Precise Mechanics and Control RAS

Introduction

Laser speckle imaging for monitoring the blood flow in living tissues can be used as a diagnostic tool for various medical applications [1]. The non-scanning technique proposed in 1996 by J. David Briers *et al.* [2] (referred to Laser Speckle Contrast Analysis or LASCA) and its subsequent variations and enhancements show great opportunity for real-time morpho-functional analysis of microcirculation and its dynamics. Nevertheless, speckle contrast imaging is known to be a more qualitative rather than quantitative tool as denoted by [2], [3] and many others.

Prospects for absolute flow speed mapping in LASCA are discussed in this work. Results of experimental study of flow monitoring in phantom and live subject are presented.

Discussion and Results

Unlike Doppler methods, speckle contrast techniques are known for their better time resolution and less resource utilization during analysis. Real-time spatial mapping of contrast values can be performed with general modern PC hardware and can be proposed for clinical use. However, exact values for microcirculation parameters such as absolute blood flow speed or perfusion cannot be obtained due to many uncertainties and errors involved at the measurement and processing stages [3]. Calculated contrast values are commonly represented in arbitrary units and even relative changes in flow parameters cannot be referenced in real-world units.

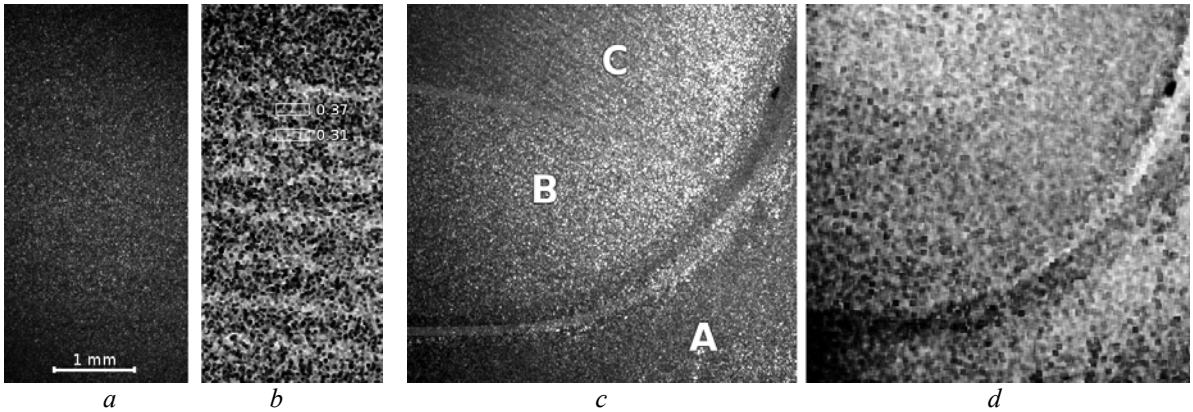

a *b* *c* *d*

Fig. 1. Example speckle patterns and corresponding spatial LASCA images for phantom (*a*, *b*) and human finger nail bed (*c*, *d*). Calculated contrast images (lighter – lower contrast) reveal inner channels of phantom (*b*) with moving particles immersed into scattering composition and areas with different blood perfusion of nail bed (*d*)

One of the intuitive ways to turn the discussed method into quantitative tool is to use calibration under controlled conditions of speckle pattern formation, registration of intensity distribution and further processing. Phantom, specially crafted to reproduce optical and functional properties of living tissues, was used to test the calibration method and to investigate the effect of various conditions on measured speckle images and calculated contrast. Figure 1 (*a*, *b*) shows a sample single image of speckle pattern and directly calculated contrast values obtained in these experiments. Figure 1 (*c*, *d*) shows the same images for human finger nail. Both results are obtained using Basler A602f monochrome CMOS camera with custom software made with National Instruments LabVIEW 8.5, which was created to perform real-time spatial LASCA studies. Proper camera operation parameters and lighting conditions were investigated to ensure repeatability of results and to avoid unnecessary influences.

Final calibration profiles for a wide flow speed range measured with different camera exposure times are presented in Fig. 2. Comparison with contrast values obtained for live tissue (finger nail bed capillaries) gave good agreement for speed ranges of actual microcirculation we got via subsequent microscopic studies performed in the same conditions (0.2 – 1 mm/s).

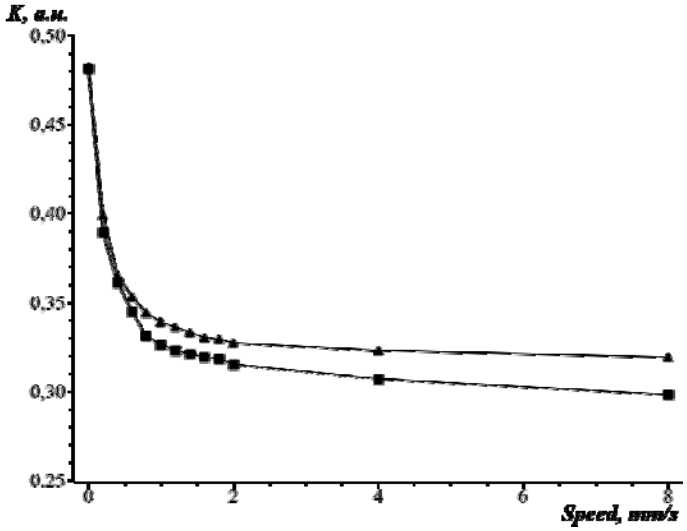

Fig. 2. Calibration profiles of contrast *K* as a function of flow speed measured with phantom for different camera exposure times: ▲ – 10 microseconds; ■ – 5 microseconds

Optical clearing (Fig. 3) also was tested to lower the effects of multiple scattering and other factors on calculated LASCA data, but show no significant difference in preliminary study of flow dynamics.

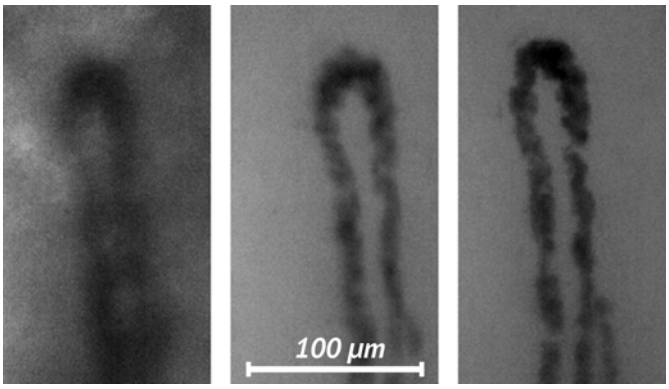

a *b* *c*

Fig. 3. Nail fold capillary loop: *a* – dry skin, *b* – 1 min after clearing agent applied, *c* – 1 hour after application

The study shows the possibility of using calibration for LASCA technique to obtain absolute values for blood flow speed and its dynamics. Unfortunately, this involves many restrictions and leads to the need of strong control over various conditions, which might be hard to achieve in clinical practice.

Acknowledgements

The research has been made possible by the following grants: RFBR #09-02-01048-a, #224014 PHOTONICS4LIFE of FP7-ICT-2007-2, Projects #1.4.09, #2.1.1/4989 and #2.2.1.1/2950 of the RF Ministry of Education and Science, RF Governmental contracts 02.740.11.0484, 02.740.11.0770, and 02.740.11.0879. The authors are grateful to Vladislav Lychagov *et al.* (Research-Educational Institute of Optics & Biophotonics) for providing the tissue phantom and Elina Genina (Chair of Optics and Biophotonics at Saratov State University) for help with techniques of optical clearing of tissues.

References

1. D.A. Boas and A.K. Dunn, *J. Biomed. Opt.*, 2010, **15**(1), 011109.
2. J.D. Briers, S. Webster, *J. Biomed. Opt.*, 1996, **1**(2), 174–179.
3. D.D. Duncan and S.J. Kirkpatrick, *J. Opt. Soc. Am. A Opt. Image Sci. Vis.*, 2008, **25**(8), 2088–2094.

THE EFFECT OF BIOTISSUE DEFORMATION ON OCT IMAGE CONTRAST

P.D. Agrba[1,2], **E.A. Bakshaeva**[2], and **M.Yu. Kirillin**[1]

[1] Institute of Applied Physics Russian Academy of Sciences, Nizhny Novgorod, Russia
agrbapd@gmail.com
[2] Lobachevsky State University of Nizhny Novgorod

1. Introduction

Improvement of methods of structural and functional visualization of processes in biotissues is a topical problem of diagnostics and treatment control of various diseases [1, 2]. Optical coherence tomography (OCT) is an imaging modality with high spatial resolution meeting the requirement for noninvasiveness, which is necessary for monitoring biological processes. OCT is based on principles of low coherence interferometry for imaging the inner structure of superficial tissues at depths up to several mm [3–5].

Light scattering in biotissue depends on the features of structure, as well as on external conditions such as additional pressure and application of clearing or contrasting agents. Thus, an OCT image is sensitive to biotissue compression degree and presence of various agents. Controlling the optical properties of biotissue allows one to extract additional information from the OCT image. In this work we present a technique for controlling scattering and absorption properties of biotissue by mechanical deformation.

2. Materials and methods

The objects under study are *in vivo* human thin skin samples. Design of the OCT probe developed at IAP RAS provides a possibility for controlled compression of the sample combined with simultaneous imaging. An OCT-probe was placed in a special holder allowing to control the force of pressure on the studied object and keep it constant. Then, the probe was pressed to human skin and was held in such position for 8–10 minutes, while the OCT-images of the studied object were acquired continuously with the rate of 1 image each 5 seconds. The acquired OCT-images were stored for further processing and analysis. We distinguish low and high pressure due to volunteers' sensation. Low compression (about 0.06 N/mm^2) provides full contiguity of probe surface with studied biotissue and does not induce any unpleasant feelings of a volunteer. High compression (about 0.27 N/mm^2) also provides full contiguity, but induces some unpleasant feelings. At the same time, the hemorrhage formation should be excluded for both pressures to keep non-invasiveness of the diagnostic process. At the next stage, we add biotissue stretching to the compression. We consider three age groups of volunteers with average ages of 23, 29 and 48 years.

3. Results and discussion

Figure 1 demonstrates an increase of OCT-signal level in dermis associated with larger compression of this layer compared to the upper-lying stratum corneum and epidermis and consequent increase in its scattering coefficient resulting in the epidermis-dermis junction contrast increase.

The applied pressure induces contrast increase for all volunteers. For the case of low pressure for younger volunteers (23 and 29 years old) the contrast almost reaches its maximum of 17 dB in 3 minutes and oscillates about this value in the remaining time of the observation. For the elder volunteer (48 years old) a monotonous, almost linear, an increase of contrast was observed during the whole observation time

High pressure at the initial stage induces contrast increase similar to the previous case, however, for three volunteers time dependences differ qualitatively. For a 23-years old volunteer the contrast increase was monotonously reaching 14 db at the end of observation time, which is slightly lower compared to the contrast value obtained in the low pressure case. A 29-year-old volunteer demonstrated dynamics very similar to that of the low pressure case: the maximal value of 16 db was reached 3 minutes after the start of compression and was kept constant with slight deviations during the rest of observation time. For a 48-year-old volunteer the contrast value reached its maximum of 18 dB about 3 minutes after the start of compression. At the same time, the OCT-images for this volunteer demonstrate dramatic changes in the structure of the OCT-image by appearance of dark areas after definite time since compression start (Fig. 1c). These areas exhibit high-contrast boundaries

and are associated with interstitial or intracellular water inflow to the region of scanning which may also cause a decrease in contrast.

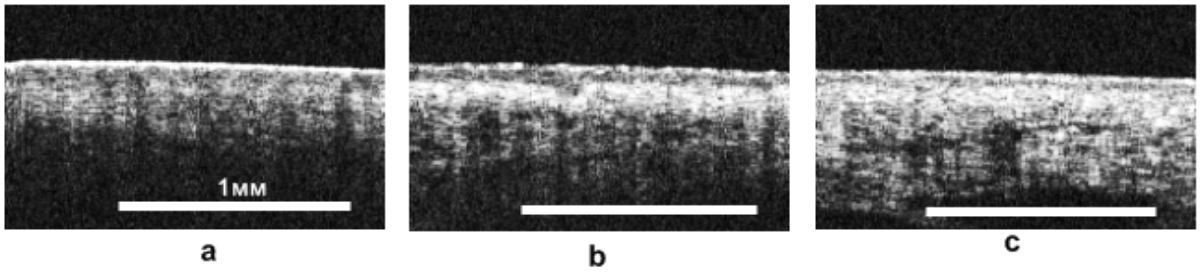

Fig. 1. OCT-images of thin skin of 48-year-old male volunteers immediately after compression start (a), in 3 min. (b), and in 6 min. (c) for high pressure case

For the case when high compression was combined with transversal deformation we observed a decrease of contrast of epidermis-dermis junction for transversal squeeze and its increase for transversal stretch (fig 2). The values of contrast in the case of high compression without transversal deformation were used as a reference.

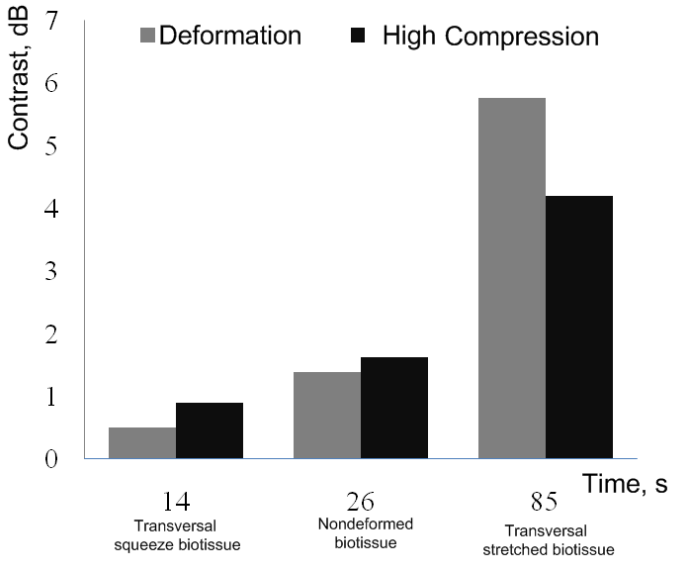

Fig. 2. Comparing OCT-images of thin skin of high compression case and high compression with deformation

Acknowledgements

The work was supported by grants from the Russian Foundation for Basic Research (Nos. 10-02-00744, 10-08-00744 and 11-02-01129), the grant of the President of the Russian Federation MK-1127.2010.2, FTP "Scientific and Scientific-Educational Brainpower of Innovative Russia" (projects Nos. 14.740.11.0253, 02.740.11.0086, 02.740.11.0839), and grant of the Government of Russian Federation No. 11.G34.31.0017.

References

1. M. Ghosn, V.V. Tuchin, and K.V. Larin, *Optics Letters*, 2006, **31**, 2726-2733.
2. G. Vargas, A. Readinger, J.K. Barton, S.S. Dozier, and A.J. Welch, *Lasers in Surgery and Medicine*, 2002.
3. *Handbook of Optical Coherence Tomography*, Edited by B.E. Bouma, G.J. Tearney, New York: Marcel Dekker, 2002, 741 p.
4. V.M. Gelikonov, G.V. Gelikonov, L.S. Dolin, V.A. Kamensky, A.M. Sergeev, N.M. Shakhova, N.D. Gladkova, E.V. Zagaynova, *Laser Physics*, 2003, **13**(5), 692-702.
5. A.M. Sergeev, L.S. Dolin, and D.N. Reitze, *Optics & Photonics News*, 2001, 28-35.

STUDIES OF ANTI-HER2/neu IMMUNOTOXIN ANTINEOPLASTIC ACTIVITY ON FLUORESCENT TUMOR MODEL

I.V. Balalaeva[1,2], E.A. Malekhanova[1], N.Y. Lekanova[1], I.V. Krutova[1], A.A. Brilkina[1,2], O.A. Stremovsky[3], and **S.M. Deyev[1,3]**

[1] N.I. Lobachevsky State University of Nizhny Novgorod, Russia, irin-b@mail.ru
[2] Institute of Applied Physics, Russian Academy of Sciences, Nizhny Novgorod, Russia
[3] Institute of Bioorganic Chemistry, Russian Academy of Sciences, Moscow, Russia

Tumor models expressing fluorescent proteins have given rise to a number of fluorescence measurement techniques that allow quick and relatively inexpensive pharmacological studies. The methods using fluorescent proteins possess some advantages over other optical techniques [1]. These include:

– No additional substrates are needed. Protein chromophore is formed autocatalytically.
– High fluorescence intensity allows observation of active animals without anaesthesia.
– The metastases can be easily detected and visualized due to inheritance of protein gene by all tumor cells.
– *In vivo* imaging of tumors can be realized with rather simple equipment, and so on.

In the present study we have used the fluorescent tumor model to estimate the antineoplastic activity of immunotoxin binding to HER2/neu receptor, overexpressed by cells of many cancer types.

Materials and methods

Nude mice bearing subcutaneous human ovarian carcinoma expressing red fluorescent protein Katushka (SKOV-3-kat cell line) were used as a fluorescent experimental tumor model. Fluorescent protein Katushka (scientific name TurboFP635) is a homodimer with absorption peak at 588 nm (ε = 65000 $M^{-1}cm^{-1}$) and fluorescence maximum at 635 nm (quantum yield 0.34) [2].

SKOV-3 cells overexpress surface receptor HER2/neu. We have chosen this receptor as a molecular target for the therapy; in this connection HER2/neu expression by transfected SKOV-3-kat cells was tested both in vitro and *in vivo*.

We have tested the anticancer effect of intraperitoneal administration of immunoxin based on anti-HER2 4D5 scFv-antibody and Pseudomonas exotoxin (or exotoxin A) in comparison with platinum-containing drug Cisplatin, scFv-antibody or toxin itself. During tumor development the volumetric tumor measurements by external caliper as well as the monitoring by method of fluorescence imaging were conducted and the information value provided by two approaches was compared.

Whole-body images were obtained using a fluorescence imaging setup. Fluorescence was excited at 585 nm by LED and registered by high sensitivity CCD camera using 628 to 672 nm band-pass filter.

Results and conclusions

The fluorescence imaging approach is supposed to provide information about real amount of cancer cells in the tumor volume at the initial stage of tumor development until the tumor node shape is mostly flat. High sensitivity of the method allowed us to visualize the growth of nonpalpable tumors and metastases (Fig. 1).

As expected, the integral fluorescence intensity over tumor area correlated with tumor volume. At the same time, there was some discordance: after cell injection, tumor node steadily grew, while fluorescence could be strongly reduced and then rose again in several days. As tumor volume depends on cancer cells amount, host's stroma cells, matrix, and growth substrate used for injection, the fluorescence intensity is thought to be the more adequate parameter for tumor assessment.

The pronounced antitumor activity of immunotoxin tested has been demonstrated. The volumetric measurements revealed the difference between groups of animals starting from 59^{th}–74^{th} day (Fig. 2a). The coefficient of the tumor growth inhibition (CTGI) evaluated at 59^{th} day for "immunotoxin" group was about 60%. The efficacy of immutoxin was comparable with Cisplatin's one. The more slight antineoplastic effect has also been shown for scFv-antibodies.

The fluorescence imaging and subsequent calculation of integral fluorescence intensity of tumor made it possible to detect the therapeutic effect much earlier. At 17^{th} day of tumor development the coefficient analogous to CTGI but calculated on the basis of fluorescence was about 80% (Fig. 2b).

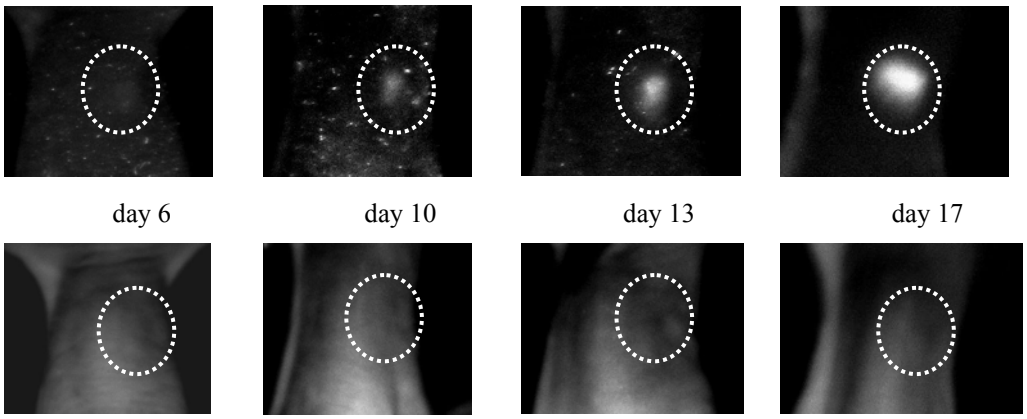

Fig. 1. Fluorescence (top row) and back-reflection (bottom row) images of the same animal 6 to 17 days after subcutaneous injection of SKOV-3-kat cells.
The tumor was nonpalpable up to the 17th day

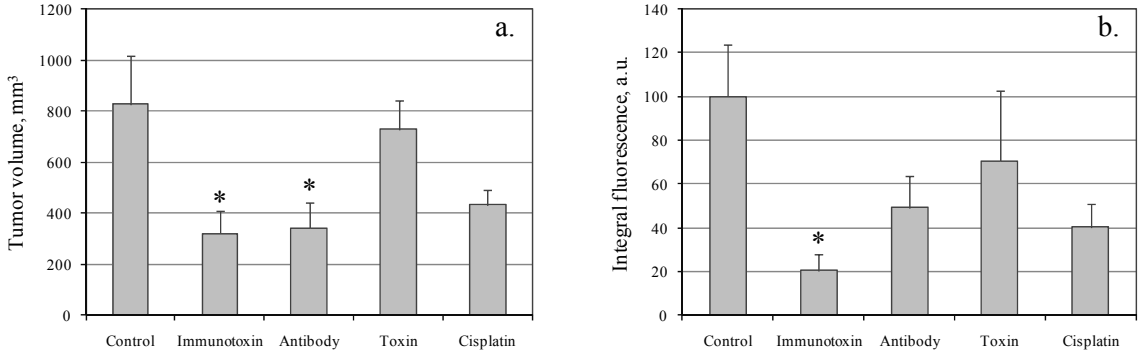

Fig. 2. Averaged tumor volume in different animal groups at 54th day of tumor development (a.) and integral fluorescence intensity in the same groups at 17th day (b.).
Statistically significant difference from the control group is indicated by asterisk

Thus, the antineoplastic activity of immunotoxin based on anti-HER2 scFv-antibody and Pseudomonas exotoxin has been demonstrated on the fluorescent tumor model. This effect is comparable with Cisplatin activity. Since the agents have different mechanisms of action, it might be supposed that their combination should be even more effective for tumor development inhibition. It should be noted that the fluorescent model allows revealing details of tumor growth at the earlier stages and with more accuracy.

Acknowledgements

This work was partly supported by the Ministry of Education and Science of the Russian Federation (project #02.740.11.0086), the Russian Foundation for Basic Research (project 11-02-00916-a), and the Program of RAS Presidium "Fundamental Sciences for Medicine".

References

1. R.M. Hoffman, *Nature Reviews*, 2005, **5**, 796-806.
2. D. Shcherbo, E.M. Merzlyak, T.V. Chepurnykh, et al., *Nature Methods*, 2007, **4**(9), 741-746.

Invited

ACCESS TO CUTTING EDGE IMAGING TECHNOLOGIES IN EUROPE

Y. Belyaev[1], A. Keppler[2], W. Hübner[3], R. Pepperkok[1,2], J. Ellenberg[2], and **C. Müller[3]**

[1] Advanced Light Microscopy Facility, EMBL, Meyerhofstr. 1, 69117 Heidelberg, Germany
belyaev@embl.de
[2] Cell Biology and Biophysics Unit, EMBL, Meyerhofstr. 1, 69117 Heidelberg, Germany
[3] Structural and Computational Biology Unit, EMBL, Meyerhofstr. 1, 69117 Heidelberg, Germany

Summary

Imaging technologies are an important part of any biological or medical research. The Advanced Light Microscopy Facility (ALMF) at the European Molecular Biology Laboratory (EMBL) in Heidelberg is a successful example demonstrating access possibilities to modern imaging technologies in Europe. Here, we also introduce two other European programs aiming to facilitate user access to the modern research infrastructure namely Euro-BioImaging and P-Cube.

ALMF

The ALMF (www.embl.de/almf/) offers state-of-the-art light microscopy equipment including high-throughput microscopy and accessory services. The facility was set up as cooperation between EMBL and industry to improve communication between users and producers of high-end microscopy technology. The main aim of ALMF is to assist all EMBL groups and visitors through the microscopic imaging process: project planning, sample preparation, staining, microscope selection and use, image processing, presentation, data transfer and storage. ALMF is also facilitating automated microscopy and high content screening (HCS) projects. ALMF develops and co-develops with industrial partners state-of-the-art accessory software and microscopy equipment, as well as commercial equipment pre-evaluated in the facility.

The ALMF presently manages 26 top-of-the-line microscope systems including 8 high-content screening microscopes from leading industrial companies. Five image analysis workstations are provided for data analysis. In addition most of the microscopes are fitted for live imaging with an environmental chamber capable of regulating temperature and CO_2 concentration. More than 30 visitors per year come to carry out their own experiments in the ALMF or to evaluate microscopy equipment. The usage of the facility has exceeded 30000 hours per year. The ALMF was the seed for the European Light Microscopy Initiative (ELMI, www.embl.org/elmi/) that establishes links between light microscopy facilities users and industry throughout Europe.

The variety of projects carried out at ALMF range from single molecule to whole embryo imaging. Wide choice of advanced microscopy techniques is available at ALMF. They can be used for the determination of protein localization in cells or tissue, the tracking of dynamic processes in live environment, analysis of protein interactions and mobility through fluorescence recovery after photo bleaching (FRAP), fluorescence correlation microscopy (FCS), and fluorescence energy transfer (FRET).

Euro-BioImaging

The Euro-BioImaging Research Infrastructure (www.eurobioimaging.eu) brings together key research areas in imaging technologies stretching from basic biological imaging with advanced light microscopy and in vivo molecular imaging up to the clinical and epidemiological level of medical imaging of patients and populations. Euro-BioImaging will meet the imaging requirements of both biological and medical imaging communities by creating infrastructure facilities distributed across many European countries. The coordinated and harmonised deployment of imaging infrastructure under one Euro-BioImaging umbrella significantly addresses the fragmentation of such efforts currently present in Europe. Euro-BioImaging infrastructures will provide access to state-of-the-art equipment, provide training and continue the development of imaging technologies to offer them as new services.

Euro-BioImaging will create a distributed and strongly coordinated infrastructure for biomedical imaging in Europe. Euro-BioImaging infrastructures ("nodes") will be newly constructed or undergo major upgrades and devote a significant part of their capacity to external users. In this manner Euro-

BioImaging will serve European scientists by providing access to advanced imaging technologies across the full scale of biological and medical applications and at the same time provide the possibility for many existing imaging research institutions or laboratories to contribute to knowledge development and training. In addition, Euro-BioImaging will create a coordination platform delivering knowledge and expertise, allowing exchange of methodologies and the joint use of acquired data.

Euro-BioImaging has a strong supporter base. It comprises 39 beneficiaries from 15 European Member States (MS) and associated countries, more than 150 associated partners from 26 European MS and associated countries. The initiative is formally endorsed by over 205 universities, research councils, funding bodies, ministries, and industry partners. Furthermore, (Euro-)Bioimaging is a key priority on many national research infrastructure roadmaps of the EU.

P-CUBE

P-CUBE (www.p-cube.eu) is the first project within the Seventh Framework Program that supports cutting edge infrastructures critical for the efficient production and crystallization of proteins and protein complexes in contemporary structural biology. The infrastructures comprise technology platforms for high-throughput cloning and expression of proteins in prokaryotic and eukaryotic cells, high-throughput crystallization, high throughput selection technologies and advanced light microscopy. The program offers access to its infrastructures free of charge for scientists from the European Union and associated countries. European experts in the field from the University of Zürich, the University of Oxford and the European Molecular Biology Laboratory share expertise, equipment and their know-how.

The P-CUBE Advanced Light Microscopy Platform presently offers the possibility to perform state-of- the-art microscopy experiments using the adequate equipment. According to the proposed project, users and staff plan the experiments and organize the required reagents prior to the visit. EMBL Heidelberg can provide expression vectors for different fluorescent proteins, fluorescence labels, and chemical reagents. At the facility users receive support for the production of fluorescently labeled samples (e.g. protein expression in different cell lines for in vivo analysis, recombinant protein production for in vitro studies, chemical labeling of protein etc.). Subsequently, they use the appropriate microscopes at the ALMF to collect imaging data, process and evaluate them using optimal equipment and software.

Invited

IN VIVO CANCER CHARACTERIZATION AND THERAPY MONITORING WITH DIFFUSE OPTICS

R. Choe

Department of Biomedical Engineering, University of Rochester, USA, Regine_Choe@urmc.rochester.edu

Diffuse optical methods based on near-infrared light sources provide several unique functional parameters with deep tissue penetration [1]. Non-invasive measurements with multi-spectral light sources and use of diffusion approximation to model photon propagation in the tissue enables quantification of of oxygenated hemoglobin, deoxygenated hemoglobin, water and lipid concentrations, and tissue scattering (μs') properties. Based on oxy-hemoglobin (HbO_2) and deoxy-hemoglobin (Hb) concentrations, total hemoglobin concentration ($THC = Hb + HbO_2$) and blood oxygenation ($StO_2 = HbO_2/THC$) are calculated. Furthermore, blood flow information is accessible with diffuse optics based on correlation technique. On the other hand, tissue micro-environment (e.g. vascular leakiness, pH) or selective uptake of molecular targeted agent in the diseased tissue can be probed by measuring fluorescence signal of exogenous optical contrast agents. In addition to these unique functional parameters, diffuse optics utilize non-ionizing radiation (thus enabling frequent measurement), and low cost instrumentation. These features make diffuse optics suitable for providing complementary information to traditional clinical imaging modalities (e.g. X-ray, Ultrasound, MRI, PET/SPECT), and for monitoring progression or therapeutic response of a disease.

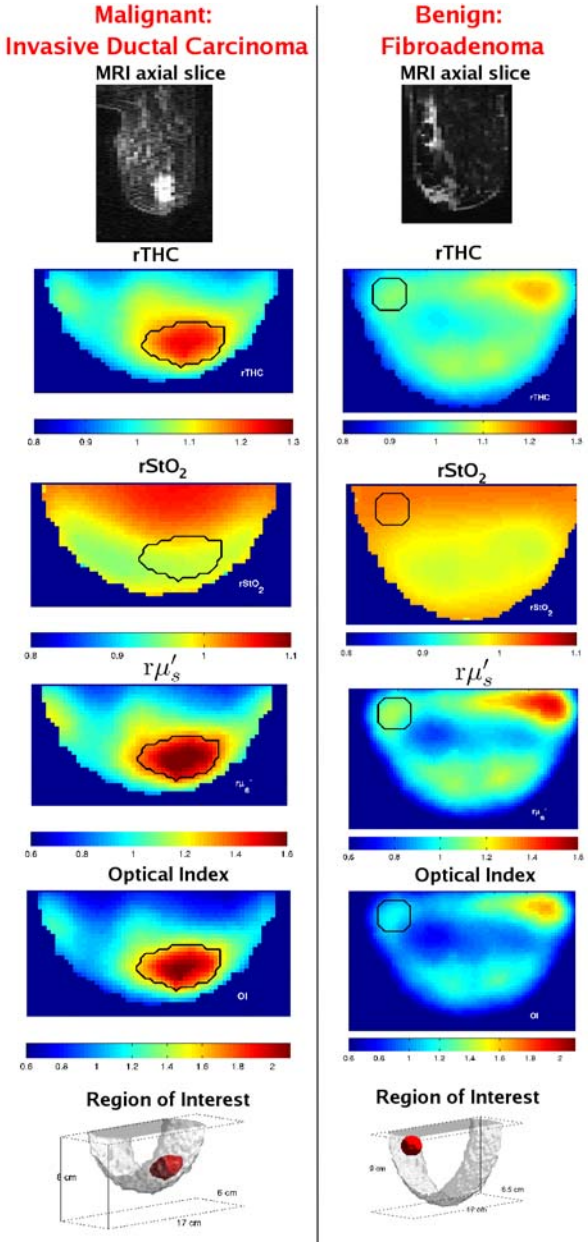

A variety of instrumentation and algorithmic strategies have been developed for tumor diagnosis and cancer therapy monitoring by several groups. For example, instruments geared for breast cancer spectroscopy/imaging differ with respect to measurement geometry (e.g. remission, parallel-plate, ring/cone), detection type (e.g. continuous-wave, frequency-domain, time-domain), wavelength implementation (e.g. broadband versus discrete wavelengths), source/detector numbers and/or compatibility with other imaging modalities. Depending on these choices, analysis algorithms vary too, ranging from analytic solutions in the homogeneous semi-infinite geometry to full-fledged 3D tomographic reconstruction. While these variations affect the system characteristics and accuracy in quantifying certain parameters, most groups observed high total hemoglobin concentration in tumor compared to benign or healthy normal tissues [2, 3]. In addition, the feasibility of applying diffuse optical techniques in the context of cancer therapy monitoring has been demonstrated successfully in both imaging instruments and with hand-held probes [4–10]. Thus far, tumor size and/or properties (e.g., total hemoglobin concentration, water) detected by diffuse optical methods have correlated well with patient response to chemotherapy (i.e., complete, partial or none) [10, 7, 8].

In this talk, I will review the theoretical and experimental backgrounds of diffuse optical techniques, and their application to cancer diagnosis and therapy monitoring in preclinical and clinical settings. In particular, this presentation will showcase the capabilities of diffuse optical techniques (1) to distinguish benign and malignant tumors, (2) to track changes induced by therapies, and (3) to image preferential uptake fluorescent contrast agents in cancer. Finally, the future research directions to bring diffuse optics closer to clinical applications will be discussed in terms of exploring new physiological parameters using novel imaging agents and hemodynamic effects of molecularly targeted therapies.

Acknowledgements

This research was supported by NIH R01-CA75124, R01-EB002109, K99-CA126187, P41-RR002305, NTROI U54CA105480, and Army DAMD17-00-1-0408.

References

1. T. Durduran, R. Choe, W.B. Baker, and A.G. Yodh, "Diffuse optical spectroscopy and tomography for tissue monitoring and imaging", *Rep. Prog. Phys.*, 2010, **73**, 076701.
2. D.R. Leff, O.J. Warren, L.C. Enfield, A. Gibson, T. Athanasiou, D.K. Patten, J. Hebden, G.Z. Yang, and A. Darzi, "Diffuse optical imaging of the healthy and diseased breast: A systematic review", *Breast Cancer Res. Treat.*, 2008, **108**, 9-22.
3. R. Choe, S.D. Konecky, A. Corlu, K. Lee, T. Durduran, D.R. Busch, B.J. Czerniecki, J. Tchou, D.L. Fraker, A. DeMichele, B. Chance, S.R. Arridge, M. Schweiger, J.P. Culver, M.D. Schnall, M.E. Putt, M.A. Rosen, and A.G. Yodh, "Differentiation of benign and malignant breast tumors by in-vivo three-dimensional parallel-plate diffuse optical tomography", *J. Biomed. Opt.*, 2009, **14**(2), 024020.
4. D.B. Jakubowski, A.E. Cerussi, F. Bevilacqua, N. Shah, D. Hsiang, J. Butler, and B.J. Tromberg, "Monitoring neoadjuvant chemotherapy in breast cancer using quantitative diffuse optical spectroscopy: a case study", *J. Biomed. Opt.*, 2004, **9**, 230-238.
5. R. Choe, A. Corlu, K. Lee, T. Durduran, S.D. Konecky, M. Grosicka-Koptyra, S.R. Arridge, B.J. Czerniecki, D.L. Fraker, A. DeMichele, B. Chance, M.A. Rosen, and A.G. Yodh, "Diffuse optical tomography of breast cancer during neoadjuvant chemotherapy: a case study with comparison to MRI", *Med. Phys.*, 2005, **32**(4), 1128-1139.
6. Q. Zhu, S.H. Kurtzma, P. Hegde, S. Tannenbaum, M. Kane, M. Huang, N.G. Chen, B. Jagjivan, and K. Zarfos, "Utilizing optical tomography with ultrasound localization to image heterogeneous hemoglobin distribution in large breast cancers", *Neoplasia*, 2005, **7**(3), 263-270.
7. S. Jiang, B.W. Pogue, C.M. Carpenter, S.P. Poplack, W.A. Wells, C.A. Kogel, J.A. Forero, L.S. Muffly, G.N. Schwartz, K.D. Paulsen, and P.A. Kaufman, "Evaluation of breast tumor response to neoadjuvant chemotherapy with tomographic diffuse optical spectroscopy: Case studies of tumor region-of-interest changes", *Radiology*, 2009, **252**, 551-560.
8. Q. Zhu, S. Tannenbaum, P. Hegde, M. Kane, C. Xu, and S.H. Kurtzman, "Noninvasive monitoring of breast cancer during neoadjuvant chemotherapy using optical tomography with ultrasound localization", *Neoplasia*, 2008, **10**, 1028-1040.
9. C. Zhou, R. Choe, N. Shah, T. Durduran, G. Yu, A. Durkin, D. Hsiang, R. Mehta, J. Butler, A. Cerussi, B.J. Tromberg, and A.G. Yodh, "Diffuse optical monitoring of blood flow and oxygenation in human breast cancer during early stages of neoadjuvant chemotherapy", *J. Biomed. Opt.*, 2007, **12**, 051903.
10. A. Cerussi, D. Hsiang, N. Shah, R. Mehta, A. Durkin, J. Butler, and B.J. Tromberg, "Predicting response to breast cancer neoadjuvant chemotherapy using diffuse optical spectroscopy", *Proc. Natl. Acad. Sci. U. S. A.*, 2007, **104**, 4014-4019.

RECONSTRUCTION METHOD FOR SOLVING INVERSE PROBLEM IN DIFFUSE FLUORESCENCE TOMOGRAPHY BASED ON NON-NEGATIVE TIKHONOV REGULARIZATION

I. Fiks, M. Kirillin, E. Sergeeva, and **I. Turchin**

Institute of Applied Physics RAS, 46 Ulyanov Street, 603950, Nizhny Novgorod, Russia
FiksII@yandex.ru

1. Introduction and methods

Optical tomography techniques are very attractive for biotissue diagnostics due to their non-invasiveness. They have various applications in modern medicine and biology. Among them are diagnostics of human brain, breast cancer diagnostics, monitoring of tumor growth and anticancer therapy control.

Unlike reconstruction in X-ray computed tomography, reconstruction of optical inhomogeneities or fluorophore distribution in optical tomography techniques is complicated by multiple light scattering in biotissue. Reconstruction of the fluorophore distribution (inverse problem solution) in the fluorescence diffuse tomography (FDT) [1-3] is based on data obtained by subsequent measurements made for different source-detector positions.

This reconstruction comes to solution of a system of linear equations:

$$Av=p, \tag{1}$$

where matrix $A=\{a_{ij}, i=\overline{1,M}, j=\overline{1,N}\}$ and a_{ij} describes fluorescent signal on the object boundary from elementary volume j with source-detector position i, $v=\{v_j, j=\overline{1,N}\}$ is an array of unknown fluorophore spatial distribution, $p=\{p_i, i=\overline{1,M}\}$ is an array of detected signal intensities at the object boundary. However, there is one more condition for unknown vector v, it must contains only non-negative components:

$$v=\left\{v_j \geq 0, j=\overline{1,N}\right\} \tag{2}$$

Therefore, the reconstruction problem comes to solution of the following system:

$$\begin{cases} Av=p \\ v_j \geq 0, j=\overline{1,N} \end{cases} \tag{3}$$

The condition (2) essentially decreases the condition number of system (1). If we know noisy vector $p_\delta = p+\delta p$ instead of initial vector p the solution noise δv can be estimated as following:

$$\frac{\|\delta v\|_2}{\|v\|_2} \leq \frac{S_A}{s_A}\frac{\|\delta p\|_2}{\|p\|_2}, \tag{4}$$

where S_A and s_A are the greatest and the smallest singular values of matrix A, correspondingly. This means that reconstruction error can be greater than right-side error by a factor of S_A/s_A. However, Eq. (4) under condition (2) can be written in the following form:

$$\frac{\|\delta v\|_2}{\|v\|_2} \leq \frac{S_A}{m_A}\frac{\|\delta p\|_2}{\|p\|_2} \leq \frac{S_A}{s_A}\frac{\|\delta p\|_2}{\|p\|_2},$$

where $m_A = \min_{\|v\|_2=1, v\geq 0} \|Av\|_2$. Since $m_A >> s_A$ (for example, in our numerical experiments $s_A \sim 10^{-20}$, $m_A \sim 10^{-2}$), the upper limit of reconstruction error decreases significantly. The use of condition (2) is necessary for correct solution of the reconstruction problem. Thus, we developed an iteration procedure for solving Eq. (3) based on the Tikhonov regularization with non-negative condition (TRNNC):

$$\begin{aligned} u^{(k+1)} &= (1-\gamma)u^{(k)} + \gamma(D(u^{(k)})A^T AD(u^{(k)}) + \alpha E)^{-1} A^T p \\ v^{(k+1)} &= \left(u^{(k+1)}\right)^2 \end{aligned}, \tag{5}$$

where α is regularization parameter, $0<\gamma<<1$ is the relaxation parameter of iteration procedure introduced for its robustness, $D(u)=diag(u)$, E is unit $N\times N$ matrix.

2. Results

In Fig. 1 we present results of fluorophore reconstruction using different standard methods: the algebraic reconstruction technique (ART [1]), simultaneous multiplicative algebraic reconstruction technique (SMART [5]), non-negative least squares (NNLS [6]), Tikhonov regularization (TR [7]) and the method proposed in the present paper (TRNNC). The object under reconstruction is a fluorescing 3x3x3 points cube in a parallelepiped 20x20x9 points cuvette. In order to simulate real experimental conditions we added $\|\delta p\|_2 / \|p\|_2 = 10^{-6}$ noise in the right-hand side of Eq. (1). Reconstruction time T and relative reconstruction error $err = \|\delta v\|_2 / \|v\|_2$ are shown in brackets.

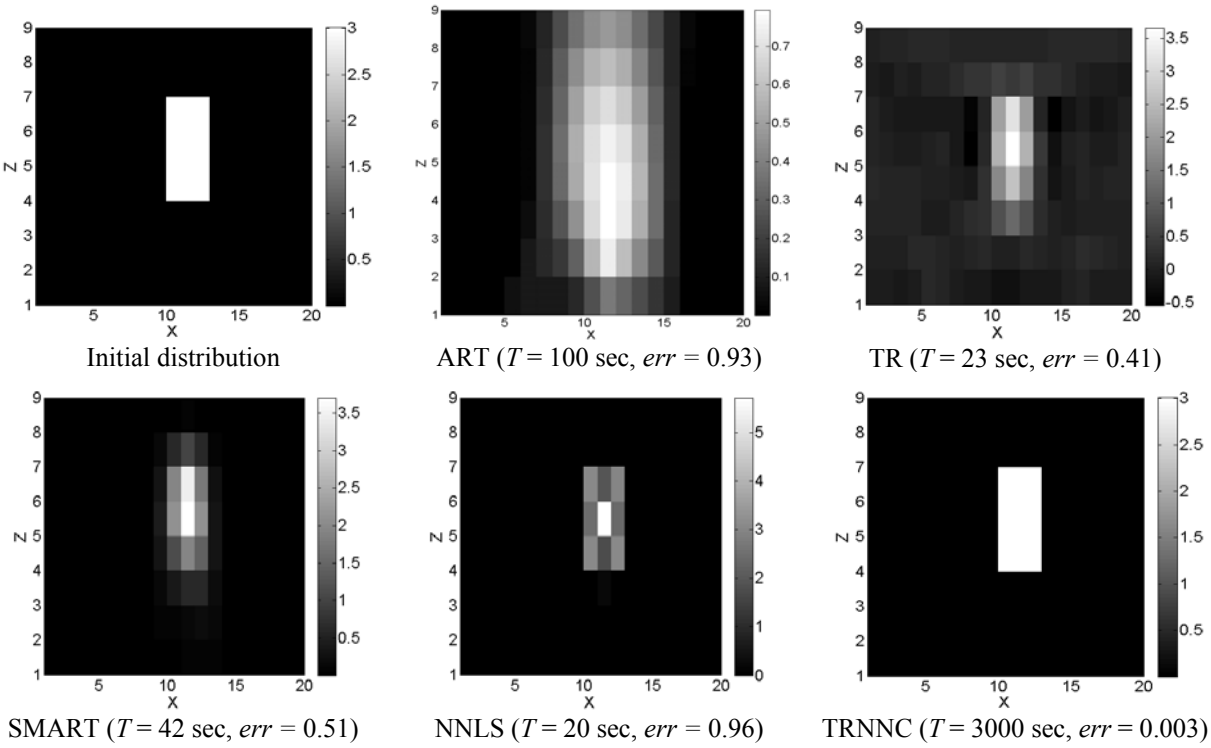

Fig. 1. Results of fluorophore reconstruction using different standard methods

As one can see from this figure the proposed method provides reconstruction with smallest error compared to all other employed techniques. On the other hand, it requires longest calculation time and additional RAM usage. Consequently, this method can be applied only for problems with moderate size of matrix in system (1), namely, with moderate number of reconstructed voxels N (because inverse matrix $N \times N$ must be calculated at each iterative step).

Acknowledgements

This work was partly supported by the Russian Foundation for Basic Research (10-02-01109, 11-02-01129), by the Science and Innovations Federal Russian Agency (projects 02.740.11.0086, 16.512.11.2140, 02.740.11.0839, 14.740.11.0253, 16.120.11.1909-MK), by the Program of Fundamental Researches of the Presidium of the Russian Academy of Sciences and grant of the Government of Russian Federation No. 11.G34.31.0017.

References

1. I.V. Turchin, V.A. Kamensky, V.I. Plehanov, A.G. Orlova, M.S. Kleshnin, I.I. Fiks, M.V. Shirmanova, I.G. Meerovich, L.R. Arslanbaeva, V.V. Jerdeva, A.P. Savitsky, *J. Biomed. Opt*., 2008, **13**(2), 041310.
2. V. Ntziachristos, C.-H. Tung, C. Bremer, R. Weissleder, *Nature medicine*, **8**(7), 757-760.
3. S.V. Patwardhan, S.R. Bloch, S. Achilefu, J.P. Culver, *Optics Express*, 2005, **13**, 2564-2577.
4. M.Yu. Kirillin, A.V. Priezzhev, R. Myllylä, , *Proc. SPIE*, 2006, **6163**, 6163-25.
5. C. Byrne, *IEEE Trans Image Process*, 2005, **14**(3), 321-7.
6. C.L. Lawson, R.J. Hanson, *Solving Least Squares Problems*, Prentice-Hall, 1974.
7. A.N. Tychonoff, V.Y. Arsenin, *Solution of Ill-posed Problems*. Washington: Winston & Sons, 1977.

IMAGE RECONSTRUCTION USING THE INVERSE RADON TRANSFORM

C. Gavrila[1], **V. Petrehus**[2], and **I. Gruia**[3]

[1, 2] Technical University of Civil Engineering Bucharest, Romania, cgavrila2003@yahoo.com
[3] University of Bucharest, Romania

Optical tomography is a new medical imaging modality. A large amount of clinical work has shown the real benefits which such a method could provide. At the same time, a considerable effort has been put into theoretical studies. The result of the optical tomography is not always optimal. That is why image reconstruction operations are needed. In this paper we apply a numerical algorithm for image reconstruction using the inverse Radon transform proposed in [2] and we use MathCad. An essential requirement is to treat the problem in a nonlinear fashion, by using an iterative method.

Given the function in [2] $f(x_1,x_2) = -\frac{1}{4\pi^2}\int_0^{2\pi} h_\rho(\rho,\theta)d\theta$ where (x_1, x_2) a point from the plane $h_\rho(\rho,\theta) = \frac{\partial}{\partial\rho}\int_{-\infty}^{\infty}\frac{Rf(\rho',\theta)}{\rho'-\rho}d\rho'$ and $\rho = x_2\cos(\theta) - x_1\sin(\theta)$, we defined the following algorithm for the reconstruction of $f(x_1,x_2)$:

1. Take all discreet data of Radon transform $Rf(\theta,\rho)$ for $\theta = \theta_j = \frac{2\pi j}{N}$, $j = 0,1,...,M–1$, $\rho = \rho_i$, $I = 0,1,\ldots,N–1$ in the matrix $f_{i,j} = Rf(\theta_j,\rho_i)$.

2. Interpolate function $Rf(\theta,\rho)$ either linearly or by spline functions (we used a linear interpolation)

3. Compute $\int_{-\infty}^{\infty}\frac{Rf(\rho',\theta)}{\rho'-\rho}d\rho'$ for $\theta = \theta_j$ using the interpolation at point 2.

4. The derivative result from 3 gives $h_j(\rho) = \sum_i \frac{f_{i+1,j}-f_{i,j}}{\rho_{i+1}-\rho_i}\cdot\ln\left(\left|\frac{\rho-\rho_{i+1}}{\rho-\rho_i}\right|\right) + \frac{f_{i+1,j}}{\rho-\rho_{i+1}} - \frac{f_{i,j}}{\rho-\rho_i}$

5. For $\rho = x_2\cos\theta_j - x_1\sin\theta_j$ in $h_j(\rho)$ the result is h_j.

6. Compute $f(x_1,x_2) = -\frac{1}{4\pi^2}\int_0^{2\pi} h_\rho(\rho,\theta)d\theta$ by approximation from $S = -\frac{1}{4\pi^2}\frac{2\pi}{N}\sum_j h_j$

Generally speaking, function reconstruction is made in a matrix of points, where each value in a given point represents the grey intensity in the respective point. The program uses Mathcad for loading an image, then the matrix is read with the grey intensities for each point, and the density resulted from there by interpolation. The function was interpolated with the option that the image is enclosed in a disc with radius 1. The Radon transform, see also [1], resulted from the integration on a number of directions and, for each direction, for a number of equidistant parallels, thereby giving the Radon data matrix [3].

We applied this algorithm for reconstructing the image of some tissue. The image is provided by the optical circuit in fig. 1, which measures polarized structure of the biological tissue. The polarization images of the biological tissue done with the help of micro objective 7 have been projected into the plane of a light-sensitive area (800x600) of CCD-camera 10, which provided the measuring range of structural elements of the biological tissue (6) for the following scales 2 – 2000 μm. The analysis of the biological tissue images has been done by the polarizer 9.

The method of determining the coordinate distribution of the polarization singularities, [4], of the biological tissue image consists of the following sequence of steps: the minimum and maximum levels of the image intensity for each separate pixel of CCD-camera and the rotation angles corresponding to them are determined by rotating an axis of the analyzer transmission 8 in the limits of $\Theta = 0 - \pi$.

By comparing the real and the reconstructed images we can conclude that the algorithm is not good enough and that it must be revised. In [5] the authors used a similar algorithm, but they used an interpolation with spline functions. According to the examples included therein, the reconstruction is much more precise, whereas the computation takes longer time. In a future study we intend to compare various inversion methods.

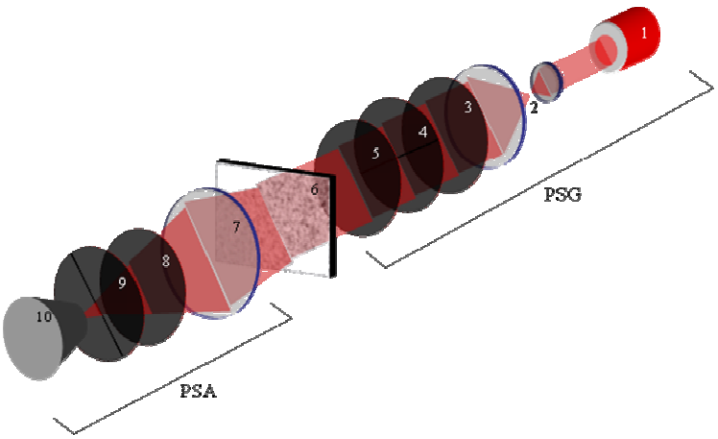

Fig. 1. Optical scheme of experimental polarimetry: 1 – laser source; 2 – afocal system; 3, 5, 8 – quarter-waved (λ/4) plates; 4,9 – linear polarizer; 6 – biological tissue; 7 – micro objective; 10 – CCD camera

Figure 2 demonstrates the series of experimentally determined topological distribution and showing the real images captured with CCD camera and the reconstructed images with inverse Radon transform.

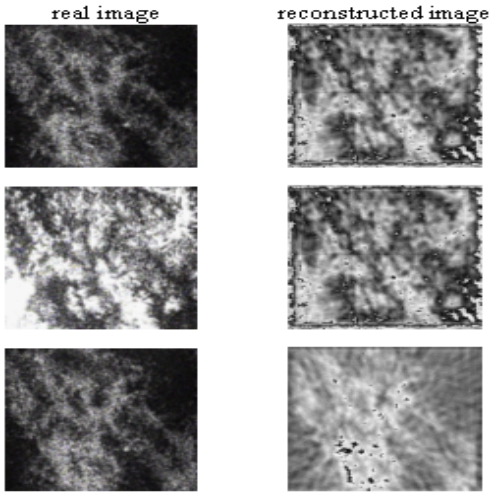

Fig. 2. The real and reconstructed images

Experimental measuring of biological tissue polarization-correlation maps provides the possibility to do the analysis of the influences of orientation architectonics peculiarities of physiologically different biological tissues in a polarization map speckle-image structure.

There is an interconnection between the coordinate pathological structure change diagnostics using the complex degree of mutual polarization of biological tissue images and the optical-geometrical parameters of their physiologically normal and pathologically changed birefringent architectonics nets.

Acknowledgements. This research has been supported by the Technical University of Civil Engineering Bucharest, Romania under the contract PNCDI II, 42-105/2008.

References

1. A.S. Fokas, I.M. Gel'fand, *Lett. Math. Phys*., 1994, **32**, 189.
2. A.S. Fokas, R.G. Novikov, "Discrete Analogues of Equations and of Radon Transform", *Acad. Sci. Paris Ser. I. Math*., 1991, **313**, 75.
3. S. Helgason, *The Radon Transform*, Birkhäuser, Boston, 1980, 202.
4. D.H. Goldstein, E. Collett, *CRS Press*, NewYork, 2003.
5. A.S. Fokas, A. Iserles, V. Marinakis, "Reconstruction Algorithms for Positron Emission Tomography and Single Photon Emission Computed Tomography and their Numerical Implementation", *Physics*, 1992, 0412030v1.

POLARIZATION-SENSITIVE TIME DOMAIN OPTICAL COHERENCE TOMOGRAPHY BASED ON TWO ORTHOGONAL ELLIPTICALLY POLARIZED MUTUALLY COHERENT WAVES

V.M. Gelikonov, G.V. Gelikonov, and **I.V. Kasatkina**

Institute of Applied Physics RAS, Nizhny Novgorod, Russia
e-mail: grig@ufp.appl.sci-nnov.ru

The polarization sensitive methods for in-vivo imaging (PS OCT) are improved regularly [1-5]. Some modifications of the PS OCT technique allow obtaining a most comprehensive information about polarization properties of tissue and conventional structural OCT imaging simultaneously [5]. Interference in-depth selection of scattered light and control of changes in its polarization state relative to the initial wave allow determining various polarization properties of tissue, such as birefringence, diattenuation, orientation of optical axes, and depolarization [5-6]. Polarization properties of biotissue contain information about the presence of organized biotissue structures, such as collagen [6-7] and its concentration, type, and inclination angle, as well as tissue microstructure [6]. It is practicable to use PS OCT for sounding biotissues possessing regular birefringence (muscle, tendon, cartilage, dermis of skin, coronary artery, anterior eye segment, retinal nerve fiber layer, and vocal fold). When sounding soft biotissue with weak birefringence, PS OCT methods are also more informative than OCT, as they allow more exact interpretation of images. It is known that reflection at biotissue may be decreased exclusively due to polarization effects [6, 8].

Modeling of the polarization effects shows that false layers may appear in many simulations and that interpretation of PS OCT images is not always straightforward [9]. For instance, as the structure of superficial biotissue layers is very complicated, accurate information about axes orientation may be acquired only for the first birefringent layer of the sample. If a second birefringent layer has a different axes orientation, it can be determined only by a more sophisticated algorithm making use of the information about the first layer [9-10]. However, the boundaries between the birefringent layers can be recognized by the change of color representing different axes orientations [10].

Starting with the traditional OCT method, its advance toward clinical applications using a flexible probe is primarily based on fiber optics. Insensivity to probe bending was first realized by using a linear birefringent fiber [11]. The birefringence of optical fiber was also used for two-channel reception of scattered waves, which is interesting for cross-polarization scattering investigations [7, 12]. Study of sample birefringence using such a system must evidently take into consideration orientation of the optical axes of the medium, as the probe wave polarization is linear [7]. This condition is analogous for tissues with both strong and weak birefringence. Stages of PS OCT method elaboration on the basis of SM fiber were analysed in [5]. These PS OCT methods allow numerical evaluation and imaging of different polarization properties of biotissue. Successive steps in solving the important problem concerning ambiguity of the incident polarization state relative to the orientation of tissue optical axes were shown in [5]. The best results were obtained using a couple of independent orthogonal waves, with allowance for the phase relations for waves backscattered by the anisotropic medium [5].

Clinical applications of endoscopic OCT methods based on Michelson interferometer frequently face the problem of interchangeability of single-mode fiber probes. It is a complicated problem as the dispersion properties of long fiber probes have low repetition. These difficulties are eliminated with the use of the method of time domain optical coherence tomography based on a measuring Fizeau interferometer and a compensating Michelson interferometer in an optical scheme with a common path for probe and reference low-coherence waves [13]. This common path scheme was used as a prototype for a new cross-polarization optical coherence tomography (CP OCT) based on mutually orthogonal arbitrarily polarized mutually coherent waves with optical path lengths differing by ΔL [1].

The optical scheme of the new time-domain CP OCT modality shown in Fig. 1 has been improved by adding a Faraday rotator immediately after the delay line. It allows turning the polarization axes of the mutual orthogonal elliptic waves by angle θ. The compensating Michelson interferometer was also modified by additional partitioning of one of the arms into two with different delay lines. Co- and cross channels reception is organized with a single detector balance scheme. The reception of light backscattered from each mutually orthogonal probe wave in a co-channel is optimal, if its polarization

coincides with the initial polarization of the probe wave possessing the corresponding delay. The reception of light in the cross-channel is optimal when the polarization is orthogonal to the probe wave polarization that is a result of the influence of medium birefringence and cross-scattering.

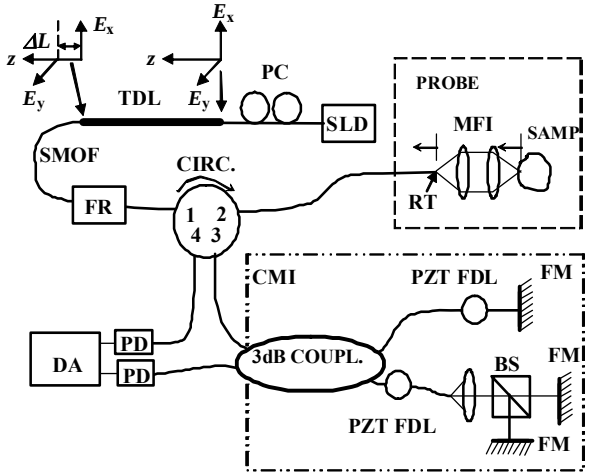

Fig. 1. Optical scheme of CP OCT: SLD – superluminescent diode; PC – polarization controller; TDL – time-delay line consisting of a piece of birefringent fiber; SMOF – single-mode optical fiber; Circ. – 4-port circulator; RT – reflecting tip of the fiber; LS – lens system; Sample – sample under study; 3dB coupler – 0.5x0.5 coupler; PZT FDL – piezoelectric fiber delay line; FM – 45° Faraday mirrors; PD – photo diodes; DA – differential amplifier; MFI – measuring Fizeau interferometer; CMI – compensating Michelson interferometer, FR – Faraday rotator

Owing to coherence of orthogonal probe waves, signal U_{CO} at Doppler shift frequency Ω in the co-channel at regular medium birefringence has the form $U_{CO} \sim A_{CO}\cos(\phi)\cos(\Omega t)$. However, signal U_{CROSS} in the cross-channel specified by regular medium birefringence depends not only on regular phase shift φ, but also on the orientation of medium optical axes relative to the probe wave ellipse axes:

$$U_{CROSS} \sim A_{CROSS}\sin(\phi)\sin(2\theta)\sin(\Omega t).$$

Here, the coefficients $A_{CO,CROSS}$ characterize the amplitude in-depth scattering coefficient in co- and cross-channels. The co- and cross-channel signals are read successively during each A-scan. Apparently, at weak medium birefringence, the cross-channel OCT images usually have lower brightness as compared with those in the co-channel and can be differentiated along the axes of regular biotissue structures. For this it suffices to summarize images obtained at θ = 0, 15°, 30° using RGB staining.

The color of cross-channel images will depict orientation of unidirectional biotissue fragments, while co-channel images will be always white. Co- and cross-OCT images of tissue with weak birefringence are presented.

Acknowledgements

The work was supported in part by the RFBR Grant No. 09-02-00650-a, the Federal Agency in Science and Innovations, State Contract No. 02.740.11.0225 of 07.07.2009, State Contract No. 02.740.11.0516 of 15.03.2010, and the Grant of the RF President Council Supporting Leading Scientific Schools No. НШ 3800.2010.2.

References

1. V.M. Gelikonov and G.V. Gelikonov, *Laser Physics Letters*, 2006, **3**(9), 445-451.
2. W.Y. Oh, S.H. Yun, B.J. Vakoc, et al., *Optics express*, 2008, **16**(2), 1096-1103.
3. M. Yamanari, S. Makita, and Y. Yasuno, *Opt. Express,* 2008, **16**(8), 5892-5906.
4. W.Y. Oh, B.J. Vakoc, S.H. Yun, et al., Opt. Lett., 2008, **33**(12), 1330-1332.
5. K.H. Kim, B.H. Park, Y. Tu, et al., *Opt. Express*, 2011, **19**(2), 552-561.
6. B. Liu, M. Harman, S. Giattina, et al., *Appl. Opt.* **45**(18), 4464-79 (2006).
7. R.V. Kuranov, V.V. Sapozhnikova, I.V.Turchin, et al., *Optics Express*, 2002, **10**(15), 707-713.
8. J.F. De Boer, S. M. Srinivas, B. H. Park, et al., *IEEE J. of Selected Topics in Quantum Electronics*, 1999, **5**(4), 1200-1204.
9. B. Liu, M. Harman, and M.E. Brezinski, *J. Opt. Soc. Am*., 2005, **A22**(2), 262-271.
10. C.K. Hitzenberger, E. Gotzinger, M. Sticker, et al., *Optics Express*, 2001, **9**(13), 780-790.
11. V.M. Gelikonov, G.V. Gelikonov, R.V. Kuranov, et al., *Letters to JETP*, 1995, **61**(2), 149-153.
12. F.I. Feldchtein, G.V. Gelikonov, V.M. Gelikonov, et al., *Optics Express*, 1998, **3**(6) 239-250.
13. F.I. Feldchtein, J. Bush, G.V. Gelikonov, et al., *PROC. SPIE International Society for Optical Engineering*; 1999. – San Jose, California, USA, 2005, 349-355.

GENETICALLY ENCODED MICROSECOND-TIME-RESOLVED SUBSTRATE FOR CASPASE-3: DEVELOPMENT OF THE TECHNIQUE OF EXPERIMENTS ON LIVING CELLS

A.S. Goryashenko[1], **V.V. Zherdeva**[2], **T.V. Ivashina**[3], and **A.P. Savitsky**[2]

[1] A.N. Bach Institute of Biochemistry, Russian Academy of Sciences, Moscow, Russia, asgoryash@yandex.ru
[2] A.N. Bach Institute of Biochemistry, Russian Academy of Sciences, Moscow, Russia
[3] Skryabin Institute of Biochemistry and Physiology of Microorganisms, Russian Academy of Sciences Pushchino, Moscow Region, Russia

Apoptosis is one of the variants of the programmed cell death. Disfunction of the apoptosis process leads to neurodegenerative, tumoral and autoimmune diseases. The central enzyme in the process of apoptosis is so-called caspase-3, because it unites death receptor and mitochondrial pathways of proteolytic cascade. Caspase-3 activity is an important marker for an estimation of efficiency of the drugs which induce apoptosis, such as antitumor drugs.

In our laboratory the microsecond time-resolved FRET-biosensor for caspase-3 has been developed. Biosensor was constructed as complex between terbium and genetically coded terbium-binding peptide (TBP) linked to red fluorescent protein TagRFP. Hydrolysis of the DEXD sequence in the linker by caspase-3 leads to the physical division of the donor and acceptor by means of diffusion, therefore the distance between the donor and an acceptor increases and FRET efficiency decreases, allowing us to carry out direct monitoring of activity of caspase-3. Advantage of use of a terbium ion as the donor is that fluorescence lifetime of lanthanide-ions is very great - from micro - to milliseconds while lifetime of background fluorescence reaches a maximum of 10-15 nanoseconds, so time-resolved fluorescent spectroscopy allows us to register a signal of a sensor against a high background signal that leads to increasing of the system's sensitivity.

In our previous studies we showed that caspase-3 hydrolyses the sensor *in vitro*. A following stage is transition to cellular model, therefore the purpose of the given work is to create a technique of definition of caspase-3activity in living cells by means of the developed substrate.

Creation of the recombinant plasmid on the basis of a vector pcDNA3, incorporating cytomegalovirus promoter, which provides an expression of the protein of interest in eucaryotic cells became the first stage of the work. The coding sequence of the biosensor was cloned from the prokaryotic plasmid based on pET22b vector into the eukaryotic pcDNA3 vector. Cloning was performed on EcoRI and HindIII restriction sites. Presence of a coding sequence in the produced plasmid was confirmed by sequencing.

The next stage of the work was an experiment with tumoral cell line A549 – lung adenocarcinoma cells. This cellular line is well described in the literature, besides experiments on it allow to model action of various apoptosis inducers on tumours. We performed transitoric transfection of A549 cells with the developed plasmid pcDNA3-TBP-19-TagRFP by means of reagent Lipofectamine 2000 ("Invitrogen", USA) at various parities of DNA-reagent (from 20 to 40 µl of the reagent and from 8 to 16 µg of DNA) and incubation within 5 or 24 hours. Presence of an expression of the protein of interest was defined by means of a fluorescent microscope. On the images received by a method of phase contrast, it is visible that use of the big doses of a complex Lipofectamine-DNA with long incubation period leads to morphological changes in cells that testifies strong toxicity while small doses and small incubation time does not lead to such consequences - cells are spread on a cell culture dish. Fluorescent images also testify that more preferable is the transfection with smaller quantity of reagents and short incubation time.

Next step of our research was the insertion of the second component of a substrate, namely – a terbium ion, into cells. For more efficient insertion it we decided to bind terbium into the complex with citrate anion – cellular metabolite compound. Besides, such complex is labile enough that after insertion into a cell terbium ion form a complex with terbium-binding peptide from our substrate.

Because in the literature there is data about toxicity of lanthanides, in particular lanthanum, cerium, neodymium, samarium, gadolinium and ytterbium [1, 2], it was necessary to obtain the data about toxicity of terbium citrate. For this purpose A549 cells were incubated in the RPMI-1640 medium containing terbium citrate at various concentrations within 24 hours and then definition of number of the survived cells by means of fluorescein diacetate was performed. Apparently from the resulted

histogram (see Fig. 1), terbium citrate isn't toxic for cells up to concentration of 2 mM within 24 hours.

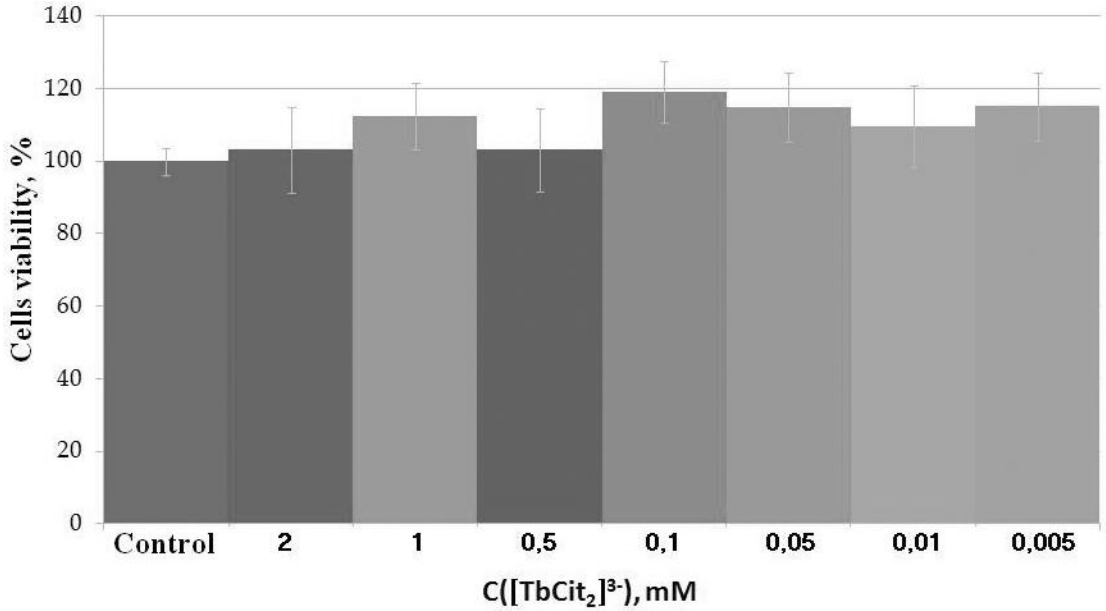

Fig. 1. A549 cells viability after 24 h incubation with different terbium citrate concentrations

As terbium citrate isn't toxic, its insertion into cells became the next stage of work. The insertion principle is described in the literature [3]. As a matter of fact, terbium citrate enters through the calcium channels of cells. For this purpose we placed the A549 cells into the 50 мM HEPES, 93 mM NaCl, 5 mM KCl, 2 mM $MgCl_2$, pH 7,4 buffer with 50 or 100 μM of terbium citrate and 500 μg/ml dextran sulphate (Mw = 500 000). Cells were incubated in such solution during 20 min at 4ºC, then $CaCl_2$ was added up to 2 mM concentration and incubation continued for 5 min. As an analytical signal we used the luminescence intensity of corresponding solutions at 545 nm after addition of commercially accessible enhancement solution ("Wallac", Finland). The results obtained shows that relative share of terbium citrate entered into cells doesn't change if we increase terbium citrate's concentration in the buffer for insertion, but the absolute quantity of terbium citrate has increased twice. Besides, within an hour of incubation there was no liberation of terbium citrate into medium.

Thus, the given work allows to draw following conclusions:

1) The method of transitoric transfection of coding sequence of substrate TBP-19-TagRFP in eukaryotic cells by means of a vector pcDNA3 is optimized.

2) Results of experiments on transitoric transfection of A549 tumour cell line by produced plasmid have shown that the expression of protein TBP-19-TagRFP is observed already at transfection within 5 hours by a complex with 20 μl of the Lipofectamine and 8 μg of DNA.

3) The data about viability of A549 cells in the presence of ion Tb^{3+} has shown that terbium citrate up to concentration of 2 mM doesn't possess toxic effect within 24 hours.

4) Insertion of terbium citrate into A549 cells showed that concentration increase of terbium citrate in the buffer for insertion from 50 to 100 μM the quantity of terbium which entered into cells, also increases twice. In addition, cells incubation with the full medium within 1 hour doesn't lead to liberation of terbium ions.

References

1. T. Sato, M. Hashizume, Y. Hotta, Y. Okahata, *Biometals*, 1998, **11**, 107-112.
2. H. Liu, L. Yuan, X. Yang, K. Wang, *Chem. Biol. Interact*., 2003, **146**, 27-37.
3. K. Blomberg, C. Granberg, I. Hemmla, T. Lovgren, *J. Immunol. M.,* 1986, **86**, 225-229.

POLARIZATION MICROSCOPY OF CANCER CHANGES OF THE PROSTATE TISSUE

I. Gruia[1], C. Gavrilă[2], M.I. Gruia[3], S. Yermolenko[4], and **P. Ivashko[4]**

[1] University of Bucharest, Faculty of Physics, Romania
[2] Technical University of Civil Engineering Bucharest, Romania
[3] Institute of Oncology, Bucharest, Romania
[4] Chernivtsi National University, Chernivtsi, Ukraine
yeserg@rambler.ru

Preface

Numerous studies revealed that in various pathologiies the structure of biotissues changes, particularly in the occurrence and development of cancer [1, 2]. We know that this should be manifested in the change of polarization parameters of the incident polarized radiation research facility. To identify and assess these changes different methods are used: measuring Stokes, Jones and Mueller matrices, spectrophotometric study. One of the simple methods in these studies is measuring the magnitude of linear dichroism.

The biological tissue (BT) is treated as a monolayer containing the ensemble of optically uniaxial birefringent fibrils [3, 4].

Experimantal results and discussion

For estimation of diagnostic potentialities of statistical analysis of the prostate tissue images the histological sections of physiologically normal (21 samples) and oncologically changed (22 samples) of the tissue were investigated.

Histological sections of optically thick (reduction factor $\tau \approx 1.2$, geometrical thickness – 400 μm), layers of prostate tissue were used as the objects of investigation.

Polarization images of the healthy (a, b) and oncologically changed (c, d) prostate tissues obtained for coaxial (0-0) and crossed (0-90) polarizer and analyzer are presented in Figure 1.

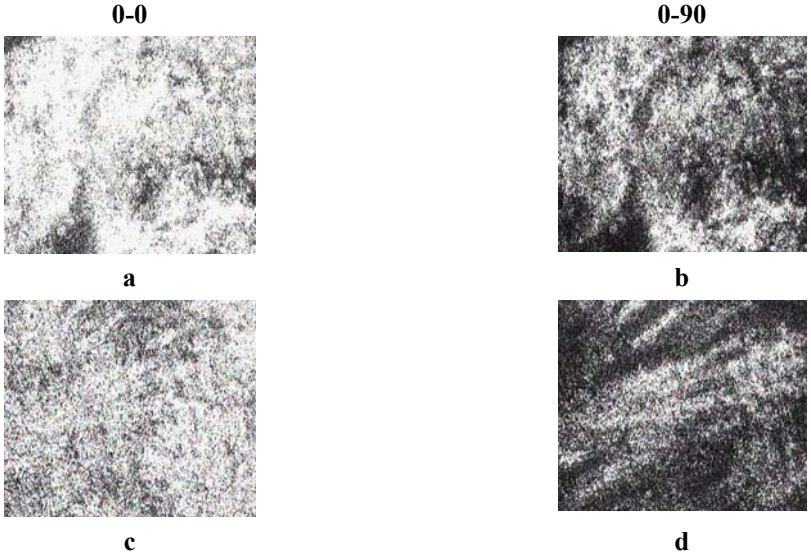

Fig. 1. Polarization images of optically thick prostate tissue layer

Statistic moments of the first (M), second (σ), third (A) and fourth (E) orders were used as the analytical tool for estimating the ensemble of random values of z, that characterize the image of biological object (intensity I, polarization azimuths α and ellipticities β) and its optical-geometrical structure (orientation directions of the protein fibrils and birefringence index of their substance Δn).

The results of statistic processing of experimentally obtained intensity distributions $I(0-0)$, $I(0-90)$ of the samples of healthy and oncologically changed human prostate tissue are illustrated in Fig. 2.

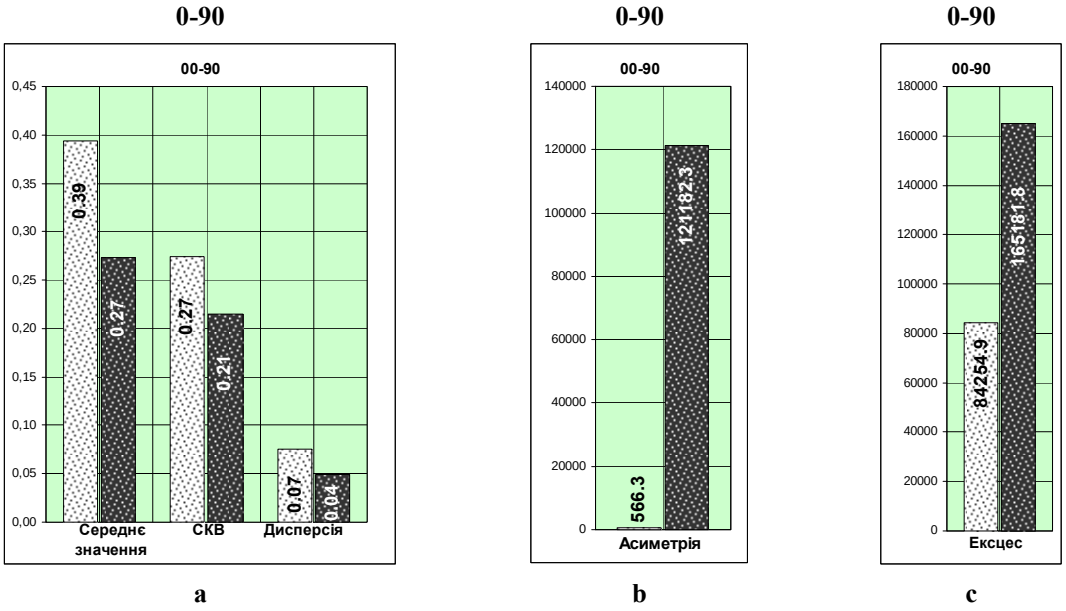

Fig. 2. Correlation between statistic moments of intensity distributions of polarization images

The third statistic moment (A) proved to be the most sensitive to pathological changes in orientation structure. Its value in the intensity distribution of polarization image $I(0-90)$ of oncologically changed tissue is 21 times higher if compared with the similar statistic parameter of the intensity distribution of the healthy tissue.

Conclusion

Thus, the efficiency of laser polarimetry technique of optically thin layers of human prostate tissue in defining its oncological state was proved. It was analytically substantiated and experimentally established that the 3rd and the 4th statistic moments of coordinate intensity distributions $I(0-90)$ of polarization images of human prostate tissue are most sensitive to the changes in orientation-phase architectonic structure.

References

1. O.V. Angelsky, S.B. Yermolenko, O.G. Prydij, A.G. Ushenko, Ye.G. Ushenko, *J. Holography Speckle*, 2006, **3**, 27-34.
2. A. Ushenko, S. Yermolenko, A. Prydij, S. Guminetsky, I. Gruia, O. Toma, K. Vladychenko, *Proc. of SPIE,* 2008, **7008**, 70082C-1 – 70082C-11.
3. S. Yermolenko, A. Prydij, K. Vladychenko, *Proc. of SPIE,* 2008, **7008**, P.70082D-1 – 70082D-7.
4. A.D. Mikhailova, S.B. Ermolenko, D.A. Zimnyakov, O.V. Angelsky, *Proc. of SPIE,* 2009, **7388**, 738819-1 – 738819-8.

POLARIZATION SPECTROMETRY IN DIAGNOSTICS OF MALIGNANT TRANSFORMATION OF BIOTISSUES

I. Gruia[1] and **S. Yermolenko**[2]

[1] University of Bucharest, Faculty of Physics, Romania;
[2] Chernivtsi National University, Chernivtsi, Ukraine
yeserg@rambler.ru

Preface

Early detection of malignant transformation is a goal of modern medicine and to this end there is an impressive number of approaches from the scientific field that tries to identify early changes preceding malignant transformation in order to establish a correct diagnosis. This paper aims at studying the combination of optical and biochemical techniques for identifying the changes in membrane dynamics of growth and development of experimental solid tumors.

Tumors obtained in murine models are considered to be an important experimental tool for elucidation of malignant mechanisms, as there is no perfect model for clinical oncology. Transplanted tumors in animals experiments are different from human tumors in several respects: the rate of growth is much faster, less heterogeneous cell is expressed; developed invasive and infiltration capacity ensures much lower metastasis. A major disadvantage of transplanted tumors is the appearance of subpopulations with differentiated cell biological behavior from parental cells.

Experimental results and discussion

In order to investigate thin tissue cuts of the prostate gland, nearly one hundred cuts were made. Unfortunately, the investigation was possible only on some of those cuts, as a great amount of samples turned to be so small that the cutover of the beam exceeded their magnitudes. Despite this, the results of the investigation of different types of tumors (4–5 samples for each type) can be regarded to have a general character [1, 2].

The results of the investigation of the benign tumor tissues showed that the magnitude of the linear dichroism Δ is insignificant in the whole studied spectral range $\lambda = 280$–840 nm and specific regularities in its change aren't observed.

The results of the investigation of the malignant tumor tissues in the form of spectral dependence of the magnitude Δ for two samples are shown in this paper. Spectral dependences of the dichroism magnitude for two tissue samples of the esophagus with a malignant tumor are shown, from which we can see that in the area $\lambda < 380$ nm and $\lambda > 700$ nm the linear dichroism is also lacking. Two maxima are observed: at $\lambda = 440$ nm and $\lambda \approx 530$–540 nm, and the last one is not clearly marked.

We used as objects for studies samples of thin muscle tissue cuts of rats at different stages of cancer disease: 7, 17, 40, 47, 52 days after cancer cell implantation. As this procedure was done on five rats, there were only 25 samples for this investigation. For demonstration of the methodology of the investigation and processing of the results consider a sample of one rat 7 days after contamination.

The corresponding transmission factors are

$$\tau_0 = \frac{I_{\min}}{I_0}, \qquad \tau_{90} = \frac{I_{\max}}{I_0}, \tag{1}$$

the magnitude of the linear dichroism

$$\Delta = \tau_{90} - \tau_0 = \frac{I_{\max} - I_{\min}}{I_0}, \tag{2}$$

the mean factor of the sample transmission

$$\tau = \frac{I_{\max} + I_{\min}}{2I_0}. \tag{3}$$

The investigation of the given sample on the spheric photometer showed that the magnitude Δ is close to zero practically for all λ, except $\lambda = 350$ nm, for which $\Delta = 0.010$ at $\tau_c = 0.888$.

As not all the samples were good for the investigation (heterogeneity of the beam thickness, insufficient size of the sample and as the result the radiation beam with the diameter of 6 mm was not

fit for the studies), that's why we obtained a full set of tables for different stages of cancer disease development only for three rats.

A similar regularity is noticed for all the rats: the linear dichroism grows in the investigated spectral range with the growth of the cancer disease time for about 47–50 days, up to 52 days its decrease is noticed. It can be explained by the fact that with the growth of the cancer tumor its structure arrangement grows to some range (47–50 days), and then destructive processes begin from the 50-th day. Besides we can observe that the magnitude of Δ depends greatly on the wavelength λ and the longer the cancer process is.

Moreover, two maxima are observed at the beginning of the process (7–17 days) in most cases in the following dependences $\Delta = f(\lambda)$: the first is at $\lambda \approx 430$ nm and the second is at $\lambda \approx 500$ nm; at the end of the process (47 days) – there is only one maximum in the area $\lambda \approx 450 - 500$ nm. It is better seen when we get the average values of Δ on five rats at five stages of cancer disease development. The results of these calculations are shown in the graphs in fig. 1.

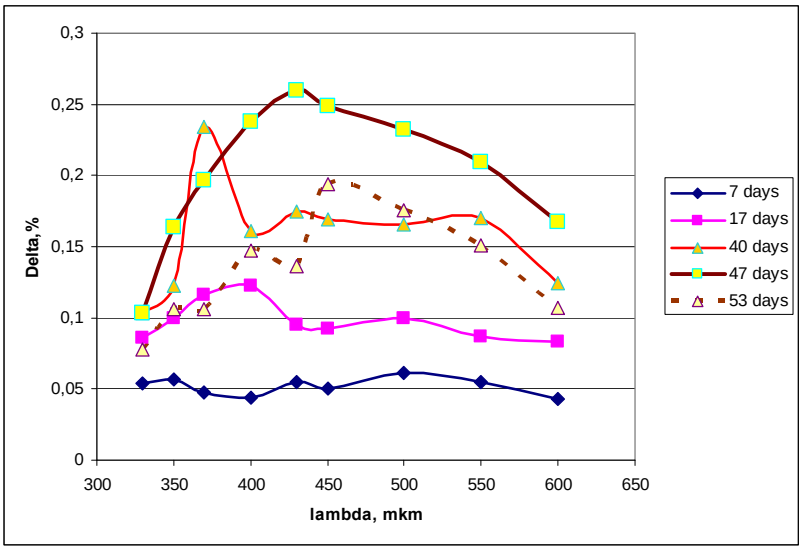

Fig. 1. The spectral magnitude dependence of the linear dichroism which is mean for all the rats: 1) 7 days; 2) 17 days; 3) 40 days; 4) 47 days; 5) 52 days after contamination

Conclusion

The following conclusions are made based on the results of the investigation:

1. It was found that in all the cases the linear dichroism appears in biotissues (human esophagus, muscular tissue of rats) with a cancer disease, the magnitude of which depends on the type of the tissue and on the time of the cancer process development.
2. The phenomenon of linear dichroism formation has a selective character: maximum values Δ are observed in the area $\lambda = 410 - 430$ nm and in the area $\lambda = 500 - 530$ nm; for the wavelength $\lambda < 300$ nm and $\lambda > 750$ nm Δ is almost zero or zero.
3. As the linear dichroism lacks in healthy tissues, the obtained results can have diagnostic value for detection and estimation of the stage of cancer disease development.

References

1. Angelsky, A.G. Ushenko, S.B. Ermolenko, D.N. Burcovets, V.P.Pishak, and Yu.A. Ushenko, *Optics and Spectroscopy*, 2000, 89, 799-804.
2. O.V. Angelsky, S.B. Yermolenko, C.Yu. Zenkova, and A.O. Angelskaya, *Appl. Opt.*, 2008, **47**, 5492-5499.

GPU-BASED SIMULATION OF NONLINEAR FLUORESCENCE IMAGING IN BIOTISSUE WITH INHOMOGENEOUS FLUOROPHORE DISTRIBUTION

A.R. Katichev and **E.A. Sergeeva**

Institute of Applied Physics RAS, Nizhny Novgorod, Russia, aleksey.katichev@gmail.com

Two-photon excited fluorescence microscopy (2PFM) is one of the most widely-used methods for deep biotissue imaging in vivo. It enables biologists to obtain structure images of a tissue under study with submicron spatial resolution up to 1 mm in depth. The method is based on non-linear fluorophores excitation by femtosecond laser pulses. Being applied to a fluorophore molecule with excitation wavelength λ, a high-intensity radiation with wavelength 2λ (usually near-IR band) induces a two-photon excitation process followed by fluorescence in VIS. Power of fluorescence signal is proportional to squared intensity of incident light. 2PFM is typically employed using femtosecond Ti:Sa sources operating in the spectral range of 700–1000 nm which lies within the so-called "transparency window" of most biological tissues. The range of 600–1300 nm is characterized by reduced scattering and absorption losses which provides higher penetration depth of NIR radiation compared to that of VIS and allows keeping submicron spatial resolution inside dense tissues [1, 2]. The range of 1000–1300 nm is potentially interesting for in vivo three-photon excitation or excitation of red fluorescence proteins; however higher-intensity sources at the wavelengths above 1000 nm are required [1].

A two-photon laser scanning microscope is similar to a confocal microscope except for absence of spatial filter (pinhole) needed for 2PFM. Due to its nonlinear nature two-photon fluorophore excitation takes place only within a focal volume of microscope objective. Therefore, every fluorescence photon is considered to be useful in contrast to the confocal scheme, where only ballistic photons used to form an image and scattered photons should be discarded. Hence, there is no need to "descan" fluorescence signal backwards to a second focus of confocal system where the pinhole is located. This allows placing a detector as close as possible to the collection optics, which results in a considerable increase of signal-to-noise ratio (SNR) of 2PFM scheme [3].

The scattering effect on multiphoton fluorescence microscopic imaging was investigated earlier with Monte Carlo (MC) simulation. As far as we know, modeling of image distortion and blurring with MPM has not been performed yet for turbid media with inhomogeneous fluorophore distributions. In this work we propose a simulation study of 2PFM image formation in such media.

The MC simulation is widely used for simulation of light propagation in highly scattering media such as biological tissues. The method is attractive by its simplicity and universality. One-layer tissues and multilayer tissues can be considered with both flat and complex boundaries [4], which is almost impossible with plural theoretical models.

The main disadvantage of the MC method is cost of computation time. To provide high SNR hundreds of millions photon trajectories should be calculated which could take hours of computations. Recently, several papers reported that implementation of graphics processing units (GPU) can dramatically improve performance of MC programs. In this study we demonstrate the benefits of this technique applied to the task of interest. Our code is based on the GPUMCML code by Alerstam *et al.* [5]. The original code has been modified in order to simulate a tightly focused Gaussian beam formed by microscope objectives with different numerical apertures (NA) and working distances. The ray-optics approach has been implemented to simulate correct spatial intensity distribution in Gaussian beam at arbitrary depth. Its concept is generation of a photon initial position within output aperture of the objective and its location in the focal plane. Each photon starts from the first point and is directed to the second point along a straight line trajectory. A probability density for location distributions in each of the two planes corresponds to intensity profile of focused Gaussian beam in the specific planes with account of given focal depth and NA value [6]. Simulation results demonstrate excellent agreement of the simulated beam profile with the theoretical Gaussian intensity distribution.

Using the described technique we performed MC simulation of 2PFM images in biological tissue. The first task was to simulate nonlinear excitation maps in biotissue with homogeneous distribution of fluorophore. Scattering of excitation light in biotissue is characterized by scattering coefficient μ_s or scattering mean free path $l_s = 1/\mu_s$. The results of simulation are shown in Fig. 1 for different focusing

depths of excitation beam with respect to the parameter l_s. For MC simulation of each map we employed $3 \cdot 10^8$ photons which took about 90 seconds using GPU compared to 5 hours using CPU single thread program. The maps demonstrate the effect of strong out-of focus fluorescence when the excitation beam is focused deep in highly-scattering tissue. In this case the efficiency of bulk two-photon excitation near the surface becomes comparable to the rate of two-photon excitation at focal point, which leads to considerable decrease of SNR. As the result, the effect of out-of focus fluorescence limits the maximum imaging depth of 2PFM.

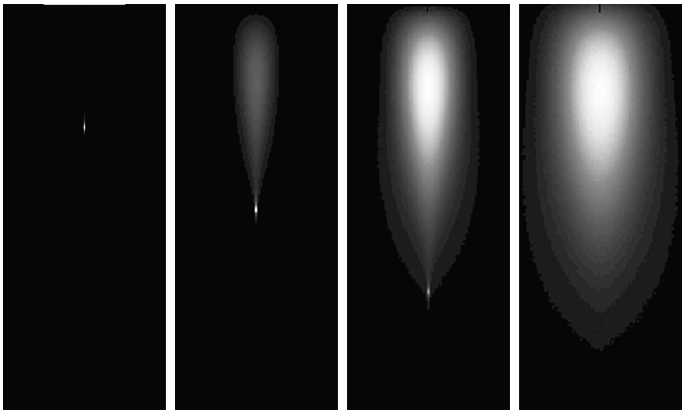

Fig. 1. Two-photon fluorescence maps for biotissue with homogeneous fluorophore distribution. Focus depth is equal to $3l_s$, $5l_s$. $7l_s$, $10l_s$, where l_s is scattering mean free path

The second task was to investigate the influence of out-of-focus fluorescence on the contrast of 2PFM images of biotissue with structured fluorophore distribution. We simulated images of regular grid of fluorescing "spots" with fluorophore concentration proportional to power sinusoidal distribution $C = C_0 \cdot \cos^n(\alpha x) \cos^m(\beta y) \cos^k(\gamma z)$. By varying the parameters of this function we can adjust size and shape of the spot, grid period and peak concentration. To simulate a fluorescent image a layer-by-layer convolution of fluorophore concentration with squared intensity of excitation light was computed. Summing images of individual layers gives the total 2PFM image of the structure (Fig. 2). It was demonstrated that for structured ("inhomogeneous") fluorophore distribution the maximum imaging depth is larger than for homogeneously fluorescing medium.

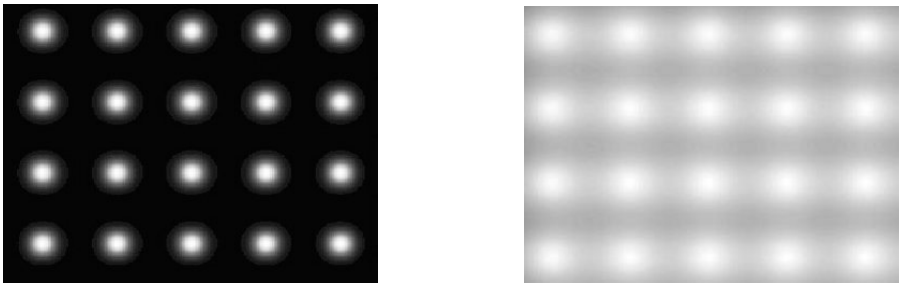

Fig. 2. Simulated 2PFM images of biotissue structured fluorophore distribution at different imaging depths: close to the surface (left); 5 l_s (right). The effect of SNR decrease due to out-of-focus fluorescence is evident

Acknowledgements

This work was partially supported by the Federal Target Program "Research and Scientific-Pedagogical Staff of Innovative Russia" (Project 02.740.11.0566).

References

1. X. Deng, M. Gu, *Appl. Opt.*, 2003, **42**, 3321-3329.
2. P. Theer, M.T. Hasan, W. Denk, *Opt. Lett.*, 2003, **28**, 1022-1024.
3. Y. Le Grand, A. Leray, T. Guilbert, C. Odin, *Optics Communications,* 2008, **281**, 5480-5486.
4. Q. Fang, *Biomed. Opt. Express*, 2010, **1**, 165-175.
5. E. Alerstam, W.C. Yip Lo, T.D. Han, J. Rose, et al., *Biomed. Opt. Express*, 2010, **1**, 658-675.
6. P.K. Milsom, *Applied Physics B: Lasers and Optics*, 2000, **70**, 593-599.

WIDE-BANDWIDTH TIME OF FLIGHT SPECTROSCOPY OF TURBID MEDIA

D. Khoptyar[1], M. Saleem[1,2], A.A. Subash[1], and **S. Andersson-Engels[1]**

[1]Dept. of Physics, Lund Institute of Technology, Box 118, S-221 00 Lund, Sweden
[2]National Institute of Lasers and Optronics (NILOP), Lehtrar Road Islamabad, Pakistan
dmitry.khoptyar@fysik.lth.se

Abstract: We report on current state of the art and performance characteristics of ultra-wide bandwidth time of flight spectrometer for biomedical and pharmaceutical applications developed in the Group of Biophotonics Lund University. The unique spectrometer is capable to deliver absorption/scattering spectra of turbid samples in the range from 650 nm up to 1400 nm. We illustrate outstanding performance of the instrument by reviewing number of applications in precise analysis of pharmaceuticals and biomedical diagnostics.

Advances in the instrumentation and measurements techniques for spectroscopy of turbid (highly scattering) materials in VIS and NIR regions are of paramount importance for the further developments in a wide range of the highly important biophotonics, biomedical and industrial applications. This covers e.g. non-invasive biomedical diagnostics and precise in-line treatment monitoring of such a deadly disease as cancer [1]. Emerging industrial applications of turbid media spectroscopy include novel analytical techniques for pharmaceutical research and development, advanced cost-effective methods for process analytical theology and fabrication quality control, analysis of food and agricultural products.

Basing on the recent advances in source and detector technology we have demonstrated [2] ultra-broadband photon time-of-flight spectrometer that is able to deliver continues absorption and scattering spectra of turbid samples in a singularly broad wavelength range from 600 nm up to 1400 nm. The spectrometer is based on the broadband photonic crystal fibber (PCF) super-continuous source (SCS) that provides short (ca. 30 ps) optical pulses electronically tunable from 600 nm up to ca 1800 nm using two acousto-optical tunable filters (AOTF's). Single photon counting avalanche photo-detector and micro-channel plate PMT's with InP/InGaAsP photo-cathode operated in time correlated single photon counting (TCSPC) mode are employed to precisely monitor photon time-of-flight (PTOF) distribution through the sample. Fitting the PTOF distribution with either analytical model for photon diffusion or by Monte-Carlo Simulations enables reconstruction of absorption and scattering coefficients in the sample. The complete spectral characterization of the absorption and scattering in the sample is obtained in the detector ranges from 600 nm to 1000 nm and from 950 nm to 1400 nm by tuning the wavelength of the probe pulse over the spectral range of interest.

Although capable to provide very precise and accurate information about scattering and absorption of the turbid sample PTOF measurements are highly sensitive to numerous factors such as the proper choice of the evaluation model, tight control over the measurement geometry and a priori information about sample optical properties (e.g. refractive index). Besides the precision of the measurements heavily relays upon precise timing calibration of the PTOFS system and in particular upon accurate determination of the instrumental response function (IRF). In many practical situations frequent IRF measurements are undesired or even impossible due to e.g. extra time needed or as extra source for the measurement distortions whereas complete temporal stabilization of the system appears to be unfeasible. Indeed clinical measures related to continuous monitoring of the patient sate may easily take hours before they may be interrupted for re-calibration; maintaining the high measurement precision (less than 1%) of the high resolution spectra scanning needed for analytical applications requires tight system synchronization over tens of minutes.

In order to comply with the tough requirements set by the applications on precision and accuracy of the measurements we introduce further advances of the spectrometer setup. To circumvent problems related to the apparent source and detector temporal drifts and to minimize uncertainties due to finite resolution of the TCSPC detection we have implemented new double path optical scheme that enables timing reference signal be recorded simultaneously with the signal (PTOF) or IRF measurements (see Fig. 1). The tiny fraction spitted from the probe pulse is routed over dedicated optical path towards the detector where it is superimposed over the PTOF or IRF signals. The amplitude of the timing

reference and its time delay with respect to the signal are controlled via dedicated attenuator and by the length of the reference optical path, respectively. The timing reference included (Fig. 2.) in the recorded PTOF and IRF signals is used along with fitting and evaluation of the PTOF data to precisely match the delay between PTOF and IRF. This considerably improves the precision of the measurements form few down to fraction of present.

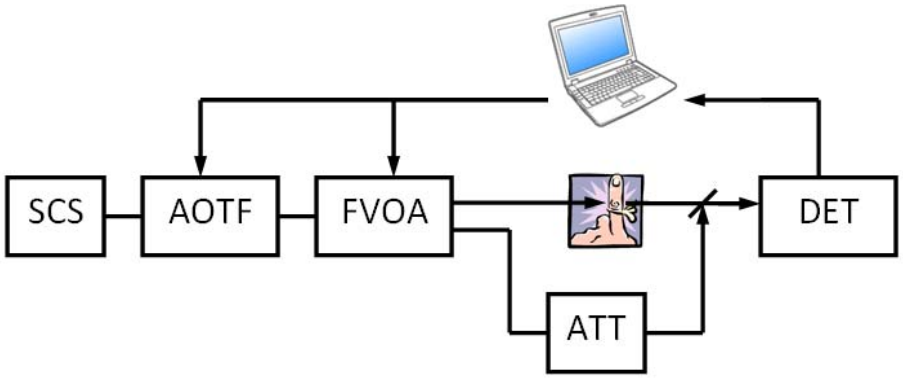

Fig. 1. Optical scheme of the instrument, only one detector channel is shown. Broadband output of SCS is filtered by computer controlled AOTF to provide spectrally narrow probe pulses at the selected wavelength. Variable optical attenuator (FVOA) adjusts the amplitude of the probe pulses that are sent to the sample. Tiny fraction (ca. −15 dB) of the probe pulse is used as a timing reference and routed over the dedicated optical path to the detector (DET). PC with TCSPC electronics controls the setup and collects the data

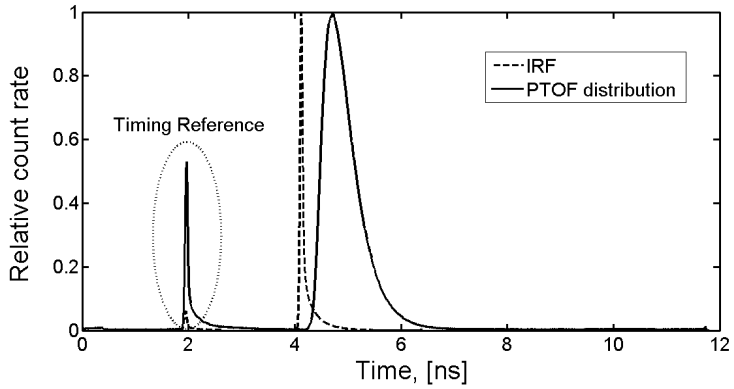

Fig. 2. En example of recorded IRF (doted line) and PTOF distribution (solid line). Both signals include timing reference that is used for precise PTOF to IRF synchronization along with evaluation of the optical properties

Enhanced accuracy in determination of the absorption and scattering properties of pharmaceuticals is crucial for precise evaluation of the tablet chemical composition (e.g. concentration of the active pharmaceutical ingredient) by the cost-efficient spectroscopic methods. This was so far hindered due to uncertainty in determination of the refractive index of the sample. In our contribution we discuss further strategies that can be employed in order to circumvent the problem. For example performing the measurements with modified boundary conditions is promising method that enables to deduce sample refractive index form series of PTOF measurements.

References

1. B.J. Tromberg et al., "Assessing the future of diffuse optical imaging technologies for breast cancer management", *Med. Phys*., 2008, **35**(6), 2443-51.
2. T. Svensson, E. Alerstam, D. Khoptyar, and S. Andersson Engels, "Near-infrared photon time-of-flight spectroscopy of turbid materials up to 1400 nm", *Review of scientific instruments*, 2009, **80**, 063105.

COLLAGEN CROSS-LINK MODIFIED FLUORESCENCE EXCITATION-EMISSION MATRIX OF ARTICULAR CARTILAGE

J. Kinnunen[1], **M. Hauta-Kasari**[1], **H.T. Kokkonen**[2], **P. Vahimaa**[1], **M. Lammi**[2], **J. Töyräs**[2], and **J.S. Jurvelin**[2]

University of Eastern Finland, [1]Joensuu / [2]Kuopio, Finland; jussi.kinnunen@uef.fi

Collagen cross-links are important factor of mechanical properties of articular cartilage. In this study the cross-linking of bovine articular cartilage was modified by threose and excitation-emission matrix of cartilage was measured. The treatment modified the intrinsic fluorescence and one new maximum might provide a window to observe pentosidine cross-linking independently from other cross-links.

Introduction

Articular cartilage is dynamic weight bearing tissue covering the bones in joints. It consists mainly of water and the solid matrix is composed of collagen and proteoglycans. When cartilage ages its mechanical properties change and joint diseases such as osteoarthritis (OA) become more common in elderly people. The advanced glycation end products (AGEs) are known to accumulate in articular cartilage where they cross-link the collagen network increasing its stiffness [1]. Diabetes is reported to enhance the accumulation of AGEs [2]. The AGE levels can be evaluated by the fluorescence of the tissue. A well characterized age-dependent AGE in human articular cartilage is pentosidine with a fluorescence maximum at 335/385 nm (excitation/emission) [3]. The high-performance liquid chromatography (HPLC) is used for pentosidine detection because several compounds in cartilage fluorescent at the same wavelength range. Such age-independent compounds, collagen pyridinium cross-links [4] and 2,6-dimethyldifuro-8-pyrone (DDP) [5] are easily mixed in detection unless HPLC is used. Earlier, four separate fluorescence maxima (280, 265, 330, 450 nm excitation / 310, 385, 390, 530 nm emission) have been measured in collagen powder [6]. In this study we introduced artificial AGE generation in bovine articular cartilage by incubating samples in a threose solution for two days. According to Verzijl et al. [1] threose generates at least N^{ε}-(carboxymethyl)lysine (CML), formyl threosyl pyrrole (FTP), threosidine and pentosidine. After the treatment the purified and papain digested collagen should demonstrate characteristic AGE fluorescence at 360/460 nm [1]. The current study investigates how the intrinsic fluorescence is modified during threose treatment and how the AGE generation can be observed without digestion or other additional processing of the cartilage.

Materials and methods

Articular cartilage samples were removed from six bovine (age = 18 months) knees from local abattoir. The samples were incubated in humidified 5% CO_2/95% air atmosphere at 37ºC for two days. Half of the samples (n = 12, 2/knee) were immersed in control liquid (DMEM low glucose 1 g/l no phenol red (Sigma Aldrich Co., MO, USA), with 100 U/ml penicillin, 100 µg/ml streptomycin, 10 mM HEPES buffer solution), 1 mM L-Glutamine (EuroClone S.p.A., Milano, Italy) and 70 µg/ml C-vitamine (Sigma Aldrich Co.). For the other half (n = 12, 2/knee), 100 mM L-threose (Sigma Aldrich Co.) was added to the liquid for cross-link formation. After incubation all the samples were changed into fresh control liquid and frozen (-20ºC) until the fluorescence measurements. During the incubation the samples were removed every five hours from the incubator for other optical measurements (data not shown). The fluorescence measurements were done using a bispectrometer with a 450 W Xe-lamp (Oriel M-66923 housing, Newport Corporation, Irvine, California, and Osram XBO 450 W bulb, Osram AG, Winterthur, Switzerland) attached to monochromator (DTMc300, Bentham Instruments Ltd., Berkshire, United Kingdom) for illuminating at the range 220-950 nm. The emitted and reflected light was collected in 0/45 – geometry into a spectrograph (PMA-12, Hamamatsu Photonics K.K., Hamamatsu City, Japan). A non-fluorescent reference was measured sequentially along the samples and its reflectance was used for calculating the bispectral radiance factor.

Results

The intrinsic fluorescence of control samples exhibited two clear maxima at 280/330 nm and 335/385 nm (Fig. 1, left). The threose treatment reduced the power of the original fluorescence and

after two days of incubation the maximum of fluorescence at 335/385 nm was decreased by 50 % (Fig. 1, right). At the same time new maxima were generated at 390/460 nm and 245/380 nm. The peak at 220/300 nm was related to control liquid in which the samples were immersed during the measurement. There was no fluorescence observed at wavelengths above 650 nm.

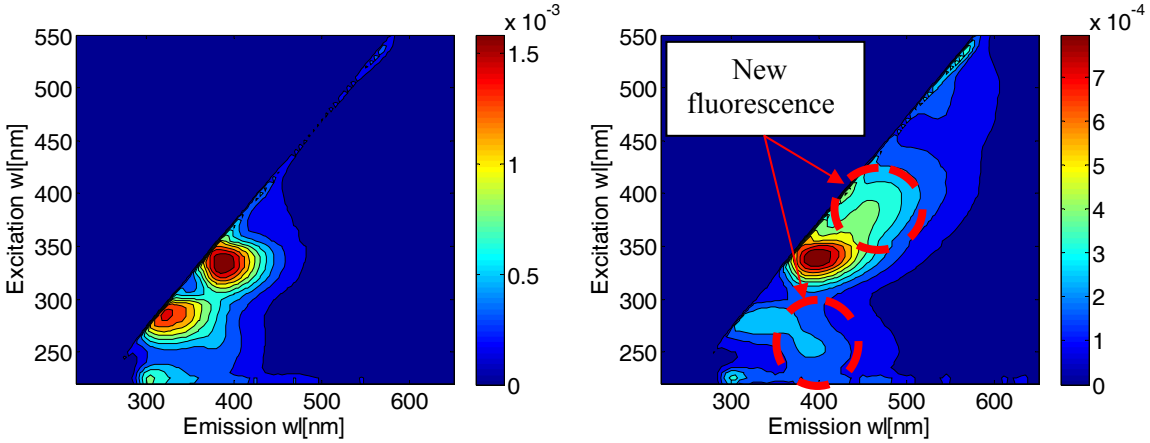

Fig. 1. Mean of bispectral radiance factor [1/nm] of the control (left, n = 12) and threose (right, n = 12) treated bovine articular cartilage after two days of incubation. Note the difference in colorbars

Discussion

As the samples were harvested from young animals, the original pentosidine levels were expected to be low [7]. Most of the fluorescence arises at 335/385 nm, due to collagen pyridinium cross-links and DDP. To our knowledge, no fluorescence related to CML has been reported in earlier studies. According to Prabhakaram *et al*. [8] the threosidine is fluorescent at 328/402 nm and it would not be separable from the pentosidine, pyridinium cross-links or DDP emission. The fluorescence at 335/385 nm decreased, even one could expect a generation of new fluorophores. This suggests that the compounds for the intrinsic fluorescence may turn into new compounds during threose treatment. L-threose reacts with proteins forming mainly FTP which generates fluorescence at 370/440 nm [9]. In that study FTP was generated much faster than pentosidine. It is likely that the new fluorescence at 390/460 nm is related to FTP. The new fluorescence at 245/380 nm, to our knowledge, has not been reported earlier. However, the absorption of threosidine [8] and purified pentosidine [10] increases at the wavelengths below 250 nm. The fluorescence can be related to either one. Since there is no intrinsic fluorescence or FTP fluorescence at 245/380 nm, it might provide a window to observe the pentosidine content independent from other AGEs.

Acknowledgements

The financial support from the Ministry of Education, Finland (University of Eastern Finland grant, projects 5741/Kuopio and 10102/Joensuu), Sigrid Juselius foundation and Kuopio University Hospital (EVO project 5041715/CT-rustokuvannus) is acknowledged.

References

1. N. Verzijl, J. DeGroot, C.B. Zaken, O. Braun-Benjamin, A. Maroudas, R.A. Bank, J. Mizrahi, C.G. Schalkwijk, S.R. Thorpe, J.W. Baynes, J.W.J. Bijlsma, F.P.J.G. Lafeber, and J.M. TeKoppele, *Arthritis Rheum*, 2002, **46**(1), 114–123.
2. V.M. Monnier, R.R. Kohn, and A. Cerami, *Proc. Natl Acad Sci. USA*, 1984, **81**, 583-587.
3. D.R. Sell, and V.M. Monnier, *J. Biol. Chem*., 1989, **264**(36), 21597-21602.
4. D. Fujimoto, K. Akiba, and N. Nakamura, *Biochem. Biophys. Res. Commun*., 1977, **76**(4), 1124-1129.
5. H.K. Gahunia, R. Vieth, and K.P.H. Pritzker, *J. Rheumatol.*, 2002, **29**(1), 154-160.
6. R. Richards-Kortum, and E. Sevick-Muraca, *Annu. Rev. Phys. Chem.,* 1996. **47**, 555–606.
7. Uchiyama, T. Ohishi, M. Takahashi, K. Kushida, T. Inoue, M. Fujie, and K. Horiuchi, *J Biochem.*, 1991, **110**(5),714-718.
8. M. Prabhakaram, Qi Cheng, M.S. Feather, and B.J. Ortwerth, *Amino Acids*, 1997, **12**, 225-236.
9. R.H. Nagaraj, V.M. Monnier, *Biochim Biophys acta*, 1995, **1253**, 75-84.
10. D. Słowik-Żłka, K. Safranow, V. Dziedziejko, H. Bukowska, K. Ciechanowski, and D. Chlubek, *J. Biochem. Biophys. Methods*, 2004, **61**(3), 313-329.

Invited

CONTRAST ENHANCEMENT IN OPTICAL TOMOGRAPHY OF BIOTISSUES

M.Yu. Kirillin[1], **P.D. Agrba**[1,2], **E.A. Sergeeva**[1], **E.A. Bakshaeva**[2], **M.V. Shirmanova**[3], **M.A. Sirotkina**[3], and **V.A. Kamensky**[2]

[1]Institute of Applied Physics RAS, 603950, Ulyanov St., 46, Nizhny Novgorod, Russia
[2]N.I. Lobachevsky State University of Nizhny Novgorod, 603950, pr. Gagarina, 23, Nizhny Novgorod, Russia
[3]Nizhny Novgorod State Medical Academy, 603005, Minin and Pozharsky sq., 10/1, Nizhny Novgorod, Russia
e-mail: mkirillin@yandex.ru

Optical coherence tomography (OCT) is a rapidly emerging non-invasive high-resolution (down to 1 μm) imaging technique being recently introduced to clinical practice [1]. However, this technique has certain limitations when imaging inner structure of non-transparent biotissues originating mostly from the multiple light scattering. These limitations are manifested by comparatively low imaging depth (not more than 1.5 mm in skin) and low image contrast at such depth. Usually, optical clearing agents are used in order to diminish the effect of multiple scattering in biomedical optical imaging techniques [2]. However, for backscattering techniques, such as OCT, optical clearing may result in a decrease of a useful signal due to a decrease in the number of backscattered photons.

In the present talk we discuss alternative ways of contrast enhancement in OCT images, such as administration of nanoparticles solutions, mechanical compression and vibratory action.

Application of nanoparticles to the biotissue surface or their target delivery results in heterogeneous distribution of nanoparticles within biotissue. Being small scatterers, nanoparticles demonstrate much more isotropic scattering phase function compared to strongly forward-elongated scattering phase functions of biotissue components, which results in local increase of probing radiation backscattering from the regions where the nanoparticles are present. Consequently, the OCT-signal from the areas containing nanoparticles increases thus causing contrasting of these areas in the OCT-images. The experiments in vivo on laboratory animal skin demonstrate the contrasting effect of nanoparticles presence [3, 4]. The origin of contrast is confirmed by results of Monte Carlo simulations. Administration of nanoparticles allows increasing contrast of the epidermis-dermis junction as well as hair bulbs and glands in OCT images of skin. After application of nanoparticles the contrast increases, reaching its maximum in 2.5-3 hours depending on the nanoparticles type.

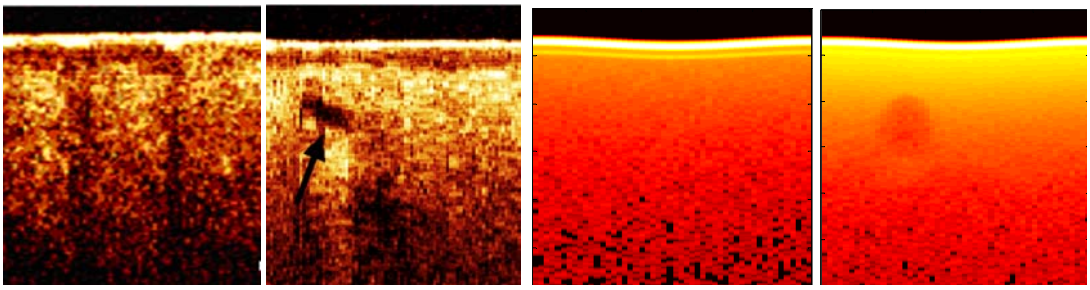

a b c d

Fig. 1. Experimental (a, b) and Monte Carlo simulated (c, d) OCT images of swine skin before (a, c) and after (b, d) application of gold nanoshells

In the case of application of mechanical compression to a biotissue non-uniform compression of biotissue layers occurs due to heterogeneous distribution of mechanical and elastic properties within tissue. This fact results in contrast of interlayer boundaries in OCT-images due to different alteration of scattering properties induced by compression. The effect of mechanical compression was studied in human rectum samples ex vivo [5] and human thin skin samples in vivo [6]. Application of mechanical compression allows contrast of layer boundaries to be increased in OCT-images of human rectum ex vivo and of the epidermis-dermis junction in OCT images of skin in vivo. After application of mechanical compression the contrast increases and then is kept constant until the pressure is removed. The results of ex vivo study were confirmed by results of Monte Carlo simulations [5].

Transversal vibratory action on the OCT-probe during scanning results in spatial averaging of the A-scans assembling the OCT-image. In some cases such averaging could help to get rid of so-called

speckled structure of the OCT-image originating from coherent properties of probing radiation. We applied transversal vibratory action (in 80–100 Hz band) to OCT-probe when imaging human thin skin and demonstrated a significant decrease in the speckle noise level from analysis of OCT-image histograms.

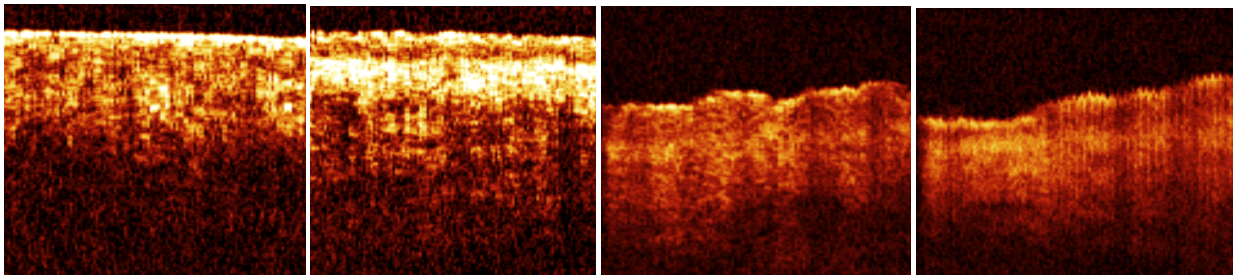

a b c d

Fig. 2. OCT images of human skin before (a) and after (b) application of mechanical compression and without (c) and with (d) vibratory action

Another optical tool for biomedical imaging and diagnostics currently being at preclinical stage is diffuse optical tomography (DOT). The DOT technique is based on illumination of the studied object at one or several wavelengths and detection of radiation scattered within the object. Number and configuration of sources and detectors may vary significantly. Application of DOT is usually aimed at detecting areas with different scattering or absorption coefficients within biotissues. Consequently, nanoparticles in the case of target delivery can serve also as contrasting agents because being target delivered to the specified areas, they can locally change optical properties, providing contrast of these areas in DOT-images. We performed Monte Carlo studies which corroborate the possibility of nanoparticles application for contrasting in DOT. These results were confirmed by pilot experimental study.

Acknowledgements

The work was supported by grants from the Russian Foundation for Basic Research (Nos. 10-02-00744, 10-08-00744 and 11-02-01129), grant of the President of the Russian Federation MK-1127.2010.2, FTP "Scientific and Scientific-Educational Brainpower of Innovative Russia" (projects Nos. 14.740.11.0253, 02.740.11.0086, 02.740.11.0839), and grant of the Government of Russian Federation No. 11.G34.31.0017. The authors are grateful to Dr. E. Zagaynova and Dr. A. Abelevich (Nizhny Novgorod State Medical Academy).

References

1. *Handbook of Optical Coherence Tomography*, Edited by B. E. Bouma, G. J. Tearney, New York: Marcel Dekker, 2002.
2. V.V. Tuchin, *Optical Clearing of Tissues and Blood*, SPIE Press, Bellingham, WA, 2006.
3. M.Yu. Kirillin, M.V. Shirmanova, M.A. Sirotkina, M.L. Bugrova, B.N. Khlebtsov, and E.V. Zagaynova, *J.Biomed. Opt*., 2009, **14**, 021017.
4. M.Yu. Kirillin, P.D. Agrba, M.A. Sirotkina, M.V. Shirmanova, E.V. Zagaynova, and V.A. Kamensky, *Quantum Electronics*, 2010, **40**(6), 525-530.
5. P.D. Agrba, M.Yu. Kirillin, A.I. Abelevich, E.V. Zagaynova, V.A. Kamensky**,** *Optics and Spectroscopy,* 2009, **107**(6), 853–858.
6. M.Yu. Kirillin, P.D. Agrba, and V.A. Kamensky, *Journal of Biophotonics*, 2010, **3**(12), 752-758.

NUMERICAL ANALYSIS OF CP-OCT IMAGES IN CLINICAL STUDY

E.B. Kiseleva[1], **N.D. Gladkova**[1], **O.S. Streltsova**[1], **N.S. Robakidze**[2], **I.B. Balalaeva**[3], **M.M. Karabut**[3], **E.V. Gubarkova**[1], **V.M. Gelikonov**[4], and **G.V. Gelikonov**[4]

[1]Institute of Applied and Fundamental Medicine, Nizhny Novgorod State Medical Academy
Nizhny Novgorod, Russia, kiseleva84@gmail.com
[2] Saint-Petersburg Medical Academy of Postgraduate Education, Saint-Petersburg, Russia
[3]Lobachevsky State University of Nizhny Novgorod, Nizhny Novgorod, Russia
[4]Institute of Applied Physics RAS, Nizhny Novgorod, Russia

Numerical analysis (NA) of the medical images can significantly upgrade the informativity of the method and objectivity of the results. This study is devoted to quantitative analysis of the cross-polarization OCT (CP OCT) images of different bladder and oral mucosa pathological states. CP OCT is a special OCT modality which acquires images resulting from cross-polarization and co-polarization scattering simultaneously. Benign states are generally characterized by OCT images with high contrast between epithelium and connective tissue, but some benign pathology also demonstrates structureless co-polarized images (CoPI) [1]. Differential diagnosis of Crohn's disease and ulcerative colitis is difficult because even the "gold standard" histology doesn't necessarily offer definitive distinguishing features [2]. The cross-polarized image (CrPI) provides information about microstructural and biochemical alterations in depolarizing tissue components (collagen). The goal of this research is to analyze numerically the CP OCT images in two independent clinical studies: the bladder and oral mucosa states.

Materials and methods

We used a CP OCT device described in V. and G. Gelikonov's paper [3] in two groups. 96 patients with flat local lesions in the bladder (80 benign & 16 malignant states) had visually reduced contrast in the CoPI, so the diagnostics is complicated in this group. The second group included 29 patients with inflammatory intestine disease (17 patients with Crohn's disease & 12 patients with ulcerative colitis) and their oral mucosa was examined. The control group contained healthy volunteers: 15 in the bladder research and 11 in oral mucosa testing. Biopsy was taken from all the CP OCT scanned zones. Histological stain with H&E confirmed the diagnosis, and picrosirius red (PSR) staining described the collagen condition. CP OCT images of the bladder and oral mucosa were processed and analyzed numerically using ImageJ software.

Results

The conducted NA has revealed, that in 4 of 5 examined benign states of the bladder (see the footnote[1]) the contrast between the layers in the CoPI is significantly lower than in norm ($p < 0.05$, except the cystitis with ulceration), but significantly higher ($p < 0.05$) than in the case of malignant processes (fig. 1a). The contrast of 3.0 dB (in the 2.5–3.5 dB range) with peak efficiency indicates neoplasia (fig. 1b). The sensitivity of the CP OCT method is 0.97, specificity – 0.82, diagnostic accuracy – 0.94.

The analysis of the signal brightness in the CrPI in the same clinical groups manifests its certain descent in 4 of 5 groups in contrast to norm ($p < 0.05$, except atrophic cystitis) (fig. 2a). The signal brightness from the submucous layer in the CrPI of 2.8 dB (in the 2.5–3.0 dB range) is a diagnostic criterion for detection of neoplasia (fig. 2b). The sensitivity of the CP OCT method is 0.84, specificity – 0.92, diagnostic accuracy – 0.85.

A similar approach is effective for NA of a signal in the CP OCT images for differential diagnosis of Crohn's disease and ulcerative colitis (fig. 3a). The signal brightness in the CrPI for diagnosis of

[1] States of the bladder with reduced contrast of tissue layers: atrophic cystitis (AC), cystitis with proliferation in submucosa (PC), cystitis with Brunn's nests (Bn), cystitis with squamous cell metaplasia (MC), cystitis with ulceration (UC), severe dysplasia (Dis III), cancer *in situ* or flat transitional cell carcinoma (ICr). Statistically significant difference from norm (*) and of malignant states (º) from benign conditions, $p < 0.01$ (one-dimensional t-Student criterion); º º – statistically significant difference of malignant states from benign conditions, $p < 0.05$ (one-dimensional t-Student criterion).

Crohn's disease is 7.5 dB (within the 7.0–8.0 dB range). The sensitivity of the CP OCT method is 0.72, specificity – 0.89, diagnostic accuracy – 0.78 (fig. 3b).

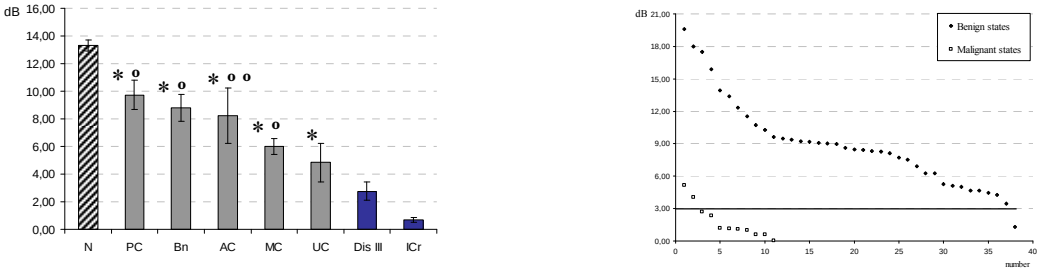

a b

Fig. 1. Contrast between layers in co-polarized images of different bladder states

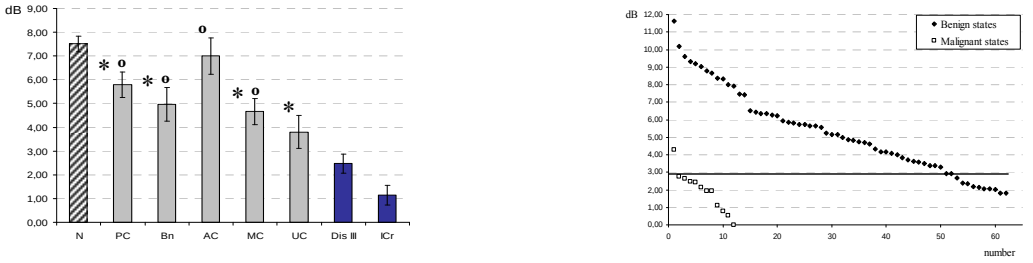

a b

Fig. 2. Brightness of a signal in the CrPI of different bladder states

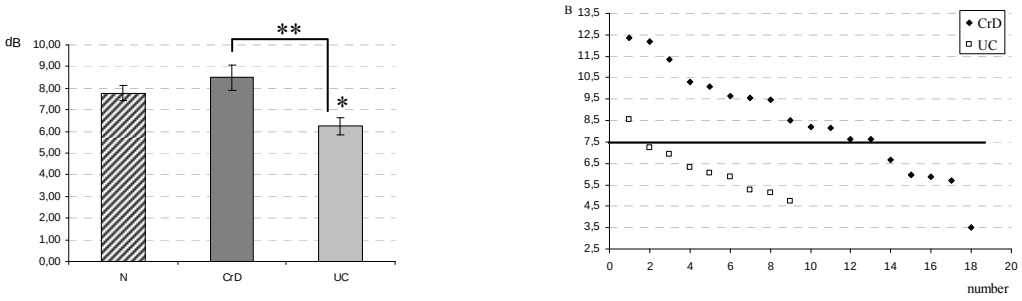

a b

Fig. 3. Brightness of a signal in the CrPI of the cheek mucosa in norm (N), Crohn's disease (CrD), ulcerative colitis (UC). * – statistically significant difference from norm, $p < 0.01$ (one-dimensional t-Student criterion); ** – statistically significant difference between the specified states, $p < 0.01$ (one-dimensional t-Student criterion)

Conclusion

Numerical analysis of the key characteristics of the CP OCT images upgrades the informative value of the method and objectifies pathological changes of the bladder and oral mucosa.

Acknowledgements

This work has been supported by the Russian Foundation for Basic Research (project 10-02-01175), State Contract of the Federal Target Program "Scientific and Scientific Educational Brain Power of Innovative Russia" (No. 02.740.11.5149) and the Grant of the Russian Federation Government (contract No. 11.G34.31.0017).

References

1. E.V. Zagaynova, N.D. Gladkova, O.S. Streltsova, et al. *Optical Coherence Tomography in Urology*. Editors: Wolfgang Drexler, James Fujimoto. *Optical Coherence Tomography*, Berlin Heidelberg, Springer, 2008, 1241–1268.
2. J. Zonderman and R. Vender. *Understanding Crohn Disease and Ulcerative Colitis*, University Press of Mississippi, 2000, p. 253.
3. V.M. Gelikonov and G.V. Gelikonov, *Laser Phys. Lett.*, 2006, **3**, 445.

FLUORESCENCE IMAGING WITH LIFETIME AND SPECTRAL RESOLUTION FOR DETECTION OF RFP-EXPRESSED TUMORS

M.S. Kleshnin[1], **I.I. Fiks**[1], **I.V. Turchin**[1], **I.V. Balalaeva**[2], and **A.P. Savitsky**[3]

[1] Institute of Applied Physics RAS, Nizhny Novgorod, Russia, m.s.kleshnin@gmail.com
[2] N.I. Lobachevsky State University of Nizhny Novgorod, Nizhny Novgorod, Russia
[3] A.N. Bach Institute of Biochemistry RAS, Moscow, Russia

Introduction

Small animal fluorescence imaging is widely used for in vivo investigations of experimental tumors. Reflectance technique [1] allows investigating the superficial fluorescing tumors. Projection imaging [2] in transillumination mode allows investigating the fluorescing tumors located deep in the animal body. Fluorescence diffuse tomography (FDT) [3] enables 3D imaging of fluorescing tumors using a set of different projections of the tissue.

The efficacy of fluorescence imaging technique can be increased if one uses additional information about light propagation in biological tissues. Small animal fluorescence imaging with lifetime resolution allows differentiating fluorophores by this parameter, thus increasing the investigations informativity. FDT technique with spectral resolution utilizes optical dispersion phenomenon which causes spectral changes of a fluorescent signal.

FDT setup for small animal fluorescence lifetime imaging

We created an experimental setup for small animal fluorescence imaging which combines the reflectance technique with lifetime resolution and fluorescence diffuse tomography [4] (Fig. 1). To achieve time resolution we use a fiber-based 525 nm pulsed laser with 500 ps pulse width and the repetition rate of 200 kHz. As a detector we use Multichannel Photocathode (MCP-based ICCD, Stanfordcomputeroptics, USA) that allows measurements with the time gate up to 200 ps. To obtain data for 3D reconstruction of the fluorophore concentration the investigated object is scanned in transilluminative configuration by moving the optical fiber with collimator using stepping motors. The results of 3D reconstruction of DsRed2 expressed tumor in NUDE mouse in vivo will be presented.

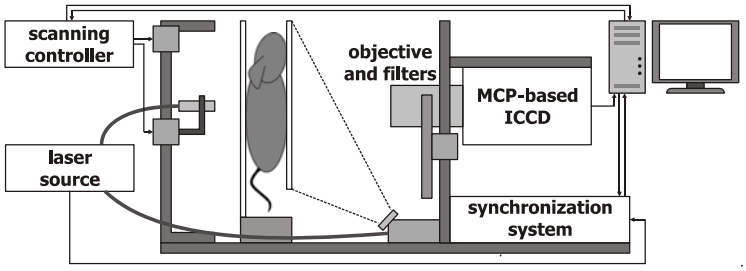

Fig. 1. FDT setup for small animal fluorescence lifetime imaging

Using different time delays between laser pulses and MCP gate it is possible to obtain time dependence of fluorescence intensity (Fig. 2) for lifetime calculation. The obtained lifetime of the TurboRFP expressed tumor in NUDE mouse is in accordance with the data obtained from the standard microscopic measurements of the same cancer cell line. The obtained results have demonstrated the possibility of identifying an RFP by registering fluorescence lifetimes.

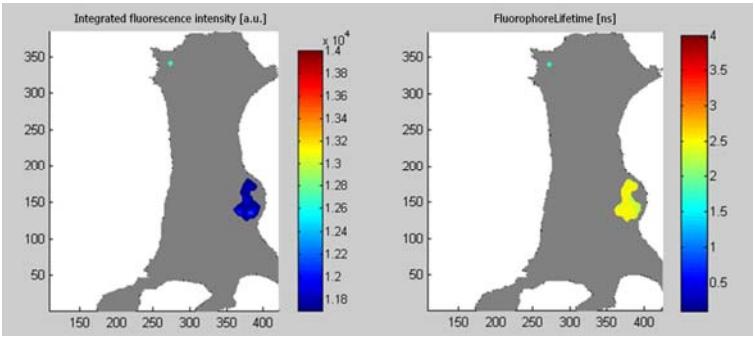

Fig. 2. The results of *in vivo* whole-body reflectance imaging with lifetime resolution of subcutaneous TurboRFP expressed tumor in NUDE mouse

Spectrally resolved FDT setup for small animal imaging

Absorption and reduced scattering coefficients are the basic parameters describing propagation of light radiation in biotissues. Scattering coefficient weakly depends on wavelength, but absorption coefficient has a strong dispersion in the range of wavelengths of 500-650 nm. Absorption dispersion causes spectral shape changes of the optical radiation propagating through biological tissues. This phenomenon can be used for 3-D reconstruction of the fluorophore concentration.

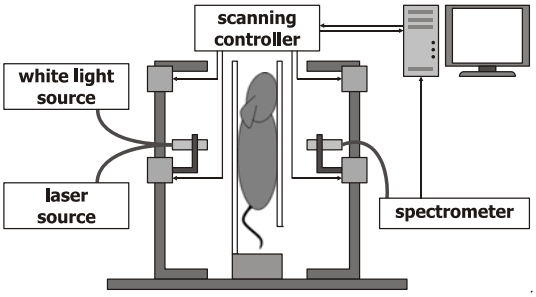

Fig. 3. Spectrally resolved FDT setup for small animal imaging

The experimental setup for spectrally resolved fluorescence tomography based on dispersion of biotissue absorption has been created [5] (Fig. 3). An animal is scanned in the transilluminative configuration by a single source-detector pair. The spectrum of optical radiation propagated through the investigated object is registered by a spectrometer (QE65000, Ocean Optics, USA) in each position. In our experiment we scanned experimental animals with RFP-marked tumor. We used the white light source which gives information about biotissue absorption and scattering and the laser source which excites RFP.

The obtained results have shown a basic opportunity of fluorescence tomography based on dispersion of biotissue absorption (Fig. 4). If optical parameters of a biological tissue are well known it is possible to make 3-D reconstruction of spatial distribution of fluorophore concentration without angular resolution in 2-D images of the examined object by changing the spectral shape of the registered fluorescence.

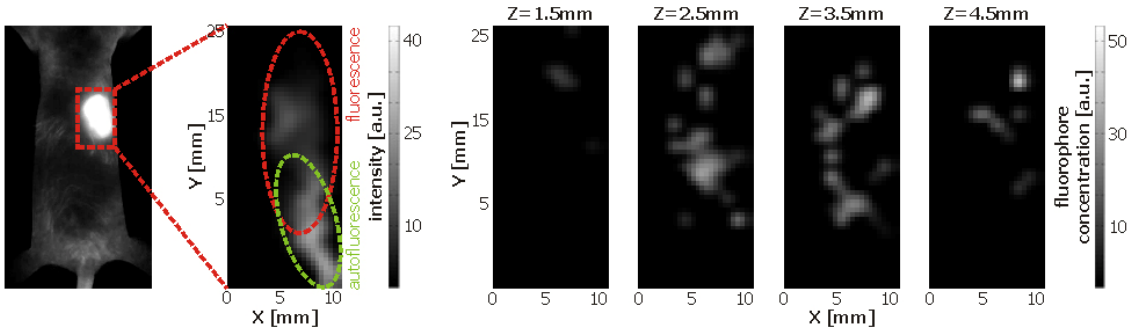

Fig. 4. Reconstruction of deeply located fluorescent tumor using the spectrally resolved FDT technique

Acknowledgements

This work was partly supported by the Russian Foundation for Basic Research (10-02-01109), by the Science and Innovations Federal Russian Agency (projects 02.740.11.0086, 16.512.11.2140, 16.120.11.1909-MK), and by the Program of Fundamental Researches of the Presidium of the Russian Academy of Sciences.

References

1. V. Ntziachristos, J. Ripoll, L.V. Wang, R. Wesslender, *Nat. Biotechnol.*, **23**(3), 313-320.
2. V. Ntziachristos, G. Turner, J. Dunham et al, *J. Biomed. Opt.*, **10**(6), 064007.
3. I.V. Turchin, V.A. Kamensky, M.S. Kleshnin et al, *J. Biomed. Opt.*, **13**(4), 041310.
4. A.L. Rusanov, T.V. Ivashina, L.M. Vinokurov et al, *J. Biophotonics*, **3**(12), 774-783.
5. M.S. Kleshnin, I.V. Turchin, *Quantum Electronics*, **40**(6), 531-537.

STUDY OF RADIATION DAMAGE OF CONNECTIVE TISSUE STRUCTURES BY OPTICAL METHODS

M. Kochueva[1], **V. Kamensky**[2], **N. Ignatjeva**[3], **O. Zakharkina**[4], **K. Kulabukhova**[5], and **A. Maslennikova**[1]

[1] Nizhny Novgorod State Medical Academy, Russia, marina.kochueva@mail.ru
[2] Institute of Applied Physics RAS, Nizhny Novgorod, Russia
[3] M.V. Lomonosov Moscow State University, Russia
[4] Institute for Laser Information Technologies RAS, Moscow, Russia
[5] N.I. Lobachevsky Nizhny Novgorod State University, Russia

Introduction

Connective tissue damages are known to play a significant role in the development of normal tissue radiation damage. However, there is little basic information available on how gamma irradiation alters collagen organization at different levels of its structural hierarchy. The goal of the study was to evaluate changes of collagen network organization at different levels of its hierarchical structure depending on dose and time after irradiation.

Materials and methods

Rat tail tendon as an example of a highly ordered collagen structure was chosen as a model. Irradiation was delivered in vivo under general anesthesia (Zoletyl 50 mg/kg) using a ^{60}Co external beam therapy unit in order to study the progression of collagen network damage as the gamma dose increased from 2 to 10 Gy (2, 4, 6, 8, 10 Gy, respectively). One day and one week after irradiation, tails were cut under anesthesia and tendon samples were excised.

The alteration at the molecular level was investigated using the susceptibility to trypsin degradation. Proteolytic enzyme trypsin induces depolymerization only of the damaged collagen molecules, while intact molecules are resistant to its influence.

The damage at the molecular and microfibril levels was estimated using differential scanning calorimetry (DSC). The thermal analysis was carried out in DSC20 and DSC30 cells of METTLER TA 4000 calorimeter. Heating was performed up to 95^{0}C with the rate of 10 K/minutes.

Changes at the fibril and bundle level were evaluated using fluorescent confocal microscopy (LSM 510 Meta (Carl Zeiss)) with second harmonic generation (SHG) imaging.

Cross polarization optical coherence tomography (CP OCT) was used for valuation of changes of general tendon architectonics. CP OCT imaging was done using the optical coherence tomograph developed at the Institute of Applied Physics of the Russian Academy of Sciences (Nizhny Novgorod).

Results

One day after irradiation collagen was significantly more susceptible to trypsin digestion compared to non-irradiated samples, suggesting the treatment induced distortion of the rigid molecular structure of collagen. A week after the treatment the irradiated samples demonstrated a higher resistance to trypsin digestion than a day after irradiation, but lower than the intact samples.

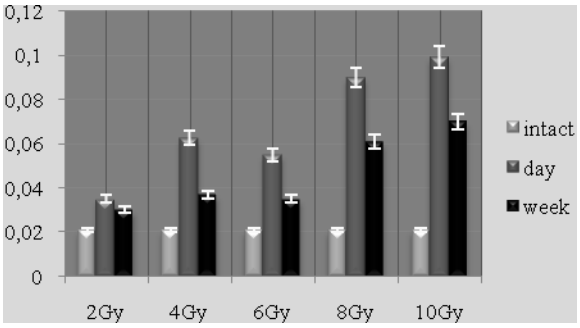

Loss of mass of tendon depending on dose and time after irradiation

The calorimetric measurements showed that the helix–coil transition in irradiated samples occurred at a lower temperature (denaturation temperature Td was 60-62^{0}C) than in non-irradiated (Td = 67 ± 1^{0}C) ones, demonstrating the presence of destabilized collagen fraction. A week after irradiation, the increase of denaturation temperature was observed, positively depending on radiation dose.

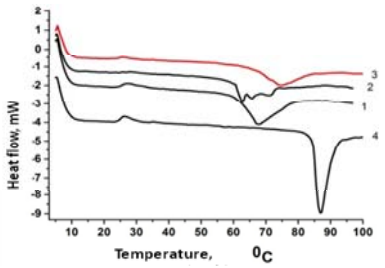

Typical DSC-termograms of tendon samples:
1 – intact; 2 – 2 Gy, one day;
3 – 4 Gy, one week; 4 – 8 Gy, one week

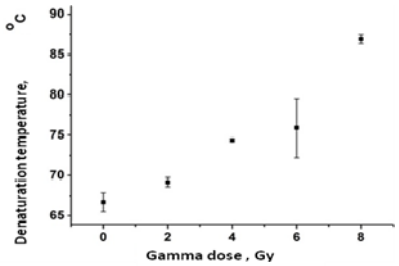

Collagen denaturation temperature
a week after irradiation depending on total dose

On SHG images of the intact samples, the well-ordered structure of the fibers that were densely packed into parallel primary and secondary bundles was clearly observed. The structure of the primary fibers remained in the images of the irradiated samples; the secondary bundles, however, became considerably disperse; that was a characteristic feature of the crimps areas. Substantial growth of a number of such crimps, in comparison with the intact samples, was a prominent feature of samples a week after irradiation. No qualitative difference was observed between irradiated samples, although the part of areas with destructive stratification increased depending on irradiation dose.

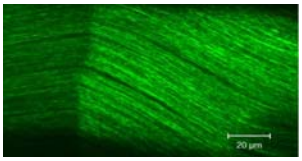

Intact sample

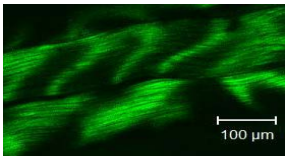

2 Gy, a day after irradiation

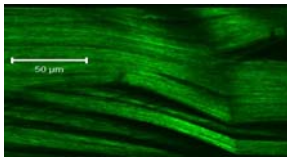

6 Gy, a day after irradiation

The general tendon architectonics, according to CP OCT data, was not altered independent of the dose and time after irradiation.

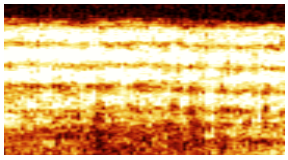

non-irradiated

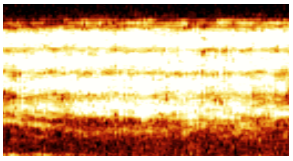

2 Gy, a day after irradiation

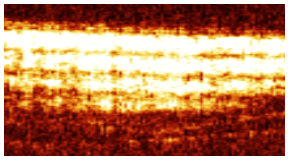

8 Gy, a day after irradiation

Conclusions

The study revealed heterogeneous changes of tendon collagen network depending on time after irradiation. A day after irradiation, native conformations of triple-helical collagen macromolecules and microfibriles were disorganized without infringement of fiber packing. A week after irradiation, the collagen structure was restored with partial separation of secondary bundles.

Acknowledgements

This work was partly supported by the Russian Foundation for Basic Research (10-02-00748-a).

References

1. Bidhu K. Mohanti, M. Bansal, *Supportive Care in Cancer*, 2005, **13** (10), 775-780.
2. P. Bruckner, D.J. Prockop, *Anal Biochem*., 1981, **110**, 360-8.
3. Cancer Therapy Evaluation Program, Common Terminology Criteria for Adverse Events, version 3.0, DCTC, NCI, NIH, DNNS. June 10, 2009 (htpp://ctep.cancer.gov).
4. V.M. Gelikonov, G.V.Gelikonov, *Laser Phys. Lett*., 2006, **3**, 445-451.
5. C.A. Miles, R.J. Wardale, H.L. Birch et al., *Equine Vet J*., 1994, 26, 291-296.
6. I. Rayment, W.R. Rypniewski, K. Schmidt-Base, et al., Science, 1993, **261**, 50-58.

GENETICALY ENCODED FRET SENSOR FOR MATRIX METALLOPROTEINASES

G.D. Lapshin[1], **T.V. Ivashina**[2], **L.M. Vinokurov**[3], **A.L. Rusanov**[1], and **A.P. Savitsky**[1]

[1] Institute of Biochemistry RAS, Moscow, Russia, sadsaviour@gmail.com
[2] IBPM RAS, Pushino, Russia,
[3] BIBC RAS, Pushino, Russia

Matrix metalloproteinases

The founding member of the matrix metalloproteinases (MMP) family, collagenase, was identified in 1962 by Gross and Lapier, who found that tadpole tails during metamorphosis contained an enzyme that could degrade fibrillar calagen 1,2. Subsequently, an interstitial collagenase, colagenase-1 or MMP1, was found in diseased skin and synovyum. In vitro MMP1 initiates degradation of native fibrillar collagens, crucial components of vertebrate exracellular matrix (ECM). Futher research led to the discovery of a family of structurally related proteinases (23 in human, 24 in mice), now referred to as the MMP family. Metalloproteinases obtained their name after metal binding region, critical for enzymatic activity.

Interest in MMPs increased in the late 1960s and early 1970s following observations that MMPs are upregulated in diverse human diseases including rheumatoid arthritis and cancer. MMPs can promote cancer progression by increasing cancer cell growth, migration, invasion, metastasis and angiogenesis. MMPs exert these effects by cleaving a diverse group of substrates, which include not only structural components of the extracellular matrix, but also growth-factor-binding proteins, growth factor –binding precursors, receptor tyrosine kinases, cell-adhesion molecules and other proteinases.

Two metalloproteinases – MMP-2 and MMP-9 are usually associated with metastasis. This is complex process: cancer cell should overcome many tissue barriers before it became new metastasis tumor. It is hard to model tissues *in vitro*, that's make development of *in vivo* MMP activity sensors very important.

For investigation of MMP behavior synthetic oligopeptides are used. Special design of these peptides makes them fluorescent after cleaving by MMP. However, the production of these probes requires complicated and costly synthetic chemical technology. Previous studies have demonstrated that it is possible to sandwich responsive proteins between two fluorescent proteins (FPs), capable of fluorescence resonance energy transfer (FRET). Energy transfer between FPs is possible if emission spectrum of one FP (energy donor) overlap excitation spectrum of another FP (energy acceptor). Cleavage of linker between FPs change distance between FPs and, as a result, change FRET efficiency. This change could be measured by increase of donor fluorescence or increase of donor fluorescence lifetime. To provide reliable signal for such measurements acceptor with low quantum yield are most useful choice.

Sensor design

In our laboratory we design two sensor for gelatinases (MMP2 and MMP9). Sensors contain MMP signal peptides for extracellular transport of recombinant protein, two fluorescent proteins: TagRFP and KFP (FRET pair) and linker with 8 amino acids substrate site. We used red fluorescent proteins, because tissues are most transparent in long wavelength part of spectra.

Different studies shown that MMP degrade a number of natural substrates and some of them are cleaved by different proteinases.

To understand exact role of each member of MMP family specific sensors should be design. But direct mechanism of substrate recognition is still unclear. Several studies show that amino acid sequence of substrate subsite, which is recognized by MMP active site, dramatically influence hydrolysis. Some authors investigate this dependence on synthetic oligopeptides. To maximize specificity for MMP-2 and MMP-9 we choose amino acids, preferable for MMP of interest:

Gly-Pro-Leu-Gly-Met-Leu-Ser-His for MMP-2
Gly-Pro-Leu-Gly-Tyr-Phe-Gly-Thr for MMP-9

Sensor properties

For characterization of physical and spectral properties of recombinant protein, prokaryotic vector containing sensor sequence without signal peptide was produced. Vector was based on pET22b (Invitrogen) plasmid. Recombinant protein were expressed in *E.coli* and then purified by ion-exchange chromatography and gel filtration.

Pure recombinant protein was characterized by electrophoresis and spectrophotometry. Electrophoresis in denaturation conditions showed that protein divides into two bands with molar masses 37 kDa and 17 kDa. This means that KFP is mature, because in this case mature chromophore breaks polypeptide chain.

Sensor has absorption spectra with maximum between maximums of TagRFP and KFP. It confirms maturation of both TagRFP and KFP in recombinant protein.

KFP have quantum yield approximately 500 times smaller than TagRFP's yield. It means that fluorescent properties of sensor should be close to properties of TagRFP. Our measurement approved this theory. Recombinant protein have extinction maximum at 555 nm and emission maximum at 582 nm.

Sensor for MMP-2 was incubated with active MMP-2 to test cleavage site for this metalloproteinase. Probes from reaction solution were analyzed by electrophoresis. It was shown that metalloproteinase cleave site and 37 kDa band, that corresponds to intact sensor, gradually disappear.

Sensor cleavage was also approved by 2 times increase of fluorescence of recombinant protein after 24 hour incubation with target metalloproteinase. Measurements of fluorescence lifetime of sensor during incubation with MMP-2 demonstrated disappearing of short living component after 24 hours. Long living component had same lifetime as intact TagRFP. That means that there is no FRET in recombinant protein after 24 h and sensor is fully cleaved.

References

1. A. Page-McCaw,et al, *Nature Reviews | Molecular Cell Biology*, 2007, **8**, 221-233.
2. J. Yang, Z. Zhang, J. J. Lin,Lu, Q. Luo, *Biochim Biophys Acta* ,2007, **1773**(3), 400-407.
3. S. Netzel-Arnett, *Biochem.*, 1993, **32**(25), 6427-6432.
4. A. Rusanov, T. Ivashina,L. Vinokurov, et al., *Journal of biophotonics*, 2010, **3**(12), 774-83.

Invited

OPTICAL IMAGING IN MAMMALIAN EMBRYOLOGY

K.V. Larin

University of Houston, Houston, USA, klarin@uh.edu

Many aspects of human embryonic development remain unknown because currently available imaging methods are insufficient to visualize the fetus with sufficient resolution in the first few weeks of pregnancy. Mouse model provides a great system for studying mammalian development since its developmental processes are similar to humans and because of the wealth of available methods to manipulate the genome and create mutant animals. Many mutant mouse lines with various developmental defects linked to human diseases are developed are being identified regularly using single gene targeting approaches and large scale screens creating a pressing need for imaging techniques allowing to study functional effects of the genetic manipulations on embryonic development. Toward this goal, non-invasive methods such as ultrasound, Micro-MRI and microcomputed tomography (MicroCT) have been employed [1–4].

Because ultrasound waves can penetrate through many centimeters of tissue without significant attenuation, this method has proven to be valuable noninvasive embryo phenotyping tool [1, 2]. However, the resolution of this technique even for high frequency systems is limited to about 30-100 μm. Micro-MRI is used for structural 3D embryo imaging, but its resolution is also limited to about 25–100 μm [5]. Additionally, due to the long acquisition times, MRI is sensitive to motion and has limited applicability in live embryo imaging [5–7]. Microcomputed tomography allows for high-resolution (2–50 μm) 3D imaging, but it relies on the administration of contrast agents, and the acquisition time required for the method is also too long to be applicable for dynamic imaging [4]. Thus, these currently available non-invasive methods either suffer from poor resolution or long acquisition times, which limit their use for live imaging of embryos *in utero*.

Optical techniques, using visible and near-infrared light, can achieve higher spatial resolution with short acquisition times, but scattering and absorption reduce the imaging depth. Since mammalian embryos develop *in utero*, dense maternal tissue restricts light penetration to the embryos, making optical imaging very challenging. Early stage post-implantation embryos, prior to the dependence on the maternal-placental connection (5.5–10.5 days post-coitus (dpc)), can be cultured and imaged directly using optical microscopy methods such as confocal or multiphoton microscopy [8–10]. While sub-micron spatial resolution can be achieved with these methods, the imaging depth is limited to hundreds microns (3-600um) making this method more applicable to early embryos and superficial structures.

To circumvent limits to depth penetration with fluorescence imaging methods while retaining sub-cellular spatial resolution, we have turned to the use of Optical Coherence Tomography (OCT). Optical Coherence Tomography (OCT) is a 3D imaging technology based on analysis of interferometry between light backscattered from a sample and a reference signal. This relatively novel modality is increasingly gaining popularity among researchers in ophthalmology, cardiology, dermatology and oncology. OCT uses non-ionizing radiation and is considered to be safe, as OCT is FDA approved for use in humans and is currently employed in nearly every ophthalmology clinic [11]. The format of data acquired with OCT is similar to that of ultrasound, but the resolution of OCT is about 2 to 10 μm (which is an order of magnitude higher than with high-frequency ultrasound or Micro-MRI), while the imaging depth in tissue is about 1 to 3 mm. We have recently shown that OCT can be used for live visualization of the entire externalized cultured mouse embryos (Fig. 1) until 10.5 dpc with a spatial resolution of 8 μm [12, 13]. This resolution is sufficient to image individual circulating blood cells and small groups of cells, as well as the movement of the heart wall and blood vessels [14]. However, embryos grown in cultured can

Fig. 1. Live imaging of cultured 9.5 dpc mouse embryo with OCT

only be maintained for 24–48 hours and embryos beyond 10.5 dpc will not survive due to the need for maternal support. This method therefore excludes the possibility of following long-term processes in the same embryo.

To fill this gap, we are developing a new methodology for live imaging of mouse embryos *in utero* beginning at 12.5 dpc through the remainder of embryogenesis [15]. This methodology involves externalization of the uterine horn through an abdominal incision for imaging. Although semi-invasive, this method allows us to repeatedly image the same living embryos to characterize temporal changes in organ development at previously unprecedented spatial resolution.

Potentially this method can enable high-throughput screens directed at recovering specific phenotypes in embryos and would even further enhance our understanding of genetic complexity of early mammalian development and congenital birth defects.

Acknowledgements

The author acknowledges financial support from the National Institutes of Health (R01HL095586) and the American Heart Association (10SDG3830006).

References

1. F.S. Foster, M. Zhang, A.S. Duckett, V. Cucevic, and C.J. Pavlin, "*In vivo* imaging of embryonic development in the mouse eye by ultrasound biomicroscopy", *Invest Ophthalmol Vis. Sci*., 2003, **44**, 2361-2366.
2. C.K.L. Phoon, D.H. Turnbull, "Ultrasound biomicroscopy-Doppler in mouse cardiovascular development", *Physiol Genomics*, 2003, **14**, 3-15.
3. F.S. Christopher, W.L. Cecilia, and L. Linda, "Fetal Mouse Imaging Using Echocardiography: A Review of Current Technology", *Echocardiography*, 2006, **23**, 891-899.
4. E.L. Ritman, "Micro-computed tomography-current status and developments", *Annu Rev Biomed Eng*., 2004, **6**, 185-208.
5. B. Hogers, D. Gross, V. Lehmann, K. Zick, H.J. De Groot, et al., "Magnetic resonance microscopy of mouse embryos in utero", *Anat Rec*., 2000, **260**, 373-377.
6. P. Pallares, M.E. Fernandez-Valle, and A. Gonzalez-Bulnes, "*In vivo* virtual histology of mouse embryogenesis by ultrasound biomicroscopy and magnetic resonance imaging", *Reproduction, Fertility and Development*, 2009, **21**, 283-292.
7. B.J. Nieman, N.A. Bock, J. Bishop, X.J. Chen, J.G. Sled, et al., "Magnetic resonance imaging for detection and analysis of mouse phenotypes", *NMR Biomed*., 2005, **18**, 447-468.
8. E.A.V. Jones, D. Crotty, P.M. Kulesa, C.W. Waters, M.H. Baron, et al., "Dynamic *in vivo* imaging of postimplantation mammalian embryos using whole embryo culture", *Genesis*, 2002, **34**, 228-235.
9. J.L. Lucitti, E.A.V. Jones, C. Huang, J. Chen, S.E. Fraser, et al., "Vascular remodeling of the mouse yolk sac requires hemodynamic force", *Development*, 2007, **134**, 3317-3326.
10. S. Nowotschin, A.K. Hadjantonakis, "Use of KikGR a photoconvertible green-to-red fluorescent protein for cell labeling and lineage analysis in ES cells and mouse embryos", *BMC Dev Biol*., 2009, **9**, 49.
11. J Chen, L Lee, "Clinical applications and new developments of optical coherence tomography: an evidence-based review", *Clin. Exp. Optom*., 2007, **90**, 317-335.
12. I.V. Larina, N. Sudheendran, M. Ghosn, J. Jiang, A. Cable, et al., "Live imaging of blood flow in mammalian embryos using Doppler swept source optical coherence tomography", *Journal of Biomedical Optics*, 2008, **13**, 0605061-0605063.
13. K.V. Larin, I.V. Larina, M. Liebling, and M.E. Dickinson, "Live Imaging of Early Developmental Processes in Mammalian Embryos with Optical Coherence Tomography", *Journal of Innovative Optical Health Sciences*, 2009, **2**, 253-259.
14. I.V. Larina, S. Ivers, S. Syed, M.E. Dickinson, and K.V. Larin, "Hemodynamic measurements from individual blood cells in early mammalian embryos with Doppler swept source OCT", *Optics Letters*, 2009, **34**, 986-988.
15. S.H. Syed, K.V. Larin, M.E. Dickinson, and I.V. Larina, "Optical coherence tomography for high-resolution imaging of mouse development in utero", *J. Biomed. Opt*., 2011, **16**, 046004.

LIVE IN UTERO EMBRYONIC IMAGING WITH OCT

I.V. Larina[1], **S. Syed**[2], **K.V. Larin**[1,2], and **M.E. Dickinson**[2]

[1] Baylor College of Medicine, Houston, USA, larina@bcm.tmc.edu
[2] University of Houston, Houston, USA

The mouse is a superior mammalian model to study early embryonic development. Hundreds of mouse mutants mimicking human birth defects and diseases have been generated to advance our understanding of the genetic basis of development and disease. However, high-resolution live dynamic visualization of mouse embryos remains a technical challenge. We are developing a new methodology for live imaging of mouse embryos *in utero* beginning at E12.5 through the remainder of embryogenesis. We assessed the capability of the proposed methodology to visualize structures of the living embryo from embryonic stages E12.5 to E18.5. Repetitive *in utero* embryonic imaging with single-cell resolution is demonstrated. This work opens the door for a wide range of live embryonic studies to understand congenital defects and effects of pharmacological and toxicological agents on embryonic development.

Introduction

About 6% of infants worldwide are born with serious birth defects. Moreover, birth defects are the leading cause of infant deaths. There are thousands of different birth defects, affecting the structure or function of every part of the human body. Currently, about 70% of the causes of birth defects are unknown. The mouse is a classic mammalian model used to study the anatomical and physiological development of different organ systems. Hundreds of mouse mutants associated with human diseases have been reported, helping to advance our understanding of the genetic basis of development and disease [1–3]. However, the success of these efforts relies heavily on the ability to analyze phenotypic outcomes, raising an urgent need for better phenotyping tools.

Traditionally, the primary analysis of embryonic mutant phenotypes have been based on static analysis of histological sections, requiring many litters at different time points to deduce phenotypic changes. However, methods that allow for directly assessing embryonic phenotypes in utero would obviate the need for sectioning multiple litters, would provide dynamic information about development and would enable higher throughput analysis for use in large-scale screens. Currently available non-invasive methods either suffer from poor resolution or long acquisition times, which limit their use for live imaging of embryos in utero.

We are developing a methodology for chronic *in utero* imaging of mouse embryos with Optical Coherence Tomography (OCT), which involves externalization of the uterine horn through an abdominal incision for imaging [4]. Although semi-invasive, this method allows us to repeatedly image the same living embryos from E12.5 to E18.5 to characterize temporal changes in organ development at previously unprecedented spatial resolution.

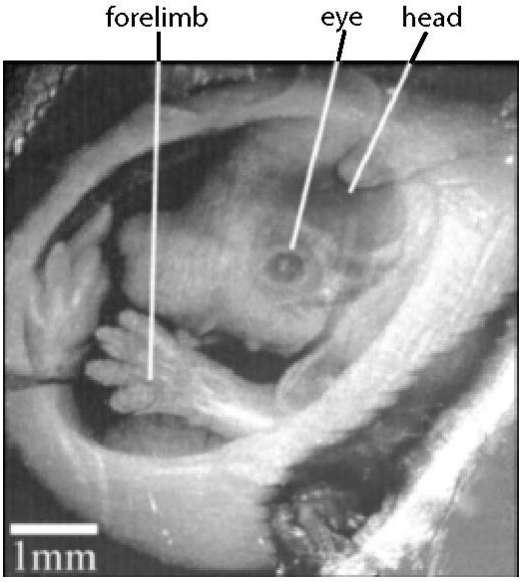

Fig. 1. 3D reconstructions of live 15.5 day mouse embryo acquired with OCT through the uterine wall

Materials and Methods

A Swept-Source OCT (SS-OCT) system used in this study employs a broadband swept-source laser (Thorlabs, SL1325-P16) with output power P = 12 mW, central wavelength $\lambda_0 = 1325$ nm, and spectral width $\Delta\lambda = 100$. The scanning rate over the full operating wavelength range is 16 kHz, resulting in the A-scan (in-depth profile) acquisition rate of 16 kHz. The imaging system is described in more details in [5]. The resolution of the current imaging system was measured to be 8 μm in both lateral and in-depth directions.

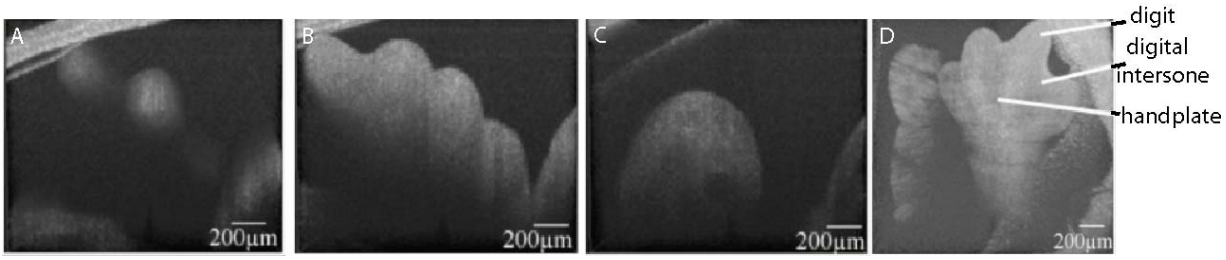

Fig. 2. Structural OCT imaging of the embryonic limb at E13.5 *in utero*

All animal manipulation procedures described here were approved by the Animal Care and Use Committee. Timed matings in CD-1 mice were set overnight and a presence of a plug in the morning was counted as E0.5. For repetitive imaging of developing embryos, the first imaging session was performed at E13.5 and then repeated at E15.5 and E17.5. The pregnant females were anesthetized with isoflurane by inhalation. The mouse was placed on a heated platform to maintain the body temperature at 37^{o}C during the whole procedure. Abdominal fur was removed with an electric clipper. To optimize visualization of each embryo and accurately identify individual embryos, the gravid uterine horn was externalized through a 1-2 cm incision made in the lower abdomen. To ensure repetitive imaging of the same embryos, each embryo was assigned a number according to its position in the uterus. After the imaging, the incision was closed using surgical sutures. To minimize post-operative discomfort, Carprofen (5 mg/kg) was administered to the females every 24 hours. There were up to three imaging sessions for each pregnant female and each mouse was sacrificed immediately after the third session.

Results and Discussion

Figure 1 shows an example of 3-D reconstructions of mouse embryo in the uterus at the embryonic stage E15.5. The data set for the reconstruction was acquired as a series of 512 x 512 A-scans over a 10mm x 10mm x 2.2 mm volume. For visualization purposes, the top layers corresponding to the uterine wall and the yolk sac were removed from the reconstruction with a clipping plane. The head and the forelimb are distinguishable on he reconstruction. Craniofacial details are clearly outlined. An example of embryonic limb imaging is shown in Figure 2. Panels (A-C) are in depth OCT scans through the E13.5 embryonic limb in utero. Corresponding 3-D reconstruction of the limb is shown in Figure 2D.

These observations suggest that the proposed technique can be useful to follow the development of different mouse embryonic organs *in utero* and can potentially be used as phenotyping tool needed to screen for mutations and toxins that disrupt normal development.

Acknowledgements

The project is supported by the National Institutes of Health (R01HL095586) and the American Heart Association (10SDG3830006).

References

1. S.D. Brown, W. Wurst, R. Kuhn, J.M. Hancock, "The functional annotation of mammalian genomes: the challenge of phenotyping", *Annu Rev. Genet*., 2009, **43**, 305-333.
2. I.Y. Kim, J.H. Shin, J.K. Seong, "Mouse phenogenomics, toolbox for functional annotation of human genome", *BMB Rep*., 2010, **43**, 79-90.
3. H Morgan, T Beck, A Blake, H Gates, N Adams, et al., "EuroPhenome: a repository for high-throughput mouse phenotyping data", *Nucleic Acids Res*., 2010, **38**, D577-585.
4. S.H. Syed, K.V. Larin, M.E. Dickinson, and I.V. Larina, "Optical coherence tomography for high-resolution imaging of mouse development in utero", *J. Biomed. Opt*., 2011, **16**, 046004.
5. I.V. Larina, N. Sudheendran, M. Ghosn, J. Jiang, A. Cable, et al., "Live imaging of blood flow in mammalian embryos using Doppler swept source optical coherence tomography", *Journal of Biomedical Optics*, 2008, **13**, 0605061-0605063.

SPECTRA ANALYSIS AND RECOGNITION ALGORITHMS FOR THE OPTICAL BIOPSY STUDIES OF BREAST TUMORS

S.A. Belkov[1], **G.G. Kochemasov**[1], **T.E. Lyubynskaya**[1], **N.V. Maslov**[1], **A.S. Nuzhny**[2], **L.B. Da Silva**[3], and **A. Rubenchik**[4]

[1] Russian Federal Nuclear Center-VNIIEF, 37 Prospekt Mira, Sarov, Nizhny Novgorod reg., 607200, Russia
e-mail: tlyubyn@gmail.com
[2] Nuclear Safety Institute of Russian Academy of Science, 52 Bolshaya Tulskaya, Moscow, 115191, Russia
[3] BioTelligent Inc., 6248 Preston Ave., Livermore, CA 94551, USA
[4] LLNL, 7000 East Ave., Livermore, CA 94551, USA

Introduction

In recent years optical biopsy methods proved to be an effective tool for cancer diagnostics, prognostics and treatment management. These methods have advantages of minimal invasiveness, on-line analysis, low cost, ease of implementation and do not require high-skilled pathologists for data interpretation. Fluorescence, Raman and elastic scattering signals are commonly used in oncology studies [1].

In the works [2-4] diagnostic ability of optical scattering and absorption spectra was demonstrated. The shapes of spectral curves have specific absorption bands deforming when the disease progresses, and that allows tissue differentiation on types and conditions. Application of a contact probe for surface cancer diagnostics was presented in [5, 6].

The minimally invasive probe and the diagnostic system reported here are also based on optical radiation spectra recording and analysis and seem to be a promising tool for early diagnostics of breast cancer [7]. In this system spectra are generated continuously as far as the needle-like probe containing one emitting and several collecting optical fibers penetrates through the tissues moving to the suspicious area. That allows analyzing not only the state of the local site, but also the structure of healthy tissues and tumors.

The study was conducted by a joint Russian-American team. The American partners were Biotilligent Inc. and Lawrence Livermore National Laboratory. The Russian participants were Biofil, Russian Federal Nuclear Centre – VNIIEF, Institute of Applied Physics RAS, Nizhny Novgorod Oncology Centre, and Nizhny Novgorod State Medical Academy.

Technical details

The system consists of a source of white light (Xe lamp with continuous spectrum in the range of 370-750 nm), a measurement circuit and a unique probe with disposable needles incorporating optical fibers. It is supplied with a computer for operation control and data recording.

The needle diameter is 0.8 mm and the length is 50 mm, fiber diameter is 100 μm. One of the fibers inside the needle emits white light which interacts with biological tissue and is then collected by three other fibers located at different distances (several hundred microns) from the source. To control the depth of needle penetration and determine mechanical parameters of biological tissues the optical probe was provided with position and force sensors.

The measurement circuit is composed of three S2000 fiber optic spectrometers (*Ocean Optics Inc*., USA) with the range from 200 to 1100 nm and resolution ~1.76 nm.

Each PC record contains the data of a microscopic volume of tissue. Macroscopic information about tissue optical properties is obtained by continuous data acquisition during the whole period of probe movement. The recording frequency of 100-120 Hz enables spectral measurements each 100 μm along the trajectory of needle movement at the recommended rate of 1 cm/sec.

Data acquisition and processing

To perform clinical studies a test protocol was developed and approved by the Ethical Committee of Nizhny Novgorod State Medical Academy of the Ministry of Health of the Russian Federation on scientific study with human participation as a subject of investigation. In the Nizhny Novgorod Regional Oncology Centre a treatment room was equipped and 165 tests were completed. Each procedure was supported by video filming and audio recording of the comments of the physician delivering the procedure. Independent medical diagnoses were the results of fine-needle biopsy and histology.

Not all the records are reliable enough and may be used for the diagnostic purposes. Visual examination discovered that the spectra of skin were close to those of the malignant tissues. So we did not take into consideration the data obtained from the depth less that 3 mm. The data acquired on the back movement were excluded too, because the channel was filled with blood, which distorted real tissue spectra. The position sensor data were used for primary filtration.

A large amount of recorded data (up to tens of thousands per patient) need automatic processing. Two approaches were used: traditional statistical analysis and neural networks. Both of them had wavelet expansion as a preprocessing stage [8]. Wavelet expansion is widely used for signal processing and filtering, because it permits to get rid off noise and various artifacts in the data such as random surges, gaps, nonlinear distortions, etc. Haar wavelet family was used in the present study as the most saving for calculation resources.

Unfortunately, some cases were totally rejected because of either technical or performance reasons. About 130 tests were considered trustworthy enough and made the base for spectral type definition. Clusterization technique revealed several main spectral shapes for malignant (4) and benign (3) tumors. Based on that automatic algorithm was developed and end-to-end analysis for the majority of the cases was completed. Comparison of the results with medical diagnoses obtained from cytology and histology investigation gave the index of sensitivity equal to 90% and specificity equal to 91%.

Neural network algorithm was developed as a prototype of future on-line processing tool. The principles of learning theory [9] require composing a learning sample, which is a set of spectrum examples presenting different tissue types. The learning sample was formed based on physicians' comments going with the procedure and only the most reliable in performance data were included.

To build a model for data division an approximation problem was considered. The goal was to reconstruct the data generation rules, given a finite amount of known data. It is the inverse problem and as the majority of them it is ill-posed, i.e. has a set of solutions. Such uncertainty may be eliminated by regularization – restriction of the set of possible solutions. In our study the Bayesian regularization method was used [10].

The model based on three-layer perceptron was tested over the sample of 29 'cancer' and 29 'non-cancer' cases and demonstrated total separation. Although we expect that the sensitivity and specificity may deteriorate with testing sample increase (because of imperfectly performed cases), we believe that the developed model has strong potential to generalize a great variety of data and its accuracy may eventually become comparable with that of the most advanced methods of breast cancer diagnostics.

Conclusion

The optical biopsy system underwent first clinical tests. Automatic statistical data processing and analysis algorithm was developed and the indexes of sensitivity and specificity were estimated on the basis of medical diagnoses: 90% and 91% correspondingly. The method of artificial neural networks was also applied for data analysis as a prototype of further on-line diagnostic algorithm and total separation on the limited data set was demonstrated.

Acknowledgements

This work was supported by funding from GIPP (Global Initiatives for Proliferation Prevention) Program of the US Department of Energy under contract LLNL-T2-0242-RU and Project #3075p of the International Science and Technology Center.

References

1. I.J. Bigio, S.G. Bown, *Cancer Biology and Therapy*, 2004, **3** (3), 259.
2. J.R. Mourant, J. Boyer, A. Hielscher, I.J. Bigio, *Opt. Lett*., 1996, **21**, 546.
3. L.T. Perelman, V. Backman, M. Wallace, et al., *Phys. Rev. Lett*., 1998, **80**, 627.
4. J.R. Mourant, M. Canpolat, C. Brocker, et al., *J. of Biomedical Opt*., 2000, **5**, 131.
5. I.J. Bigio, S.G. Bown, G. Briggs, et al., *J. of Biomedical Optics,* 2000, **5**, 221.
6. G. Zonios, L.T. Perelman, V. Backman, et al., Applied Optics, 1999, **38**, 6628.
7. S.A. Belkov, G.G. Kochemasov, S.M. Kulikov, et al., Proceedings of SPIE, 2008, **6859**, 20.
8. I. Daubechies, *Ten Lectures on Wavelets*, SIAM, USA, 1992.
9. A. Tikhonov, V. Arsenin, *Solutions of ill-posed problems* (W.H.Winston, Washington, DC 1977).
10. P. Williams, *Neural Computation*, 1995, **7**, 117.

DEFINITION OF SELENIUM CONCENTRATION CHANGE IN BLOOD AFTER APPLICATION OF SELENIUM PREPARATIONS BY FLUOROMETRIC TECHNIQUE

V.V. Anipko[1], V.S. Maryakhina[2], and L.L. Abramova[1]

[1] Orenburg State Agriculture University, Orenburg, Russia, anipko86@rambler.ru
[2] Orenburg State University, Orenburg, Russia. valemar@mail.ru

Abstract

The influence of selenium preparations on the selenium concentration in rabbit's blood is considered. It is shown that the "Selenolin" preparation is more efficient than "E-Selen", because it is better assimilated in animals' organisms. The selenium concentration in the blood of rabbit females was measured by a fluorometric technique. Data processing was based on decomposition of spectra into Gaussian-Lorentzian components. We found that selenium concentration in blood increases 3÷5 times compared with the control group after application of selenium preparations. It was also revealed that application of "Selenolin" leads to increased quantity of lactocytes. These results can be used to remove selenium deficiency of rabbits and for prevention of diseases.

Summary

Selenium is a trace element the content of which in the organism depends on physiological state. Selenium deficiency can lead to dysfunction of any organ, including reproductive ones. Known, Preparations on the basis of selenium compounds are known to have a prolonged effect. Large doses of selenium preparations are toxic for people and animals. Thus, control of their content in the organism is important.

The purpose of this study was analyzing the influence of preparations on selenium concentration in rabbits' blood, and dev eloping an alternative method of assessing selenium concentration in blood.

The object of research was blood from rabbit females of the Soviet Chinchilla breed. Three animal groups were formed: control group and two experimental groups. Every group consisted of five animals. The "E-Selen" preparation was injected into females of the first experimental group with the dose 0.04 mg/kg (weight). The "Selenolin" preparation was injected into females of the second experimental group with the dose 0.01 mg/kg (weight). Ten days after the injection we made blood sampling. The "E-Selen" is water-dispersed complex of vitamin E with sodium selenide. The "Selenolin" is a therapeutic and preventive medication created on the base of selenium-organic compound. These preparations were used as they had been successfully tried on other animal breeds.

The samples were centrifuged for separation of blood cells. The HCl solution was added to the obtained blood serum. The mixture was gradually heated up to 60ºC for transformation of Se (VI) to Se (IV). After that, the Diaminonaphthalene (DAN), EDTA, and HCl were added to pre-cooled mixture and then heated by 80 ^{0}C for 20 minutes and extracted with the cyclohexane at 36-37ºC. Fluorescence spectra of the solution (complex of selenium with DAN) were measured on a SOLAR CMM-2203 device in cyclohexane phase, because it is fluoresced in nonpolar solvents only. The excitation wavelength was 363 nm, maximum of absorption spectrum of selenium with DAN complex (SDAC) located in this region.

For data proceedings, a few standard solutions were prepared. An aliquot of selenium acid (H_2SeO_3) with concentration 7.75 10^{-3} M was taken instead of blood serum. The aliquot was from 5 to 30 µl. The selenium concentration in the blood was defined by calibration plot generated on the basis of measurements of standard solutions.

We used the method based on the well-known reaction between Se (IV) and DAN depicted in (1).

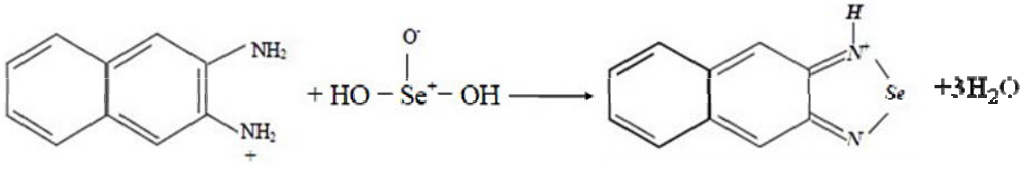

(1)

The fluorescence spectra of solutions have two maxima: 515 and 560 nm. The first maximum (515 nm) is characterized by SDAC fluorescence. The second maximum (560 nm) is characterized by fluorescence of unreacted DAN. The maxima ratio in the fluorescence spectra depends on Se (IV) amount in the probe. The increase of Se (IV) quantities leads to the increase of the first fluorescence maximum (fig. 1).

The obtained fluorescence spectra of standard solutions were decomposed into Gauss-Lorentz components, and an area under every curve was assessed. After that, a calibrating plot was constructed as a function of selenium concentration obtained on the basis of the calculated areas under the curves from known selenium concentration of standard solutions. The concentration of selenium in the samples was determined from the calibrating plot. This data proceeding improved the quality of the test, and led to separate fluorescence of every component, decreasing the influence of scattering light and mixtures.

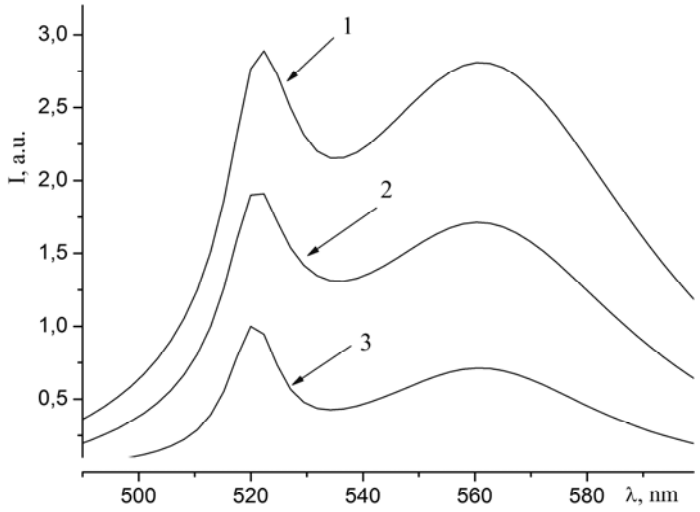

Fig. 1. Spectra fluorescence of standard solutions with Se concentrations:
1 – 1.05 μM; 2 – 2.1 μM; 3 – 4.2 μM

We found that "Selenolin" is a more effective preparation than "E-Selen". Selenium concentration in blood increases 3÷5 times compared to the control group after application of all selenium preparations. Their values are 1.16 ± 0.25 μM, 3.38 ± 0.84 μM and 5.66 ± 1.18 μM for the control group, the first experimental and second experimental rabbits groups, respectively.

In addition to the concentration effect, the biological effect of application of the studied preparations should be mentioned. The cytological studies showed that application of "Selenolin" leads to increased quantity of lactocytes. As a consequence, the quantity of milk in rabbit females rises compared with the control group. The effect was less pronounced in females of the first experimental group than in the other groups of animals.

Hence, selenium preparations are assimilated in animal organisms, increasing selenium concentration in rabbits' blood. The "Selenolin" preparation is more effective than "E-Selen". The results of the research may be used for prevention of animal diseases.

Acknowledgements

This work was supported by the Foundation for Promotion of the Development of Small Business in Science and Technology (contract № 14 from 01.02.2010).

OPTICAL DIAGNOSTICS OF BIOTISSUE CELLS CULTIVATED IN POLYMER MEDIA

V.S. Maryakhina and **S.N. Letuta**

Orenburg State University, Orenburg, Russia, valemar@mail.ru

Abstract

Features of delayed fluorescence of molecular probes in normal and cancer cells have been studied by the laser photolysis technique. The cells were cultivated in a polymer nutrient medium. For this "Hyamatrix" has been proposed as a nutrient medium for cultivation of bacteria and somatic cells. It was created on the basis of the polymer of native form of hyaluronic acid. For spectral and kinetic measurements xanthene dyes are used as molecular probes. Differences of oxygen concentration in cells are calculated by the measurements data of their delayed fluorescence kinetics. The influence of bacterial pollution of cell culture on optical measurements was also analysed. Results of the studies aimed at developing an alternative diagnostics method of biotissues are considered.

Introduction

Optical techniques are frequently used in different fields of biology and medicine for development of alternative diagnostic methods of biological structures. The state of biotissues or cells is estimated by intensity of light scattering and fluorescence spectrum of endogenous and exogenous fluorophores. The basic problem of the investigations is insufficient accuracy of experimental data. Registration of triplet states of dye is capable of enhancing accuracy of the evidence.

Living cells must be at hand to develop optical biomedical diagnostics. Special nutrient media are needed for this. A possibility of cultivating any cell types on the surface of "Hyamatrix" was demonstrated and spectral luminescence properties of exogenous fluorophores in cells were studied.

The subject and methods of research

The objects of research were fibroblasts, E. Coli bacteria, as well as cells were obtained from normal and cancer mammary gland of female mice (BYRB line with spontaneous cancer tumor). Fragments of mammary gland tissue were taken into collagenase solution (0.5 mg/ml) in a phosphate buffer (pH = 7.4) and were incubated at 37^0C.

After fermentation dissociation of the obtained mammary cell suspention was placed into the nutrient medium and incubated for 24 hours at 37^0C and atmospheric pressure. The nutrient medium (biomaterial "Hyamatrix") was created by Rakhmatullin R. [1] in the form of a polymer plate (biopolymer) obtained in the process of hydrogel polymerization in basic hyaluronic acid. The plate thickness was 0.25 mm, density 340.13 kg/m^3. The properties of the biomaterial were described in detail in [2].

Oxygen penetration of biomaterial and cells was studied using the delayed fluorescence (DF) technique. Xanthene dyes (erythrosine, bengal rose and eosine) were used as molecular probes for spectral measurements. The setup for studying DF kinetics of dye molecules was based on YAG:Nd laser. Molecules were excited by second harmonic of the laser (λ_{ex} = 532 nm). The pulse duration was 10 ns, energy 10–50 mJ. The influence of bacterial pollution on results of DF measurement was studied. For this E. coli were cultivated on the surface of the biomaterial for 24 hours. The vitality of bacteria and somatic cells was controlled by standard microbiological methods. After that, DF kinetics and fluorescence spectra of dyes in biomaterial as well as biomaterial with E. coli were measured. The excitation wavelength during measurements of fluorescence spectra was 520 nm.

Results

Results of the experiments demonstrate that somatic cells and bacteria are effectively cultivated on the surface of biomaterial. The cultivated cells are located on biomaterial surface forming a monolayer. The thickness of the polymer plate is decreasing during cultivation. Biodegradation of the polymer plate is the result of biomaterial assimilation. Biopolymer swells without cells, but it doesn't dissolve. The ability of cell cultivation on the surface of biomaterial is explained by the features of the biomaterial structure and bioorganic compounds included in it [2]. The biomaterial has a fiber

structure which is identical to biotissues. Microstructure of the biomaterial was investigated by the AFM technique. It consists of polymer fibers of hyaluronic acid with thickness of about 100 nm.

Fibroblasts were cultivated on the biomaterial surface for testing biocompatibility. The experimental results show that these cells are also cultivated on the biomaterial surface with fission period of 24 hours.

The air pressure change above the polymer plate without cells from 150 torr to the atmospheric pressure doesn't influence the DF dyes kinetic. Hence, a very small part of oxygen penetrates into nutrient medium. Quite another character of DF function is observed at exogenous fluorophores luminescence in cells obtained from biotissues. The cells located on the nutrient medium surface contain oxygen that easily diffuses in liquid medium. Triplet states are extinguished with molecular oxygen. As a result, singlet oxygen is generated $^1\Delta_g(O_2)$. The annihilation unextighuished triplet state of the dye with the oxygen molecules generates dye S1 states. Thus, the DF kinetic is registered as a sum of two processes different in nature, containing information about the medium state. Therefore, DF kinetics of cells has a hump-shaped type [3]. The experimental results are shown that the culture of normal mammary cells has high sensitivity to oxygen. These differences in the experimental data will occur if we have living cells only. The authors found that stationary concentration of molecular oxygen and its lifetime in normal cells is higher than in cancer cells.

The influence of the stage of cancer development on results of spectral measurements was investigated. Cancer cells were taken from spontaneous mice tumor with diameter 1÷3.5 cm. The dependence between accumulations of triplet states of dyes in two cell types is shown. In the case of normal cells the maximum of DF accumulation is shifted toward shorter times at 3 ± 1 μs, which indicates an increase of oxygen concentration in it. With development of the pathological process the influence of the cancer cells enhances.

Fluorescence spectra of samples with mammary and bacterial cells cultivated on the biomaterial surface are measured. They will be extinguished if samples contain E. coli bacteria. This dependence is also shown for samples containing mammary cells. DF kinetics of dyes in mammary cells and bacteria has an identical type. Thus, bacterial pollution can negatively influence results of spectral and kinetic measurements.

Conclusion

Hence, in this work a possibility of using biomaterial as a nutrient medium for cell cultivation was demonstrated. Somatic cells and bacteria are effectively cultivated on the surface of biomaterial. The results of DF kinetics can be used either for a design of alternative diagnostics method of biotissues or for control of cells viability. High sensitivity of the method allows finding pathological changes in cells at early stages.

Acknowledgements

This work was supported by a grant from the Russian Foundation for Basic Research (RFBR) (Grant № 09-02-99020) and Foundation for Promotion of the Development of Small Business in Science and Technology (contract № 14 of 01.02.2010).

References

1. R.R. Rakhmatullin, D.A. Pozdnyakov, *Patent* № 200811069 from 21.03.2008 [RU].
2. S.N. Letuta, V.S. Maryakhina, R.R. Rakhmatullin, *Quantum-electronics*, 2011, **41**(4), 314–317.
3. S.N. Letuta, V.S. Maryakhina, *Proc. SPIE*, 2011, **7999**, 26-30.

DEVELOPMENT OF A TECHNIQUE OF SCREENING OF AGENTS FOR PHOTODYNAMIC THERAPY OF CANCER *IN VIVO* USING COLOR FLUORESCENT PROTEINS

I.G. Meerovich[1], **V.V. Zherdeva**[1], **N.I. Kazachkina**[1], and **A.P. Savitsky**[1]

[1] A.N.Bach Institute of Biochemistry of RAS, Moscow, Russia, imeerovich@inbi.ras.ru

Introduction

Fluorescent diagnostics (FD) and photodynamic therapy (PDT) are the promising methods of diagnostics and treatment of oncological diseases, based on the application of photosensitizers (PS), selectively accumulate in tumors and rendering of the antitumor effect of the irradiation of light a certain wavelength.

The efficiency of photodynamic damage to biological tissue is determined mainly by the level of accumulation of PS, its localization in tissues and photochemical activity. One of the problems of PDT is to increase the selectivity of FS in the tumor. To reduce the side effects caused by the accumulation of PS in a number of healthy organs and tissues (liver, spleen, kidneys, as well as in the skin), it is necessary to study the dynamics of the level of accumulation of PS in tumor and normal tissue, for each PS to determine the best time for the photodynamic therapy. This can be performed using different methods, including non-invasive, for example, the spectral fluorescence spectroscopy, diffuse reflection, etc.

Our work was devoted to improving the screening of new agents for the fluorescent visualization and photodynamic therapy (PDT) of cancer using red fluorescent tumor models and photosensitizers (PS) with fluorescence in near-infrared (rear IR) spectral range, possessing the biggest efficient depth of photodynamic action.

Materials and Methods

To obtain fluorescent xenograft tumor model the of mel Kor-TurboRFP cell line [1] was used. Cells ($10x10^6$ in 150 μL) were inoculated subcutaneous into back of BalbC/*nude* mice.

Tumor growth and inhibition was estimated by palpation as well by different fluorescence methods, such as fluorescent imaging by fluorescence small animal imaging system UVP iBox (UVP, LLS, USA) and diffuse fluorescent tomograph DFT-3 (Institute of Applied Physics, Russia).

Processing of the fluorescence images was performed using the program Images J 1.42q (NIH, USA).

Results and Discussion

To select the optimal time for the exposure sensitized tumors was studied by means of fluorescent methods pharmacokinetics IR-photosensitizers in an organism of the mouse.

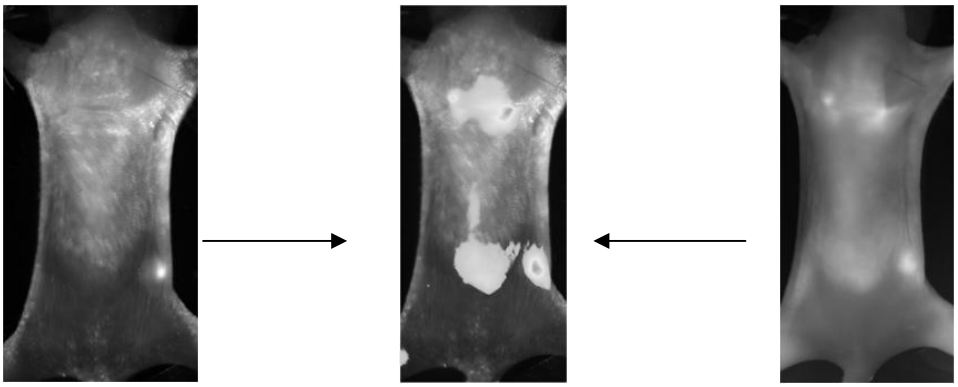

Fluorescent tumor localization exitation filter 502–547 нм emission filter 570–640 nm

Colocalization

Photosensitizer localization Exitation filter 600–645 nm emission filter > 700 nm

Fig. 1. Fluorescent images of mouse with fluorescent tumor 24 hours after i.v. injection liposomal photosensibilizator "Tiosens" (6 mg/kg of bodyweight).
Image of colocalization of fluorescence of PS and fluorescent tumor was received by iBox software

The distribution of infrared PS *in vivo* in animals at various ways of injection of PS was studied using UVP iBox. Example of images after use of liposomal preparation of phthalocyanine derivative "Tiosens" are presented on Fig. 1, and digital processing of data received is presented on Fig. 2.

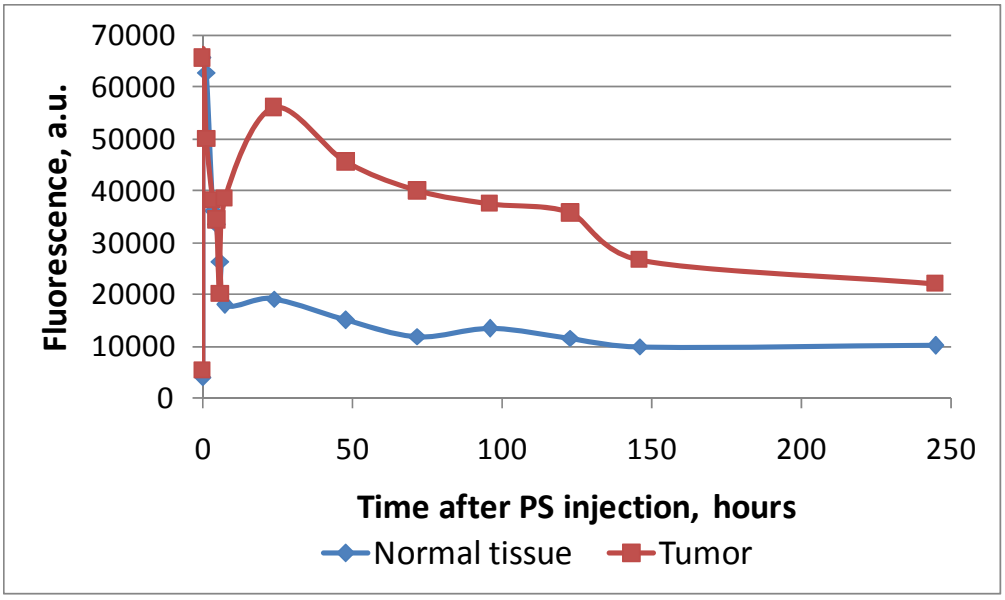

Fig. 2. Uptake of "Tiosense" by tumor and normal tissue after i.v. injection at dose of 6 mg/kg bodyweight

It was shown that the accumulation of liposomal "Tiosens" in the tumor reaches a maximum 24 hours after intravenous injection of PS, at this moment this is achieved contrast accumulation equal to 3, in the future contrast even a little increased, but at the same time is reduced accumulation of FS in the tumor.

Irradion of tumors was performed by 730 nm laser (Biospec, Russia) at power density of 260 W/cm^2 for 20 min. The time to start irradiation was chosen as 24 hours after PS administration, based on time ranges of maxima of PS accumulation in tumor and ratio of PS uptake by tumor in comparison to normal tissue and organs.

Efficiency of photodynamic treatment was evaluated by change of tumor size, which was determined by direct measurement of tumor boundaries by palpation as well as by analyzing fluorescent images of the tumor made using the diffuse fluorescent tomography.

Decreasing of tumor volume of fluorescent tumor, sensitized by liposomal "Tiosens", was shown by means of diffuse fluorescence tomography.

Acknowledgements

The work was supported by grant of Program of Presidium of Russian Academy of Sciences "Fundamental sciences for medicine".

References

1. I.G. Meerovich, L.R. Arslanbaeva, M.M. Shigreva, D.V. Sokolova, O.S. Burova, N.V. Andronova, E.M Treshalina., A.Yu. Baryshnikov, and A.P. Savitsky, *Proc. II International symposium Topical problems of biophotonics*, Nizhny Novgorod, 2009, p. 63-64.

PROCESSING OPTICAL COHERENCE TOMOGRAPHY DATA AS A SYNTHETIC DIGITAL HOLOGRAM

A.A. Moiseev, **G.V. Gelikonov,** and **V.M. Gelikonov**

Institute of Applied Physics RAS, Nizhny Novgorod, Russia, aleksandr.moiseev@gmail.com

Abstract

The problem of restoration of Optical Coherence Tomography (OCT) images acquired with a tightly focused probing beam in out-of-focus region for improving lateral resolution of the OCT has been discussed in several works [1–5]. In the present work we show similarity between data acquisition in OCT and Digital Holography (DH). Some methods from the DH have been applied to the simulated OCT data acquired with a tightly focused scanning beam to restore micrometer lateral resolution in the whole investigated volume.

Method

We start with the wave backscattered from the object. We can write the field measured on the detector array in case of DH as

$$f_{DH}(x,y,k) = \int dz \cdot g_{DH}(x,y,z,k) \otimes o(x,y,z), \tag{1}$$

where $g_{DH}(x,y,z,k)$ denotes the point spread function of the DH system at distance z from the focal plane of the objective; $o(x,y,z)$ is an object's plane at distance z from the focal plane, $\otimes$ denotes convolution on *(x,y)* plane.

The field measured by lateral scanning of the OCT probe can be written in the form

$$f_{OCT}(x,y,k) = \int dz \cdot g_{OCT}^2(x,y,z,k) \otimes o(x,y,z), \tag{2}$$

where $g_{OCT}(x,y,z,k)$ denotes the point spread function of the OCT system at distance z from the focal plane of the objective (the square appears because the illumination and detection in the OCT system occur on the same optical path); $o(x,y,z)$ is an object's plane at distance z from the focal plane, $\otimes$ denotes convolution on the (x, y) plane. Note that in both cases we actually measure the interference between the object and the reference waves, and reconstruct the wave backscattered from the object, performing several measurements with different phase shift in the reference arm.

Assume that the apertures of the detector in the OCT and of each detector from the array in the DH are the same, and the imaging optics is also the same. The main goal of this work is compensation of defocusing, thus we suppose that the only influence of the imaging optics is defocusing: $g \sim \exp(i \cdot \alpha \cdot z \cdot (x^2 + y^2))$. Here α depends on illumination wavelength, aperture and numerical aperture of the imaging optics. One can see the similarity between both data sets. The OCT data looks like DH data, with all axial lengths two times "stretched" (we do not take into account any amplitude factors rise, for example, from the confocality of the OCT). Thus we can use the OCT data methods, developed for the DH data, for instance in [6], where DH was used for investigation of the biological samples. In this work, to restore the volume image of the object, the DH data at each wavelength has been decomposed into plane waves, these waves have been numerically propagated from the focal plane, and then volume data at all wavelengths have been summed up. It has also been shown that, under assumption of a small divergence angle, the summation may be performed utilizing Fast Fourier Transform:

$$S(x,y,z) = FT_{k_x,k_y,k}(FFF2d_C(k_x,k_y,k)_0 \cdot \exp(i \cdot \Delta z \cdot \frac{k_x^2 + k_y^2}{k})) \tag{3}$$

where

$$FFF2d_C(k_x,k_y,k)_0 = \iint f_{OCT}(x,y,k) \cdot \exp(i \cdot k_x \cdot x + i \cdot k_y \cdot y) \cdot dx \cdot dy \tag{4}$$

$k = 2 \cdot \pi / \lambda$ is a wavenumber, "stretching" of the OCT data relative to DC is taken into account. In the case of a tightly focused probing beam, this operation shifts the focal plane by distance Δz. By performing several such shifts, we can obtain one image focused in the whole investigated volume (this operation can be studied as "numerical focus fusion").

Results

To show the cabilities of the method, we simulate an OCT data as described in [2]. The results are shown in the figure. The left image is an initial OCT image, the next three images obtained by numerical shift of the focal plane according to the expressions (3), (4), and the right one is the image obtained by focus fusion.

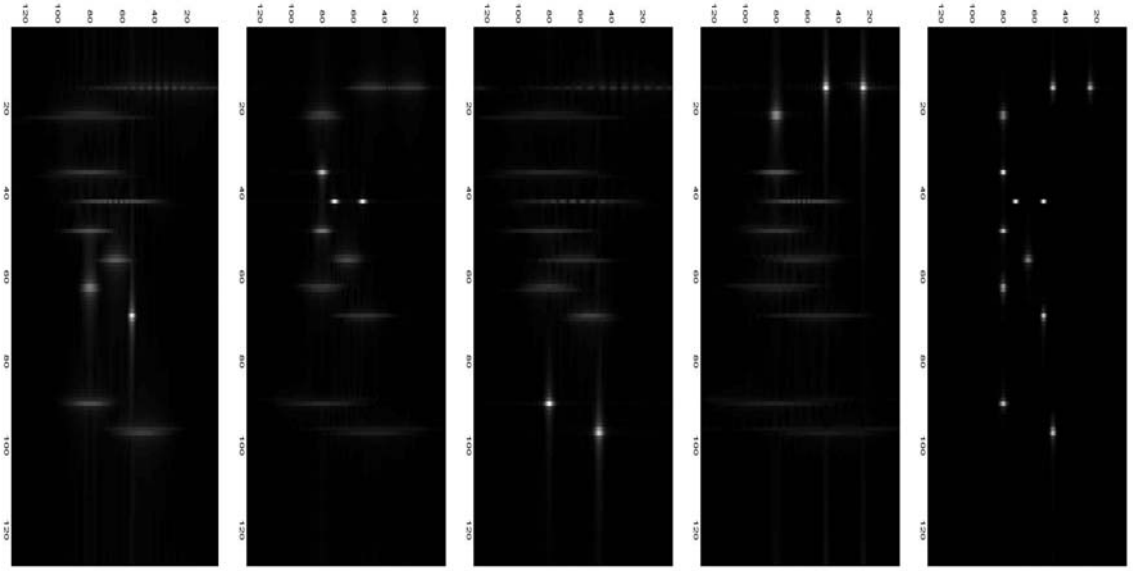

Acknowledgements

This research was supported in part by Contracts of the Russian Federation Nos. 02.740.11.0225 dated July 7 of 2009, 02.740.11.0516 dated March 15 of 2010, the Russian Foundation for Basic Research (grants Nos. 07-08-00803-a, 09-02- 00650-a, 11-02-01326-a), and the Council in Support of Leading Scientific Schools with the President of the Russian Federation (grant No. NSh 1931.2008.2).

References

1. T.S. Ralston, D.L. Marks, S.A. Boppart, *IEEE Transactions on Image Processing*, 2005, **14**, 1254-1264.
2. T.S. Ralston, D.L. Marks, P.S. Carney, S.A. Boppart, *J. Opt. Soc. Am. A*, 2006, **23**, 1027-1037.
3. Yu.L. Rao, B. Zhang, J. Su, J. Wang, Q. Guo, S. Chen, *Z. Opt. Express*, 2007, **15**, 7634-7641.
4. Y. Yasuno, J. Sugisaka, Y. Sando, Y. Nakamura, S. Makita, M. Itoh, T. Yatagai, *Opt. Express*, 2006, **14**, 1006-1020.
5. A.A. Moiseev, G.V. Gelikonov, P.A. Shilyagin, V.M. Gelikonov, *In: SPIE Photonics West, SPIE*, Ed. San Franisco, 2011.
6. D.V. Shabanov, G.V. Gelikonov, V.M. Gelikonov, *Laser Physics Letters*, 2009, **6**, 753-758.

POLARIZED REFLECTANCE SPECTROSCOPY BASED ON POLARIZATION MAINTAINING SINGLE MODE OPTICAL FIBER

A.N. Morozov[1], **V.A. Kamensky**[1], **M.Y. Kirillin**[1], and **M.A. Shakhova**[2]

[1] Institute of Applied Physics RAS, 46 Ulyanov str., Nizhny Novgorod, Russia, 603950
Tel: +7-831-4164923, e-mail: morozov@ufp.appl.sci-nnov.ru
[2] Nizhny Novgorod Regional Hospital, 190 Rodionov str., Nizhny Novgorod, Russia, 603126

The diagnostics of biological objects and tissues is an important problem in modern medicine [1, 2]. The overwhelming majority of malignant tumors are of epithelial origin and, at early stages of a disease, precancerous changes occur in the epithelial layer. Therefore, one of the most important requirements for early detection methods is the ability to reliably detect malignant changes on a comparatively small spatial scale, the thickness of epithelium. Today probably the most advanced techniques are based on endoscopic equipment. The most promising tissue structure examination methods compatible with endoscope are high frequency ultrasound [3], optical coherence tomography [4], and fluorescence spectroscopy [5, 6]. The fluorescence spectroscopy methods are highly sensitive, but suffer from low specificity to distinguish neoplastic changes [7, 8]. Methods for tumor diagnostics based on changes in the state of polarization in normal and cancer tissue were developed recently [9, 10]. The main idea for selection of backscattered light from biotissue is based on essential difference in optical characteristics of neoplastic epithelial cells and stromal fibers. Normal epithelial and malignant cells are considered to have a scatter polar pattern mainly forward without appreciable change in polarization state [11, 12]. Backscattered light from such tissues has the same state of polarization as incident light. Whereas stromal fibers are highly depolarized due to their anisotropic structure and backreflected intensity contains both initial and orthogonal polarization components. The main difference of the stromal medium from the epithelium is that it has a complicated three-dimensional collagen structure and light penetrating through it undergoes multiple scattering and rapidly depolarizes inside the collagen fibers. Sample tissue is irradiated by linearly polarized broadband near IR light from a single-mode polarization-maintaining optical fiber and after scattering inside the object the backreflected radiation is collected by the same fiber in two orthogonal polarizations. Probing radiation maintains its initial state of polarization during passage through the epithelium and then gets inside the stromal layer formed primarily by collagen fibers. In the current paper we present an all-fiber optic-endoscope-compatible device (Fig.1) for measuring the backscattered radiation and the effect of micro depolarization in biotissues − a subepithelial endoscopic polarized reflectance spectroscope.

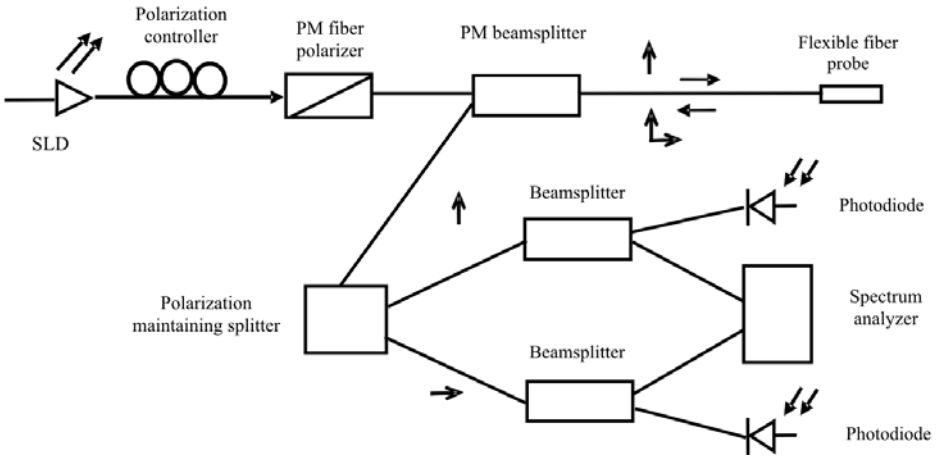

Fig. 1. Schematic of PM fiber-optic based polarized reflectance spectroscopy setup

The probing light from SLD with central wavelength $\lambda = 1310$ nm is sharply focused on the basal membrane (focal distance 500 μm) to acquire maximum signal from the subepithelium and to remove background noise from the upper layer. Intensity of the cross-polarization component is generally determined by the micro depolarization effect and scattering in stroma. In an incipient malignant

tumor, cancer cells usually weakly depolarize probing light along basal membrane and the reflected depolarized intensity is much less than in normal tissue. Also, we acquire spectral information from backscattered radiation in orthogonal polarization. Our fiber-optic probe is custom made with 1.4 mm diameter compatible with biopsy channel of commercially available endoscopes and bronchoscopes so we can examine mucous membranes of hollow organs and serous cover of cavities. The optical power from the fiber probe was measured to be 7 mW. The polarization extinction ratio of the setup was measured to be 23 dB. With the use of the polarized reflectance spectroscopy method we expect to differentiate normal and cancerous tissue by tracking the amplitude of orthogonal component. *Ex vivo* studies were carried out on resected larynx malignant tumors (Fig. 2).

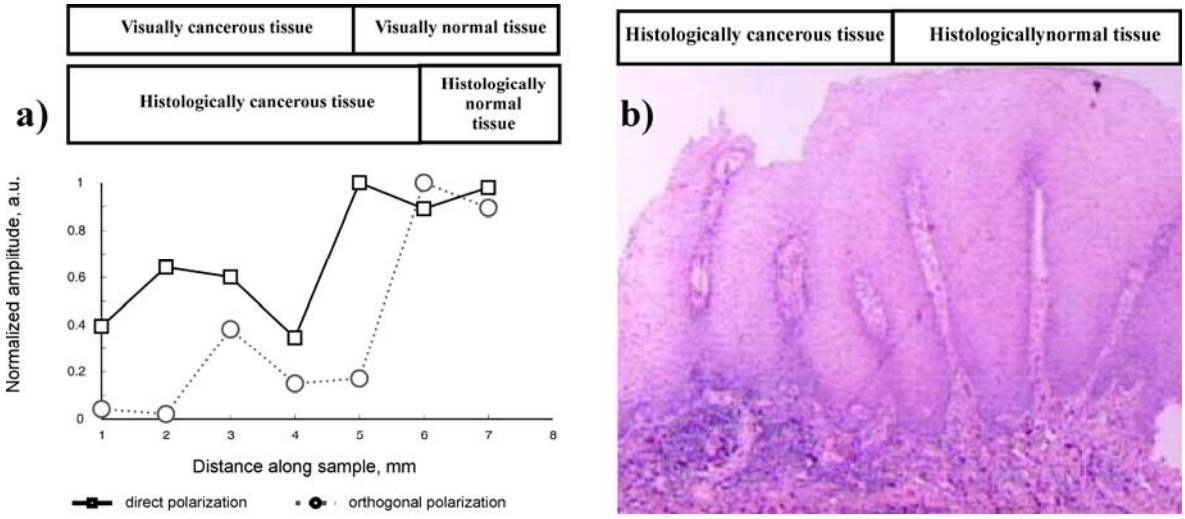

Fig. 2. a) Normalized amplitude of the orthogonal component of detected signal as a function of coordinate along colon sample. b) Histological image of larynx tumor

We conjecture that noninvasiveness and absence of unwanted side effects of the polarized reflectance spectroscopy method allows it to be used for dynamic examination – intraoperative observation and pathologic processes monitoring during treatment. Ability for real time information acquisition can be beneficial when it is necessary to make a rapid decision during treatment manipulation.

Acknowledgements. We acknowledge the contribution of Dr. Nataliya Shakhova for discussions. The work was supported by grants from the Russian Foundation for Basic Research (Nos. 10-02-00744, 10-08-00744 and 11-02-01129) and the grant of the Government of Russian Federation №.11.G34.31.0017.

References

1. A. Jemal, R. Siegel, E. Ward, T. Murray, J. Xu, and M. Thun, *CA Cancer J. Clin*, 2007, **57**(1), 43–66.
2. D. M. Parkin, F. Bray, J. Ferlay, and P. Pisani, *CA Cancer J. Clin,* 2005, **55**(2), 74–108.
3. C. Arens and H. Glanz, *Eur. Arch. Otolaryngol.*, 1999, **256**(6), 316–322.
4. W. Drexler and J. G. Fujimoto, eds., Springer, (2008).
5. M. Mitchell, S. Cantor, C. Brookner, U. Utzinger, D. Schottenfeld, and R. Richards-Kortum,, *J. Obstet. Gynecol*., 1999, **94**(5), 889–896.
6. R. Drezek, C. Brookner, I. Pavlova, I. Boiko, A. Malpica, R. Lotan, M. Follen, and R. Richards-Kortum, *Photochemistry and Photobiology.*, 2001, **73**(6), 636–411.
7. M.J. Swinn, M.M. Walker, L.J. Harbin et al., *Eur. Urology*., 2004, **45**(4), 471–474.
8. V.V. Sapozhnikova, N.M. Shakhova, V.A. Kamensky, S.A. Petrova, L.B. Snopova, and R.V. Kuranov, *Laser Physics*., 2005, **15**(12), 1664–1673.
9. S.L. Jacques, J.C. Ramella-Roman, and K. Lee, *J. Biomed. Opt.*, 2002, **7**(3), 329–340.
10. R.V. Kuranov, V.V. Sapozhnikova, I.V. Turchin, E.V. Zagainova, V.M. Gelikonov, V.A. Kamensky, L.B. Snopova, and N.N. Prodanetz, *Optics Express*., 2002, **10**(15), 707–713.
11. R.S. Gurjar, V. Backman, L.T. Perelman, I. Georgakoudi, K. Badizadegan, I. Itzkan, R.R. Dasari, and M.S. Feld, *Nature Medicine*, 2001, **7**(11), 1245–1248.
12. J.M. Schmit and S.H. Xiang, *Optics Letters*, 1998, **23**(13), 1060–1062.

MONITORING OF EXPERIMENTAL TUMOR OXYGENATION BY DIFFUSE OPTICAL SPECTROSCOPY

A.G. Orlova[1], A.V. Maslennikova[1,2,3], G.Yu. Golubiatnikov[1], V.A. Kamensky[1], T.I. Pryanikova[1,2], V.I. Plekhanov[1], I.P. Ivanova[3], T.V. Smirnova[2], N.M. Shakhova[1,3], and **I.V. Turchin[1]**

[1] Institute of Applied Physics RAS, Nizhny Novgorod, Russia, orlova@ufp.appl.sci-nnov.ru
[2] N.I. Lobachevsky State University of Nizhny Novgorod, Nizhny Novgorod, Russia
[3] Nizhny Novgorod State Medical Academy, Nizhny Novgorod, Russia

Tumor oxygen state is considered to be one of the key factors influencing the malignant tumor prognosis and treatment effectiveness [1]. Estimation of tumor oxygenation in the course of the therapy may be of great importance for choosing the optimal therapeutic strategies as well as for assessing treatment efficiency. Moreover, investigation of dynamics of oxygenation is required for testing the agents developed for hypoxic tumors reoxygenation to improve their sensitivity to therapy. As a method of *in vivo* assessing the tumor oxygen status under the influence of different types of treatment the method of diffuse optical spectroscopy (DOS) has been used. It is capable to provide information concerning the oxygen status of biological tissues [2]. The goal of the current study was to investigate the capabilities of DOS for monitoring of oxygenation of experimental tumor models and for studying the biological effects of the chemotherapy, radiation therapy and hemorrheologic agent pentoxifylline (Ptx).

The experiments were carried out on white outbred rats. Pliss's lymph sarcoma (PLS) was transplanted subcutaneously into the inner side of the thigh of the animal. Twenty six male tumor-bearing animals were used. Experiments on DOS were performed on the experimental setup with parallel plane geometry created at the Institute of Applied Physics RAS (Nizhny Novgorod, Russia) [3]. Illumination at three wavelengths (684 nm, 794 nm, and 850 nm) which correspond to different parts of the absorption spectrum in a therapeutic transparency window provides information about concentration of the main absorbers (oxygenated hemoglobin, deoxygenated hemoglobin, and fat/water). The use of high-frequency (140 MHz) amplitude modulation allows determination of absorption coefficients more accurately due to separate determination of scattering and absorption coefficients.

Before the investigation animals were anaesthetized and immobilized on a transparent plastic plate; the tumor region were positioned into the scanning area. During scanning, animals were placed into a cuvette containing the immersion liquid with definite optical parameters. The images were obtained by simultaneous scanning by moving the source and the detector located along the sagittal axis from the opposite sides of the studied subject with a step of 1–2 mm synchronously. The distribution of concentrations of oxygenated, deoxygenated and total hemoglobin, as well as blood oxygen saturation level in the tissues was reconstructed numerically. In the case of chemotherapy single doses of cyclophosphane (50 mg/kg) were injected intraperitoneally. In the case of radiation therapy tumors were irradiated with single doses of 30 Gy. As a control, untreated animals were used. In the case of oxygen-modifying action single doses of Ptx (50 mg/kg) were injected intraperitoneally. The DOS investigation was performed before and 90 min after Ptx treatment.

DOS allows observing dynamics of tissue oxygen saturation in the process of tumor natural growth, as well as after cyclophosphane and radiation treatment. In the course of a natural growth, Pliss's lymph sarcoma demonstrated a pronounced decrease of blood saturation in the tumor zone (Fig. 1). Chemo- and radiation therapy inhibit tumor growth and cause the increase of the blood oxygen saturation as compared with untreated animals. Such effect may be explained by inhibition of tumor cells division and their death, decrease in interstitial pressure, leading to increased oxygen availability, decrease in oxygen consumption and improvement of oxygen supply of the tumor [4, 5].

Figure 2 shows changes of blood oxygen saturation level after pentoxyphillin injection. Ptx treatment causes substantial raise of blood oxygen saturation in the tumor area. Pentoxifylline is a hemorrheologic agent with the ability to improve tumor perfusion [6]. It is of interest in radiation oncology because the improvement of tumor perfusion might result in better oxygenation and thus higher radiosensitivity.

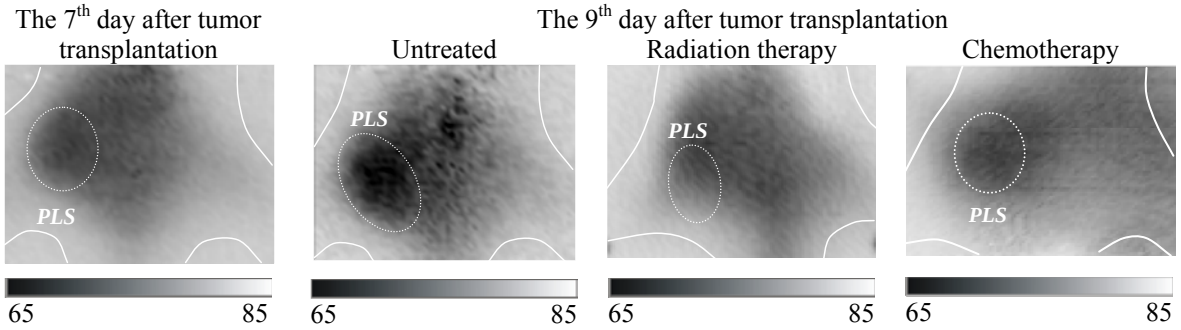

Fig. 1. Blood oxygen saturation level (%) of Pliss's lymph sarcoma during natural growth (untreated), and under radiation therapy and chemotherapy influence. Solid lines contour the animal body within the zone of scanning; dotted lines contour the tumor area. Image size 60×70 mm

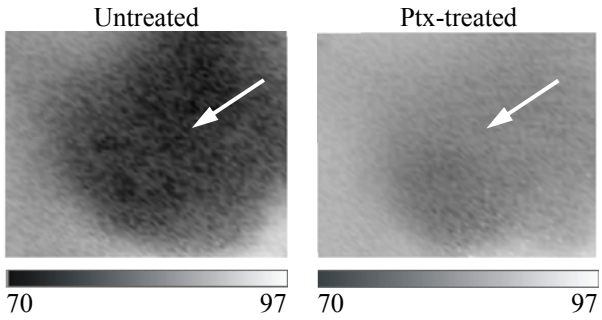

Fig. 2. Blood oxygen saturation level (%) of Pliss's lymph sarcoma before and after 90 min after Ptx injection. The arrows show the tumor. Image size 70×70 mm

Our research demonstrated the capabilities of the DOS for *in vivo* noninvasive monitoring of experimental tumors for estimation their blood oxygen saturation level in response to chemotherapy, radiotherapy and oxygen-modifiers action. This method may be used both in experimental oncology for development of new approaches of cancer treatment and in clinical practice for investigation of tumor oxygenation dynamics under therapy influence.

Acknowledgements

This work was partly supported by the Russian Foundation for Basic Research (10-02-01142) and the Program of RAS Presidium "Fundamental Sciences for Medicine".

References

1. P. Vaupel, *Oncologist*, 2008, **13**, 21-26.
2. B.J. Tromberg, A. Cerussi, N. Shah, M. Compton, A. Durkin, D. Hsiang, J. Butler, and R. Mehta, *Breast Cancer Research,* 2005, **7**, 279-285.
3. A.V. Maslennikova, A.G. Orlova, G.Yu. Golubiatnikov, V.A. Kamensky, N.M. Shakhova, A.A. Babaev, L.B. Snopova, I.P. Ivanova, V.I. Plekhanov, T.I. Prianikova and I.V. Turchin, *Journal of Biophotonics*, 2010, **3**(12), 743-751.
4. H. Poptani, N. Bansal, W.T., Jenkins, D. Blessington, A. Mancuso, D.S. Nelson, M. Feldman, E.J. Delikatny, B. Chance, J.D. Glickson., *Cancer Res.*, 2003, **63**(15), 8813-8820.
5. N. Crokart, B.F. Jordan, C. Baudelet, P. Sonveaux, V. Gregoire, N. Beghein, J. Dewever, C. Bouzin, O. Feron, B. Gallez, *Int. J. Radiation Oncology Biol. Phys.*, 2005, **3**, 901-910.
6. F. Zywietz, L. Bohm, C. Sagowski, W. Kehrl, *Strahlenther Onkol.*, 2004, **180**, 306-314.

THE STUDY OF CYCLOPHOSPHANE EFFECT ON BLOOD OXYGEN SATURATION LEVEL IN TUMOR MODELS USING DIFFUSE OPTICAL SPECTROSCOPY

T.I. Pryanikova[1,2], A.V. Maslennikova[1,2,3], A.G. Orlova[1], G.Yu. Golubiatnikov[1], V.A. Kamensky[1], V.I. Plekhanov[1], I.P. Ivanova[3], N.M. Shakhova[1,3], and **I.V. Turchin[1]**

[1]N.I. Lobachevsky State University of Nizhny Novgorod, Russia, tipryanikova@mail.ru
[2]Institute of Applied Physics RAS, Nizhny Novgorod, Russia
[3]Nizhny Novgorod State Medical Academy, Russia

The main method of estimation of chemotherapy efficiency in experimental animal models is the survival and monitoring of tumor volume in the course of treatment. However, this method does not provide information concerning important biological and physiological features of tumor. In particular, data about changes of tumor oxygenation upon administration of cytostatic drugs are of great importance because they can indicate the therapeutic response [1]. Noninvasive investigation of this parameter is available only by means of special methods of tissue visualization, such as MRI and PET [2]. Alternative noninvasive imaging modality for detecting and assessing tumor oxygenation is diffuse optical spectroscopy (DOS) capable of providing information on blood oxygen saturation in tissues [3]. The goal of the current study is to investigate the capabilities of DOS for monitoring tumor tissue oxygen saturation under the influence of chemotherapy.

The investigation was performed on the experimental setup with parallel plane geometry and three wavelengths (684, 794 and 850 nm) created at the Institute of Applied Physics RAS (Nizhny Novgorod, Russia). These wavelengths provide information about the principal tissue absorbers: oxygenated hemoglobin (HbO_2) and deoxygenated hemoglobin (HHb). Oxygen saturation level in tissues was computed as $StO_2=[HbO_2]/[HbO_2+HHb]$.

Pliss's lymph sarcoma (PLS) was transplanted subcutaneously into the thigh of the white outbred rats. The tumor is characterized by a high mitotic activity, high cellularity, a rapid growth and low oxygen state [4]. *In vivo* investigation of PLS model was performed during the process of a native tumor growth and in the course of the treatment with cyclophosphane. HHb, HbO_2 content and blood saturation level were studied. The first DOS procedure was carried out on the 4^{th} day of tumor growth when the tumors reached 13-16 mm in diameter. An alkylating drug cyclophosphane was chosen as a chemotherapeutic agent. A single dose of cyclophosphane was injected i.p. on the day of first DOS investigation. A series of DOS procedures were carried out sequentially every 2-3 days. During scanning, animals were placed into an immersion liquid – water solution of lypofundin with added Indian ink. Acquisition of one tumor image took 15 min. The external tumor sizes were measured before every DOS investigation.

In the process of its natural growth during the observation period, tumor volume increased eventually. The substantial decrease of tumor growth rate was observed after cytostatic drug intake. Natural tumor evolution was accompanied by the decrease of blood saturation level. This effect was determined by the increase of HHb content and the decrease of HbO_2 content. Under the action of chemotherapy, tumor blood oxygen saturation rose because of the increase of oxygenated hemoglobin concentration and the decrease of deoxygenated hemoglobin concentration in the tumor zone as compared with untreated animals. An example of DOS-images of LSP obtained on the 4^{th} and 9^{th} day after tumor cells suspension inoculation is given in figure 1.

According to [5], in case of rapidly growing tumors, the decrease of blood oxygen saturation during their natural evolution occurs due to reduction of tissue perfusion. Insufficient blood flow in tumor vessels leads to disruption of oxygenated hemoglobin supply and inhibition of deoxygenated hemoglobin removal. According to [6], the increase of tumor blood oxygen saturation under chemotherapy treatment influence is connected with the decrease in oxygen consumption.

It has been shown that DOS allows visualizing oxygen blood saturation of tumor model and tracing its changes in the course of tumor natural growth as well as under chemotherapy impact.

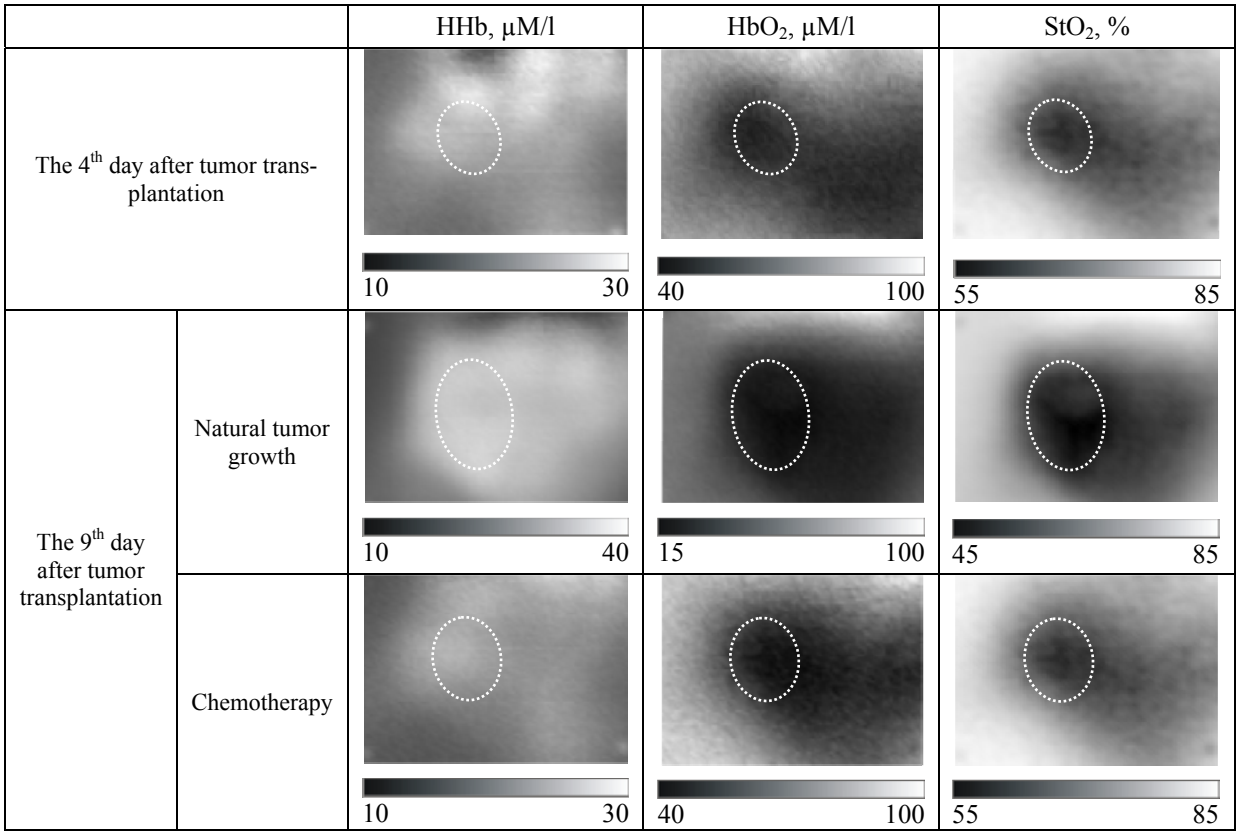

Fig. 1. Results of DOS study of PLS area:
distribution of the content of deoxygenated and oxygenated hemoglobin, blood oxygen saturation level.
Dotted lines contour the tumor area. DOS image size 60×70 mm

Acknowledgements

This work was partly supported by the Russian Foundation for Basic Research (10-02-01142) and the Program of RAS Presidium "Fundamental Sciences for Medicine".

References

1. U. Duvvuri, H. Poptani, M. Feldman, L. Nadal-Desbarats, M.S. Gee, W.M.F. Lee, R. Reddy, J.S. Leigh, and J.D. Glickson, *Cancer Research*, 2001, **61**, 7747-7753.
2. I. Serganova, J. Humm, C. Ling, R. Blasberg, *Clinical Cancer Research*, 2006, **12**(18), 5260-5264.
3. B.J. Tromberg, A. Cerussi, N. Shah, M. Compton, A. Durkin, D. Hsiang, J. Butler, and R. Mehta, *Breast Cancer Research,* 2005, **7**, 279-285.
4. A.V. Maslennikova, A.G. Orlova, G.Yu. Golubiatnikov, V.A. Kamensky, N.M. Shakhova, A.A. Babaev, L.B. Snopova, I.P. Ivanova, V.I. Plekhanov, T.I. Prianikova and I.V. Turchin, *Journal of Biophotonics*, 2010, **3**(12), 743-751.
5. B.M. Fenton, E.M. Lord, S.F. Paoni*, Int. J. Cancer*, 2001, **93**, 693-698.
6. H. Poptani, N. Bansal, W.T., Jenkins, D. Blessington, A. Mancuso, D.S. Nelson, M. Feldman, E.J. Delikatny, B. Chance, J.D. Glickson, *Cancer Res.*, 2003, **63**(15), 8813-8820.

Invited

METHODS, APPLICATIONS AND RELEVANT LIGHT DOSES IN 3D FLUORESCENCE MICROSCOPY

H. Schneckenburger[1,2], P. Weber[1], M. Wagner[1], T. Bruns[1], V. Richter[1], S. Schickinger[1], and **R. Wittig[2]**

[1]Hochschule Aalen, Institut für Angewandte Forschung, Beethovenstr. 1, 73430 Aalen, Germany
e-mail: herbert.schneckenburger@htw-aalen.de
[2]Institut für Lasertechnologien in der Medizin und Messtechnik an der Universität Ulm
Helmholtzstr. 12, 89081 Ulm, Germany

Use of 3D models and application of low light doses are present challenges in live cell fluorescence microscopy. To fulfil these requirements, structured as well as single plane illumination techniques were established, and maximum light doses for maintaining cell viability were determined. In addition, cell-substrate topology was measured with nanometre precision by variable-angle Total Internal Reflection Fluorescence Microscopy (VA-TIRFM). Tomographic, spectroscopic and time-resolved methods were applied for detection of tumours and neurodegenerative diseases (e.g. M. Alzheimer) as well as for imaging various properties of living cells (e.g. membrane stiffness).

Introduction

Spatial resolution is a key parameter of modern fluorescence microscopy. While light diffraction commonly limits lateral as well as axial resolution, further restrictions are due to a low focal depth at high magnification when images from a focal plane are superposed by out-of-focus light. This plays a predominant role, if conventional 2-dimensional cell cultures (growing e.g. on a glass slide) are replaced by 3D systems, e.g. cell spheroids or tissue samples. Therefore, methods of optical sectioning are required, where information from individual planes is selected and possibly combined in a high-resolution 3-dimensional image. Those techniques include laser-scanning microscopy (LSM) as well as wide-field microscopy with structured [1] or single plane (SPIM) [2] illumination. In addition, fluorescence imaging with nanometre resolution close to cell surfaces became possible by variable-angle Total Internal Reflection Fluorescence Microscopy (VA-TIRFM) [3, 4].

In multi-dimensional microscopy spatial resolution is often combined with high spectral or temporal resolution, thus resulting in spectral imaging or fluorescence lifetime imaging microscopy (FLIM). In addition to precise localization of fluorescent probes these techniques often permit to measure intermolecular interactions with their micro-environment. Non-radiative (Förster resonance) energy transfer (FRET) from a donor to an acceptor molecule plays an important role in this context, since intermolecular distances below 10 nm can be detected reliably.

With increasing magnification illuminated areas in a microscope decrease considerably, and power densities often exceed solar irradiance (100 mW/cm² or 1 nW/µm²) by several orders of magnitude. This may cause severe damage to living cells [5] and requires microscopic methods of low light exposure. For this reason, all experiments were performed under strict limitation of the light dose in order to maintain cell viability.

Materials and Methods

Human glioblastoma cells were cultivated either as monolayers on glass slides or as spheroids of about 300 µm diameter. Cell viability was tested using a colony forming assay [5] and strictly maintained in all experiments. U251-MG cells kindly supplied by Prof. Jan Mollenhauer, Dept. of Molecular Oncology, University of South Denmark, Odense, were used as a model system for tumour detection. In two subclones of those cells tumour suppressor genes were over-expressed, such that cells may be regarded as less malignant. For measuring the proximity and possible interaction of proteins relevant in the pathogenesis of M. Alzheimer, U373-MG cells were transfected with β-secretase (BACE)-GFP and amyloid precursor (APP)-RFP encoding plasmids. Membrane dynamics was studied with the polarity sensitive marker 6-dodecanoyl-2-dimethylamino naphthalene (laurdan) incorporated into cell membranes.

In addition to conventional fluorescence microscopy, laser scanning microscopy as well as structured or single plane illumination techniques were used. Furthermore, variable-angle TIRFM permitted selective studies of plasma membranes. Fluorescence imaging with ultra-sensitive detection

by an electron multiplying (EM-)CCD camera was combined with spectral analysis and fluorescence lifetime measurements.

Results and Discussion

Present results can be summarized as follows:

Various imaging methods, e.g. LSM, structured illumination or SPIM, are available for 3-dimensional cell or tissue samples, permitting moderate resolution and decreasing light exposure in the order LSM → structured illumination → SPIM.

High resolution or super-resolution microscopy requires single cells, specific techniques (e.g. VA-TIRFM) and higher light doses which may easily attain the limit for cell damage.

Additional use of spectral or temporal resolution provides further information, e.g. for precise localization of fluorophores or measurements of intermolecular interactions.

Spectral as well as fluorescence lifetime measurements of specific coenzymes can be used to distinguish tumour cells from less malignant cells.

FLIM and FRET experiments can be used to probe molecular interactions in the pathogenesis of M. Alzheimer [6] or further diseases.

Spectral and temporal resolution can be used to measure membrane stiffness and fluidity, e.g. in the presence of various metabolites or pharmaceutical agents.

These and further applications prove the large potential of multi-dimensional fluorescence microscopy in life cell imaging.

Acknowledgment

Present research is funded or financed by Land Baden-Württemberg, Europäische Union – Europäischer Fonds für die regionale Entwicklung, Bundesministerium für Bildung und Forschung (BMBF) and Baden-Württemberg-Stiftung gGmbH.

References

1. M.A.A. Neil, R. Juskaitis R, and T. Wilson, *Opt. Lett*., 1997, **22**, 1905–1907.
2. J. Huisken, J, Swoger, F. del Bene, J. Wittbrodt, and E.H.K. Stelzer, *Science,* 2004, **305**, 1007–1009.
3. H. Schneckenburger*, Curr. Opin. Biotechnol*., 2005, **16**, 13-18.
4. M. Wagner, P. Weber, W.S.L. Strauss, H.-P. Lassalle, and H. Schneckenburger, *Advances in Optical Technologies*, 2008, Vol. **2008**, Doi:10.1155/2008/254317.
5. M. Wagner, P. Weber, T. Bruns, W.S.L. Strauss, R. Wittig, and H. Schneckenburger, *Int. J. Mol. Sci.*, 2010, **11**, 956–966.
6. C.A.F. von Arnim, B. von Einem, P. Weber, M. Wagner, D. Schwanzar, R. Spoelgen, W.S.L. Strauss, and H. Schneckenburger, *Biochem. Biophys. Res. Commun*., 2008, **370**, 207−212.

REFINED FORWARD PROBLEM SOLUTION FOR BIOTISSUE OPTICAL PROPERTIES RECONSTRUCTION

E.A. Sergeeva, A.R. Katichev, and **M.Yu. Kirillin**

Institute of Applied Physics RAS, Nizhny Novgorod, Russia, sea@ufp.appl.sci-nnov.ru

Many optical biomedical modalities are based on monitoring biological tissue optical properties changes related to functional activity or structural transformations. One of the fundamental problems here is reconstruction of the desired optical properties from the measured optical signals of radiation transmittance and/or reflectance. This task is considered as the inverse problem of optical tomographic or spectroscopic techniques and it requires adequate solution of the forward problem of radiation transport in the media with scattering and absorption properties close to those of biotissue. The most general approach to study propagation of light in the media with strong anisotropic scattering and comparatively low absorption is the radiation transfer theory (RTT) [1] which allows obtaining relations between the intensity of light exciting the examined medium at a definite point (a characteristic typically measured in the experiment) and medium optical parameters. However, the range of analytical solution in RTT is quite limited due to complexity of the basic equations even for simplest geometries of the medium. The most thoroughly examined RTT model is diffusion approximation which leads to Helmholtz type equation easy to solve both analytically and numerically. The crucial restriction of this approximation, however, is its inapplicability for source-detector separations comparable to or smaller than the transport length l_t. This means that it cannot be used, for example, for optical properties reconstruction in the modalities based on back-reflectance measurements and for integrating sphere measurements of relatively thin tissue samples (with a thickness up to a few mm).

We propose a novel solution to the forward problem of light propagation in biotissues based on a hybrid approach for calculating intensity of a collimated beam in case of highly anisotropic scattering. The proposed model operates only with the parameters which govern diffusion of light, namely, absorption coefficient μ_a and reduced scattering coefficient μ_s'. We consider the total energy density in the medium as the sum of the directed component and the diffusive component

$$I = I_{dir} + I_{diff}, \tag{1}$$

where the directed component is formed by collimated light and light scattered at small angles (which corresponds to least-scattered photons). These kinds of photons are not accounted for by the diffusion approximation. If the collimated probing beam of total power P_0 enters the medium at the boundary $z = 0$ along the z-direction, then [2]

$$I_{dir}(\mathbf{r}_\perp, z) = P_0 \exp(-\mu_t' z)\delta(\mathbf{r}_\perp)\mathrm{m}, \tag{2}$$

where $\mu_t' = \mu_a + \mu_s' = 1/l_t$ is a reduced attenuation coefficient. The diffusive term I_{diff} can be calculated from the diffusion equation with the source term defined by the directed component [1]

$$\left(\Delta - 3\mu_a\mu_t'\right) I_{diff}(\mathbf{r}_\perp, z) = -3\mu_s'\mu_t' I_{dir}(\mathbf{r}_\perp, z), \tag{3}$$

using Green function formalism and proper boundary conditions.

We used the proposed approach to demonstrate reconstruction of the parameters μ_a and μ_s' from the spatially resolved reflectometry and integrating sphere measurements, and compared our results with the results of reconstruction based on the diffusion approximation.

1. Spatially resolved reflectometry (SRR) with small source-detector separation

This problem is important for diffuse back-reflectance spectroscopy, an optical diagnostic technique which uses spectroscopic data to estimate the degree of tissue oxygen saturation. We employed numerical Monte Carlo simulation to model intensity of scattered light of a collimated source at two fiber detectors co-aligned with the source and transversally separated from it at the distances of $0.7l_t$ and $1.5l_t$, respectively. The simulated signals obtained for media with various absorption and scattering coefficients served as input data for the processing procedure which utilizes either the hybrid approach (HA) or the conventional diffusion approximation (DA) as the solution of the forward problem. The results of reconstruction of μ_a and μ_s' are displayed in Table 1 for both approaches. It is evident that evaluation of optical parameters using HA provides better agreement with the input values. Especially the discrepancy between the true and reconstructed values of μ_a is significantly less for HA-based reconstruction which is of high importance in diagnostic techniques based on monitoring of hemoglobin concentration.

Table 1. Optical parameters reconstruction in SRR, mm^{-1}

Input parameters		Parameters reconstructed using HA		Parameters reconstructed using DA	
μ_a	μ_s'	μ_a	μ_s'	μ_a	μ_s'
0.01	2	0.0075	1.93	0.03	2.08
0.1	2	0.1	1.86	0.18	1.96
0.01	4	0.008	3.98	0.045	4.38
0.1	4	0.1	3.9	0.2	4.27

2. Integrating sphere measurements for an arbitrary sample thickness

Typically the problem of reconstruction of biotissue optical parameters from the total reflectance and transmittance measured by integrating sphere is based on Kubelka-Munk two-flux model empirically related to diffusion approximation (KMDA) [3]. To meet the conditions of diffusion approximation the sample thickness should exceed the transport length. However, increased sample thickness leads to the power losses. Besides, the KMDA approach does not account for air-tissue refractive index mismatch which significantly affects the quality of reconstruction. In the proposed forward model based on the hybrid approach we have incorporated modified Milne boundary conditions which account for the refractive index mismatch at the both sides of the sample. This makes the HA-based model more realistic than the KMDA model. In addition, the novel approach is valid if the sample thickness is less than the transport length.

We have verified the HA-based model and the KMDA model of the forward problem by comparing the calculated transmittance and reflectance with the results of Monte Carlo simulations in a wide range of optical parameters. The HA-based model provided much better agreement with numerical data than the KMDA model. We later applied both forward-problem solutions to evaluate rat brain spectra of μ_a and μ_s' from the measurement data found in the literature [4]. The results of reconstruction using the HA-based model versus the KMDA model are displayed in Fig. 1. Discrepancy of the results obtained from different models reaches 100%. The presented results demonstrate to which extent the reconstruction outcome depends on the choice of an adequate theoretical model. Proving the validity of the utilized model in the given range of the parameters plays a significant role in correct assessment of optical properties.

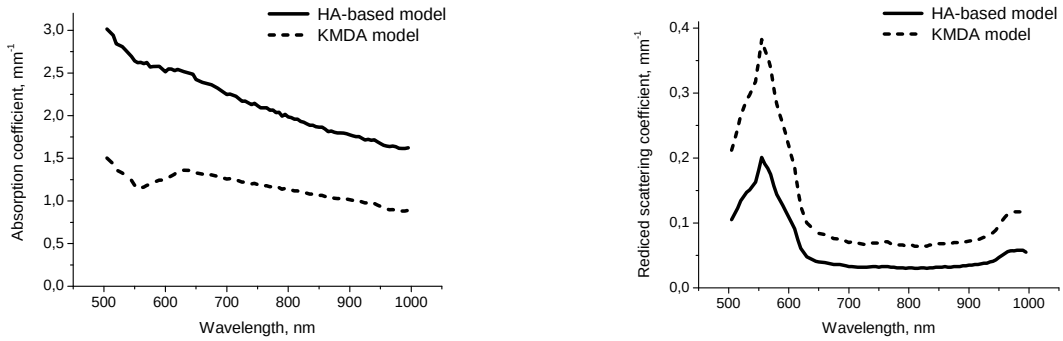

Fig. 1. Spectra of rat brain reconstructed optical parameters

This work was supported by the Russian Foundation for Basic Research (grants 10-02-00744, and 11-02-01129), grant of the President of the Russian Federation MK-1127.2010.2, FTP "Scientific and Scientific-Educational Staff of Innovative Russia" (projects 14.740.11.0253, 02.740.11.0839 and 02.740.11.0566).

References

1. A. Ishimaru, *Wave Propagation and Scattering in Random Media,* New York: Plenum Press, 1978.
2. L.S. Dolin, *Radiophys. Quantum Electron.*, 1998, **41**(10), 850-873.
3. W.F. Cheong, S.A. Prahl, A.J. Welch, *IEEE Jour. Quantum Electron.*, 1990, **26**, 2166-2185.
4. Pieter van der Zee, *Measurement and Modelling of the Optical Properties of Human Tissue in the Near Infrared*, (Ph.D Thesis, Department of Medical Physics and Bioengineering, University College London, 1992).

LIFETIME IMAGING: FROM PICOSECONDS TO MILLISECONDS

W. Becker, V. Shcheslavskiy, B. Su, and **A. Bergmann**

Becker&Hickl GmbH, Nahmitzer Damm 30, 12277 Berlin, Germany
vis@becker-hickl.de

Introduction

There is a number of radiative relaxation processes which occur on a much longer time scale than fluorescence. One of the most known is phosphorescence, i.e. emission from the triplet state of organic dyes. Phosphorescence can be quenched by oxygen. The effectiveness of the phosphorescence quenching depends on the frequency of collisions between the triplet state molecules and molecular oxygen [1]. This fact provides the basis for using phosphorescence as a tool for measuring oxygen concentration in biological systems [2]. One of the important advantages of the tool, that it is noninvasive. Imaging of oxygen distributions is of great importance for neuroscience, for example, where the ability to image brain oxygenation is critical for understanding neuronal activation [3].

Most of the phosphorescence imaging experiments are done with wide area illumination in combination with CCD detection. While such an approach provides fast data acquisition, it results in poor spatial resolution. To overcome it, two-photon laser scanning microscopy has been applied as alternative method to image partial oxygen pressure [4]. However, in many cases it would be extremely useful to have simultaneously both fluorescence and phosphorescence lifetime information. To be able to record lifetime images from picoseconds to milliseconds time range both with high temporal and spatial resolution, laser scanning technique with the detection based rather on PMT than on CCD is required. Here we report a new approach to a lifetime imaging in broad time range from picoseconds to milliseconds, based on a confocal laser scanning microscope.

Experimental setup

To obtain both fluorescence and phosphorescence lifetimes we use the principle, shown in Fig. 1. A high-frequency pulsed laser is turned on only for a short period of time, t_{on}, at the beginning of each pixel. For the rest of the pixel time the laser is turned off. During the on-period, the laser excites fluorescence, and builds up phosphorescence. Within the off period, t_{off}, pure phosphorescence is obtained. The modulation of the laser is controlled by bh FLIM system.

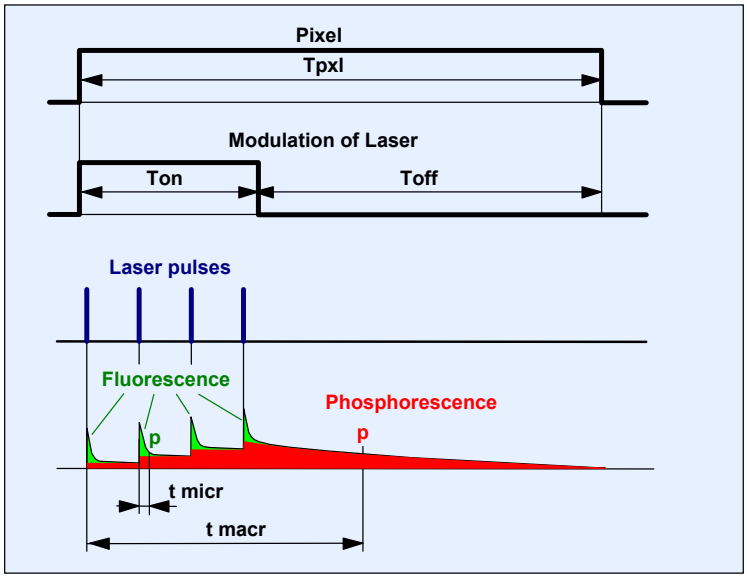

Fig. 1. Principle of FLIM from picoseconds to milliseconds

To demonstrate simultaneous recording of fluorescence and phosphorescence we used a bh TCSPC FLIM module attached to a Zeiss LSM 710 NLO multiphoton microscope [5]. The luminescence was collected through the non-descanned beam path of the LSM 710. The photons were detected by bh HPM-100-40 hybrid detector. As a sample we used yeast cells stained with a ruthenium dye.

Results

Intensity images of yeast cells are shown on Fig. 2.

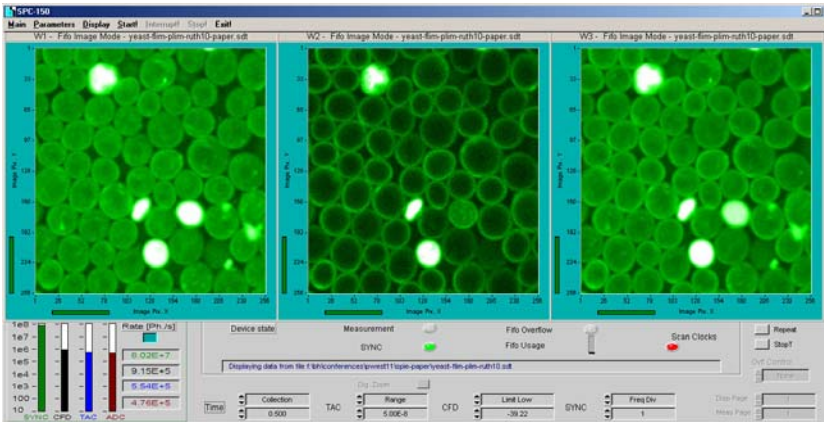

Fig. 2. Intensity images of yeast cells stained with a ruthenium dye. Images from left to right: fluorescence, phosphorescence, total emission. Phosphorescence mainly comes from the cell membrane to which the ruthilium dye binds. Two-photon excitation at 780nm

Lifetime images obtained from the same data set are shown in Fig. 3 with the corresponding decay curves in the selected spot (Fig. 4).

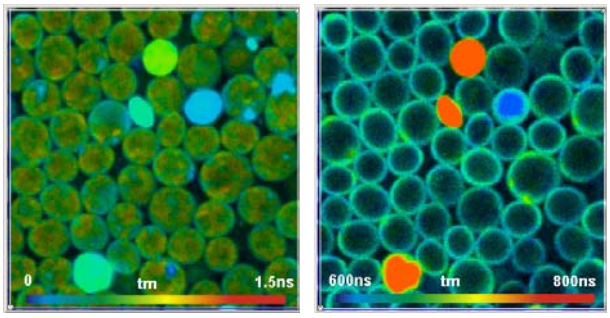

Fig. 3. Fluorescence image (left) and phosphorescence image (right) of yeast cells

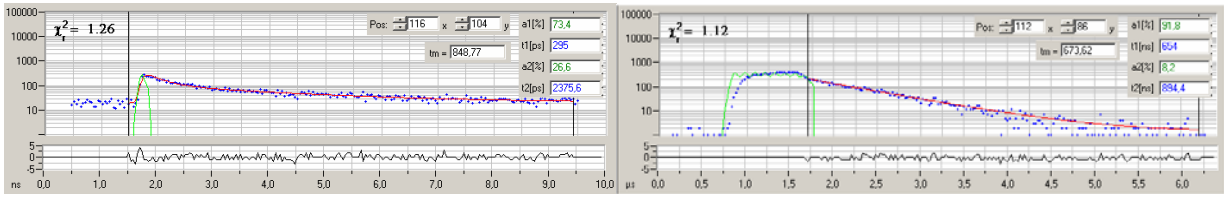

Fig. 4. Decay curves in the selected spot of Fig. 3. Left: fluorescence. Right: phosphorescence

Summary

The technique described above simultaneously records fluorescence and phosphorescence lifetime images in confocal and multiphoton laser scanning systems. It eliminates the requirement of using pulse picker for reduction of the pulse repetition rate, and avoids excessively high pulse power at low excitation rate. Potential applications include oxygen concentration measurements with simultaneous monitoring cell metabolism via autofluorescence signals, identification of nanoparticles in cosmetical products in the skin.

References

1. J. Callis, J. Knowles, and M. Gouterman, *J. Phys. Chem.*, 1973, **77**, 154-156.
2. A. Lebedev, A. Cherpakov, S. Sakadzic et al, *Appl. Materials & Interfaces*, 2009, **1**, 1292-1304.
3. J. Thompson, M. Peterson, R. Freeman, *Science*, 2003, **299**, 1070.
4. S. Sakadzic, E. Roussakis, M. Yaseen et al, *Nature Methods*, 2010, **7**, 755-759.
5. W. Becker, *The bh TCSPC Handbook*, Fourth Edition, 2011.

SCANNING TOTAL INTERNAL REFLECTION FLUORESCENCE LIFETIME MICROSCOPY

V. Shcheslavskiy[1], **M. Kaiser**[2], **S. Pautot**[2], and **W. Becker**[1]

[1] Becker&Hickl GmbH, Nahmitzer Damm 30, 12277 Berlin, Germany
vis@becker-hickl.de
[2] Center for Regenerative Therapies, Technical University Dresden, 01062 Dresden, Germany

Introduction

The interest in the application of time-resolved fluorescence techniques for biomedical research has considerably grown for the last decade [1]. The fluorescence lifetime of a molecule is sensitive to numerous parameters, e.g. degree of aggregation or conformation, pH and temperature of the surrounding medium. Therefore, lifetime measurements are appropriate to probe the microenvironment of a fluorescent molecule. Fluorescence lifetime measurements combined with the techniques allowing getting high spatial resolution may deliver invaluable information [2] not accessible by other means. Lateral and axial resolution in fluorescence lifetime imaging (FLIM) has so far been in the range of hundred nanometers using either multiphoton microscopy or optical sectioning by a structured illumination technique. One of the ways to get improved axial resolution is to use evanescent waves for selective excitation of fluorophores residing in the close proximity of the coverslip interface. This is important to study, for example, protein-protein interactions, confined to a membrane of a cell and spectral properties of fluorophores adsorbed at the interface. We report on the development of a setup where FLIM is combined with scanning total internal reflection fluorescence microscopy (STIRF).

Methods

There are mainly two ways to generate evanescent field: a prism-based and objective-based approach. In both cases the objective lens is used to collect the emitted fluorescence. We use the second approach. The generation of the focused evanescent field is achieved by illumination of the back focal plane of the high NA objective with a ring, produced by an axicon lens (Fig. 1).

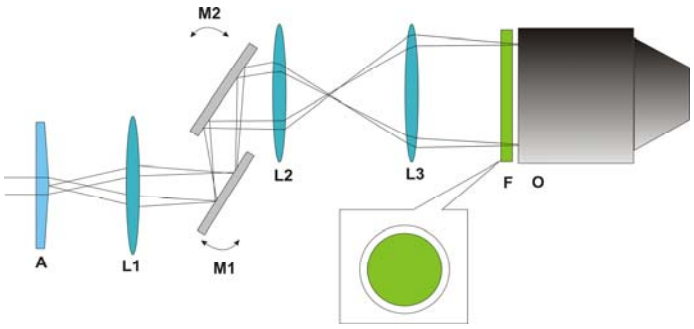

Fig. 1. Experimental setup. A: Axicon with an apex angle of 179^0; L1: lens, f = 300 mm; L2: scan lens, f = 40 mm; L3: tube lens: f = 200 mm; O: TIRF objective, Nikon APO 60, NA = 1.49; F: spatial filter

The advantage of using the axicon instead of a conventional beam stop is that all the power of the incoming beam is preserved in the ring. The inner radius of the beam was chosen so that the beam was incident at an angle, that exceeds a critical angle for total internal reflection:

$$\theta_c = \arcsin(n_1 / n_2), \quad (1)$$

where n_1 and n_2 are the refractive indices of the specimen and substrate, respectively. Careful spatial filtering allows to project a ring with a high contrast into the pupil plane (the scattered light from the apex of the axicon is filtered) and avoid stray light from illuminating the sample at angles below the critical angle. For excitation, 473 nm 50 ps diode laser (BDL-473-SMC) was used. The beam shaped with an axicon was sent to the bh DCS-120 confocal scanner. The detection was done in descanned mode with cooled PMT (PMC-100). The images were captured and recorded by time-correlated single-photon counting module SPC-150 [3].

Results

To evaluate the propagation length of the evanescent waves we imaged 5.2 μm diameter silica microspheres (Bangs Laboratories) coated with dioctadecylindocarbocyanine. Using the approach described in [4] we obtained the propagation distance of the evanescent wave of 140 nm. Similar results are obtained for 170 nm fluorescence polystyrene beads, deposited on a 170-μm-thick cover slide (Fig. 2).

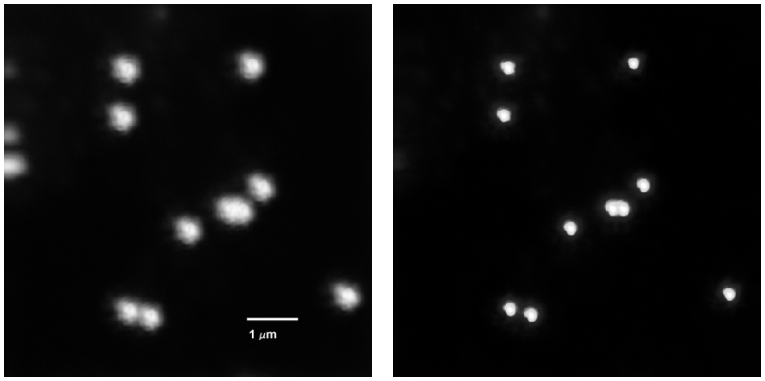

Fig. 2. Comparison of wide-field (left picture) and TIRF (right picture) images of 170 nm fluorescence beads

When the incidence angle on the sample is greater than critical angle, the illumination light will undergo total reflection. By contrast, when the incident angle on the sample is less than a critical angle, the illumination light enters the bulk of the sample and out-of-focus planes are illuminated, thus beads above focal plane become visible (Fig. 2, left picture). At the same time TIRF image allows to resolve two beads sitting together (Fig. 2, right picture). The lateral psf is non-symmetrical and slightly elongated in one direction, which is the result of illumination polarization.

To extend the scanning TIRF setup to the biological samples, we have made preliminary experiments on cultured Human Embryonic Kidney (HEK-293) cells (Fig. 3).

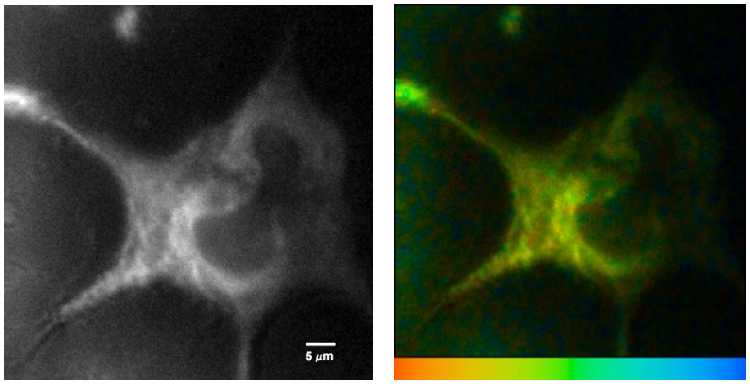

Fig. 3. TIRF picture of HEK-293 cells expressing Green Fluorescent Protein receptors. Left image: intensity distribution. Right image: lifetime image. The average lifetime is 1.85 ns with a standard deviation of 0.12 ns (6.5%). Average photon count rate is 80 kHz

In conclusion, we present an approach for implementing a scanning TIRF-FLIM experiment. We demonstrated that TIRF-FLIM can be easily obtained by adding external beam shaping optics to the existing confocal scanner and TCSPC FLIM module. This setup can be used for example to study protein-protein interactions at a cell membrane.

References

1. W. Becker, *Advanced time-correlated single-photon counting techniques*, Springer, Berlin, 2005.
2. E. Auksorius et al., *Opt. Lett.*, 2008, **33**, 113-115.
3. W. Becker, *The bh TCSPC Handbook*, Fourth Edition, 2011.
4. A. Mattheyses and D. Axelrod, *J. Biomed. Opt.*, 2006, **11**, 014006.

RECORDING LINEAR IN-WAVENUMBER SPECTRUM WITH SD-OCT WITHOUT RESAMPLING

V.M. Gelikonov, G.V. Gelikonov, A.A. Moiseev, D.A. Terpelov, and **P.A. Shilyagin**

Institute of Applied Physics RAS, "BioMedTech" LLC, Nizhny Novgorod, Russia; paulo-s@mail.ru

Methods of partial phase correction of registered optical spectrum for in-wavenumber linearization are described and investigated. A significant increasie of calculation speed in comparison with full resampling is shown. The experimental results for sample media are presented.

Fourier domain optical coherence tomography (FD OCT) is based on measuring optical spectrum of a sum of two interfering waves: the reference one and the wave backscattered from the object [1, 2]. The information about object's inner structure is reconstructed by inverse Fourier transform of optical spectrum. The Fast Fourier transform (FFT) is used to get maximized processing speed [3]. Using FFT has in mind strongly equally spaced (by argument) samples (in FD, OCT argument is optical frequency of receiving light). In real systems this equidistance is guaranteed only to limited accuracy [4, 5]. Recently a number of methods of correcting received spectra have been developed. Some methods are based on optical transformation of dispersion characteristics of the spectrometer by using an additional optical element [6, 7]. Other methods are based on using a graphics processor unit for fast resampling [8–10]. Unfortunately, the first methods do not allow compensating all dispersion nonlinear orders. The use of numerical methods results in a decreased maximal observation depth [7]. This paper is devoted to combined optical and numerical methods of spectral samples non-equidistance compensation in the spectral domain OCT (SD OCT).

Using a prism-compensator in spectrometer, one can decrease its nonequidistance by about 2 or 3 orders of magnitude. This allows reconstructing the scattering profile without widening of the maximum level of ½ in a discrete system [7]. But usually a logarithmic scale is used in OCT devices for visualization of the object structure – in this case the visible profile widening becomes significant (fig. 1 curve 1).

To avoid this problem, two modifications of a combined optical and numerical method for spectral samples non-equidistance compensation in SD OCT were developed.

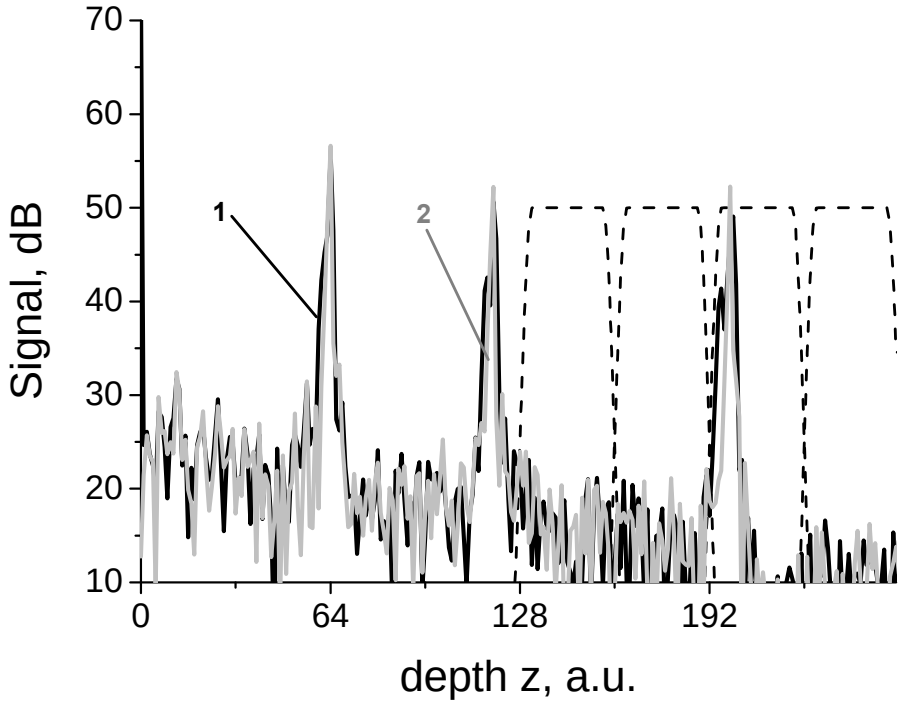

Fig. 1. A-profiles in SD-OCT. 1 – without correction; 2 – with correction. Dotted lines illustrate windows for dividing *z*-space series

For both modifications the information on integral dispersive characteristics is needed. It can be obtained from two (in linear approximation) measurements with single scatterer in object arm, located at two different depths. After DC component subtracting [11], the distribution of the interference phase over the optical frequency can be obtained. Then the real phase distribution for every depth $\varphi(\omega, z)$ can be calculated by solving a linear system of equations and any nonlinearity of this distribution can be compensated. Unfortunately, the direct calculations are time and labor consuming.

In the first modification, we divided the spectrum into a number of parts on the optical frequency scale. Every i-th part ($\omega_i < \omega < \omega_{i+1}$) was transformed by FFT and multiplied by a phase term increasing with depth. The value of phase for this term was obtained as the mean of $\varphi(\omega_i < \omega < \omega_{i+1}, z)$. These modified parts were used for construction of a new A-profile. The disadvantage of this modification is the presence of phase breaks over the optical scale, which could result in image destruction in the z-space.

In the second modification we divided the z-space series by windows as shown in fig. 1 by dotted curves. After the inverse FFT we multiplied the obtained filtered spectral series by a phase term increasing with depth. The value of phase for this term was obtained as the mean of $\varphi(\omega, z_i < z < z_{i+1})$. Since the dependence of phase on depth z is believed to be weak and linear, the number of steps can be not high. Combining these parts into a single corrected spectrum we obtain a corrected A-profile with minimal additional calculations.

Acknowledgements

This work was supported in part by the Ministry of Education and Science of the Russian Federation (contract of the Russian Federation No. 16.512.11.2002 dated 10.02.2011)

References

1. A.F. Fercher, C.K. Hitzenberger, G. Kamp et al., *Optics Communications*, 1995, **117**(1-2), 43.
2. M.A. Choma, M.V. Sarunic, C.H. Yang et al., *Optics Express*, 2003, **11**(18), 2183.
3. S.H. Yun, G.J. Tearney, J.F. de Boer et al., *Optics Express,* 2003, **11**(22), 2953.
4. M. Wojtkowski, R. Leitgeb, A. Kowalczyk et al., *Journal of Biomedical Optics,* 2002, **7**(3), 457.
5. W.A. Traub, *J. Opt. Soc. Am*., 1990, **7**(9), 1779.
6. Z. Hu, A.M. Rollins, *Opt. Lett.,* 2007, **32**(24), 3525.
7. V.M. Gelikonov, G.V. Gelikonov, P.A. Shilyagin, *Optics and Spectroscopy*, 2009, **106**(3), 459.
8. A. Bradu, S. Van der Jeught, D. Malchow et al., *in Proc. Optical Coherence Tomography and Coherence Domain Optical Methods in Biomedicine XV*, San Francisco, California, USA: SPIE, 2011. 78892E.
9. Y. Watanabe, T. Itagaki, *Journal of Biomedical Optics*, 2009, **14**(6), 060506.
10. S. Van der Jeught, A. Bradu, A.G. Podoleanu, *Journal of Biomedical Optics,* 2010, **15**(3), 030511.
11. V.M. Gelikonov, G.V. Gelikonov, I.V. Kasatkina et al., *Optics and Spectroscopy*, 2009, **106**(6), 895.

COMPLEMENTARY SINGLE-SHOT REGISTRATION OF FULL COMPLEX OPTICAL SPECTRUM IN SD-OCT

V.M. Gelikonov, G.V. Gelikonov and **P.A. Shilyagin**

Institute of Applied Physics RAS, "BioMedTech" LLC, Nizhny Novgorod, Russia, paulo-s@mail.ru

The goal of the research is improving a system for obtaining two different spectra in a single line of a linear CCD array.

Spectral domain optical coherence tomography (SD-OCT) is based on measuring an optical spectrum of a sum of two interfering waves: the reference one and the wave backscattered from the object [1, 2]. As the obtained spectrum is the real function of optical frequency, the image reconstructed by Fourier transformation has a mirror-symmetrical structure relative to zero path-difference [1]. Some methods of eliminating the mirror artifacts obtained for SD-OCT [3-6] are based on consecutive obtaining of spectral components with different phase shift between the reference and object waves. Simultaneous obtaining of full complex spectrum allows eliminating the influence of Doppler phase shifts caused by moving scatterers in the object [7, 8]. Simultaneous registration of quadrature interference components in spectrometer-based OCT by using a dual linear CCD array was proposed in [9]. The novel technique allows registering both quadrature components using an ordinary linear CCD array.

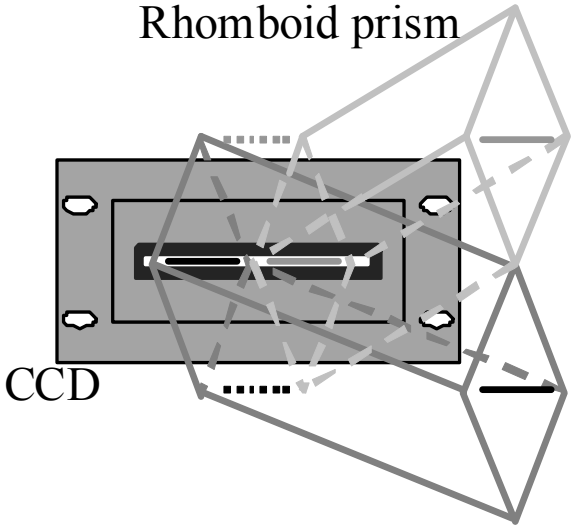

Fig. 1. Using rhomboid prisms for translation of two parallel lines into a single one

Using the principle described in [9], the reference beam is divided into two portions with different phase shifts. The beam dividing prism differs from that presented in [9] by increased prism angle. The diffracted beam after grating is focused by lens system to the CCD array. In the CCD plane the image corresponds to two spaced parallel lines. To translate these lines into one line, two rhomboid prisms are used. A schematic drawing of CCD linear array and rhomboid prisms setup is presented in fig. 1. Location of spectral images for dark and light lines in an ordinary setup is shown by dotted lines. The evident advantage of this setup in comparison with the one in [9] is a possibility of using ordinary linear CCD arrays and its insensitivity to insufficiently exact tuning of the angle between the projected lines and the CCD line.

The exact tuning of spectral images mutual location in the CCD plane is made by rotating rhomboid prisms.

Acknowledgements. This work was supported in part by the Ministry of Education and Science of the Russian Federation (contract of the Russian Federation No. 16.512.11.2002 dated 10.02.2011).

References

1. A.F. Fercher, C.K. Hitzenberger, G. Kamp et al., *Optics Communications*, 1995, **117**(1-2), 43.
2. M.A. Choma, M.V. Sarunic, C.H. Yang et al., *Optics Express*, 2003, **11**(18), 2183.
3. A.F. Fercher, R.A. Leitgeb, C.K. Hitzenberger et al., *in Proc. SPIE*, Stockholm, Sweden 1999, 173.
4. M. Wojtkowski, A. Kowalczyk, R. Leitgeb et al., *Optics Letters*, 2002, **27**(16), 1415.
5. R.A. Leitgeb, C.K. Hitzenberger, A.F. Fercher et al., *Optics Letters*, 2003, **28**(22), 2201.
6. P. Targowski, M. Wojtkowski, A. Kowalczyk et al., *Optics Communications*, 2004, **229**(1-6), 79.
7. M.A. Choma, C.H. Yang, J.A. Izatt, *Optics Letters*, 2003, **28** (22), 2162.
8. Zhao, Y.H., Chen, Z.P., Ding, Z.H. et al., *Optics Letters*, 2002, **27** (2), 98.
9. G.V. Gelikonov, V.M. Gelikonov, P.A. Shilyagin, *in Proc. Optical Coherence Tomography and Coherence Domain Optical Methods in Biomedicine XV*, San Francisco, California, USA: SPIE, 2011. 788925.

FLUORESCENCE CYSTOSCOPY, OPTICAL COHERENCE TOMOGRAPHY AND IMMUNOHISTOCHEMISTRY FOR DETECTION OF EARLY BLADDER CANCER

N.N. Prodanets[1], **L.B. Snopova**[1], **E.V. Zagaynova**[1], **O.S. Strelzova**[1], and **A.G. Orlova**[2]

[1] Nizhny Novgorod Medical Academy, Russia, lsnopova@gma.nnov.ru
[2] Institute of Applied Physics RAS, Nizhny Novgorod, Russia

Cancer of the urinary bladder is the second frequently met oncourological disease and the third one in mortality. Timely diagnosis of tumors of the urinary bladder and treatment of patients with this pathology is a difficult and significant problem of present-day oncology.

For optimization of diagnostic methods of recognition of early cancer of the urinary bladder the capabilities of combined application of fluorescent cystoscopy, optical coherence tomography (OCT) and immunohistochemistry were analysed. The best of domestic photosensitizes was selected for diagnostics. The choice was based on a possibility of intravesical introduction, high fluorescent activity and absence of photic toxicity; Alasens possessed the above characteristics [1].

A Karl Storz device with a xenon lamp with the wavelength of 430–480 nm was used for fluorescenne cystoscopy.

The time-domain OCT device created at the Institute of Applied Physics of the Russian Academy of Science (Nizhny Novgorod) was used in the research. A forward-looking OCT probe (2.7 mm in diameter) was used during the routine cystoscopic procedure: it was passed through the channel of the cystoscope and placed in contact with the mucosa. The compact OCT device utilizes low coherent radiation at 1270 nm wavelength and 1.5 mW optical power and has a spatial resolution of 10–20 μm. The penetration depth was close to1 mm with an acquisition time of 1.5 seconds for a 200x200 pixels image.

52 patients were investigated aiming at complex application of the fluorescent cystoscopy and optical coherence tomography for early detection of bladder cancer. The results obtained were verified by data of histologic analysis.

The fluorescence cystoscopy detected all areas of urinary bladder mucosa, which accumulated photosensitizer and fluoresced. Using the OCT during cystoscopic procedure it was possible to separate areas of malignant transformation in all fluorescent areas.

Special attention was given to the estimation of the OCT capability for verification of early cancer. Out of 163 flat fluorescent suspicious areas 150 were benign on histological data and, consequently, had false-positive fluorescence.

In 32 of 150 benign areas of the urinary bladder mucosa according to the OCT-data suspicious variants of images were obtained. These images demonstrated damage of the stratified structure or contrast of the border between the urothelium and underlying connective tissue. Consequently, 21% of the false-positive areas were also false-positive according to the OCT-data. 79% of the false-fluorescent areas were correctly recognized by the OCT as benign areas.

Thus, complex application of the fluorescent cystoscopy and optical coherence tomography, really enhance the quality of endoscopic diagnostics of early urinary bladder cancer. The sensitivity of the modern method of diagnosing urinary bladder cancer based on complex application of the fluorescence and OCT for flat suspicious areas of the urinary bladder mucosa was 86%, and the specificity was 79%. In the case of a major area of the fluorescence of the urinary bladder mucosa (chronic inflammation, squamous metaplasia) OCT allows objectively to detect the changes in these areas and preserve maximum of the mucosa during resection.

Proliferation marker Ki-67, cells cycle regulators p-53, p-63, cytokeratin 20, molecule adhesion CD44 v6, ABO(H) blood group antigen, and Thomsen-Friedenreich antigen were studied for assessing the capabilities of immunohistochemistry for verification of flat fluorescence zones. To the best of our knowledge, the mentioned antibodies have not been studied together, only separate markers were investigated for differential diagnostics of bladder tumor [2–6]. Meanwhile, they all have prognostic importance for early diagnostics of bladder cancer [2, 3, 4, 5, 6].

The markers were used in specimen tissues from the tumor and non-exophytic fluorescent zones. Ten patients had superficial forms of the urinary bladder cancer (16 non-exophytic fluorescent zones, 10 tumors).

Histological study of the non-exophytic fluorescent zones of the mucosa of the urinary bladder showed inflammation with uneven thinning of epithelium, plethora, edema, and diffusive inflammation infiltration.

In the non-exophytic fluorescent zones expression of Ki-67 and p-53 was temperate but high in tumors.

The expression of the cells cycle regulator p-53 was 41 % in the flat suspicions zones and 56 % in tumors.

In the tumor there was positive expression of the molecule adhesion CD44 v6 but in the flat suspicious areas there was diffusive staining of the cytoplasm of the epithelial cells.

The pathological type of the cytokeratin 20 expression was as in the non-exophytic fluorescent zones and in the tumor. But normal expression was in 25% of patients.

Loss of ABO blood group antigen expression was reported in transitional cell carcinoma of the urinary bladder. It was shown for 50% of noninvasive tumors. In the non-exophytic fluorescent zones positive staining on ABO dominated.

In the flat suspicious areas faint or negative expression of the Thomsen-Friedenreich antigen was revealed. The expression was always negative in the tumor.

Thus, immunostaining shows that in the non-exophytic fluorescent zones in patients with superficial forms of urinary bladder cancer the process of damage differentiation of the epithelial cells of urinary bladder are present in various degree. The character and the level of expression of all the studied biomarkers indicate the probability of neoplastic damages in urinary bladder mucosa. Hence, the presence of non-exophytic fluorescent zones on patients examination should be regarded to be suspicious and proper tactics of treatment must be selected.

Acknowledgements

This research was supported by the Russian Foundation for Basic Research (Project # 08-04-97098) with financial support of the Industry and Innovation Department of the Nizhny Novgorod Region.

References

1. E.G. Vakulovskaya, V.P. Letyagin, E.M. Pogodina, *Russian journal of biotherapy*, 2003, **2**, 57-60.
2. K.A. Iczkowski, J.H. Shanks, W.C. Allsbrook, et al., *Histopathology*, 1999, **35**, 150-156.
3. K.A. Iczkowski, J.H. Shanks, D.G. Bostwick, *Histopathology*, 1998, **32**, 322-327.
4. B.P. Matveev, K.M. Figurin, O.B. Karyakin, *Caner of urinary bladder*. Moscow, 2001.
5. Y. Chihara, K. Sugano, A. Kobayashi, et al., *Lab Invest.*, 2005, 85, 1051.
6. S.V. Petrov, N.T. Raihlin, *Handbook of immunohistochemical diagnostics of human tumors*. Edition 2, Kazan, 2000.

HIGH-FREQUENCY ACOUSTIC DETECTORS FOR PHOTOACOUSTIC TOMOGRAPHY

P.V. Subochev[1,2], **R.V. Belyaev**[1], **A. Morozov**[1], and **I.V. Turchin**[1,2]

[1] Institute of Applied Physics, Russian Academy of Sciences, Nizhny Novgorod, Russia,
[2] Nizhny Novgorod State Medical Academy, Russia
Pavel.Subochev@gmail.com

Photoacoustic imaging is a promising hybrid modality [1] which combines the advantages of optics and ultrasound. In comparison with pure optical methods, such as optical coherence tomography and optical diffuse tomography, the main advantage of photoacoustics is a higher spatial resolution for depths from several millimeters to few centimeters. As compared to pure acoustic methods, such as ultrasonography, the advantages of photoacoustics are high-contrast imaging of certain types of biological tissues (malignant tumors, blood vessels), as well as exogenously delivered contrast agents (gold nanoparticles, organic dyes, fluorescent proteins, etc. [2]).

In order to design a photoacoustic system one should use a laser delivering high power but non-ionizing laser pulses into biological tissue. Using multiple wavelengths of laser pulses enables one to differentiate acoustic pulses from different tissue chromophores. In our preliminary experiments we used a laser system based on tunable solid state LT-2214-PC and LS-2137/3 Q-switched pump lasers, both manufactured by the Belorussian company LOTIS TII, which were also used in photoacoustic systems of other authors [3]. Maximum pulse length of this laser system is 18 ns which corresponds to the spatial resolution limit of 28 μm at an average sound velocity in soft biological tissue 1.54 μm/ns. Therefore. transducers with >55 MHz are not expected to provide improved (<28 μm) spatial resolution when used with the described laser system.

The spatial resolution achieved by acoustic transducer with given frequency in the photoacoustic tomography depends on many parameters, such as reconstruction algorithm, physical properties of investigated tissue, mutual geometry of tissue and transducer, geometry of laser-tissue interface, and finally the piezo-mechanical properties of acoustic transducer itself in terms of its sensitivity and length of impulse response (the shorter the duration of impulse response for particular transducer, the greater is transducer's potential on spatial resolution). Thus, in order to construct a high sensitivity and resolution photoacoustic system one should use high sensitivity and short impulse response acoustic transducers.

In this study we analyzed two high-frequency acoustic transducers and compared them with three Panametrics transducers that were analyzed in the paper [4]. The first transducer that we tested was based on a $LiNbO_3$ crystal, it had 50 MHz resonance frequency, 3 mm diameter, and was spherically focused at 6 mm. The second transducer was based on PVDF material, had 30 MHz resonance frequency, 5 mm diameter and was spherically focused at 9 mm. Signals from both transducers were amplified using custom-made AD8099-based low-noise amplifiers.

In paper [4] impulse responses of different transducers were obtained by focusing short laser pulses on transducer surface. In order to add our transducers to the comparison, we used the same geometry of the experiment (fig. 1a). Typical A-scan data provided in fig. 1b and fig 1d, and as seen from aggregate pictures (fig. 1d and fig. 1f) a single laser shot on transducer surface generates RF-pulses with the resonant frequency of the transducer as a filling frequency. To compare transducers with different resonance frequencies, let us define the length of impulse response in arbitrary units as $N = T_{0.1} \cdot f$, where f is the resonant frequency of transducer in MHz, $T_{0.1}$ – the width of envelope at 10% amplitude level in μsec, so N would be the number of periods in impulse response. Maximum spatial resolution can be defined as $d = N \cdot c/f$, where c=1.54 μm/nsec is the speed of sound in soft tissue.

The sensitivity of two transducers can be compared using the recorded photoacoustic signals generated by a thin black-painted film (figs. 1e and 1f). To compare the sensitivity of two transducers let us use the Signal to Noise Ratio (SNR) parameter defined as $SNR = 20 \lg(A_1/A_2)$, where A_1 is peak signal value of photoacoustic signal and A_2 is standard deviation of noise. Finally, to compare maximum depth of photoacoustic diagnostics available for each transducer let us also use the following parameter $D = (SNR - 6\ dB)/(\alpha \cdot f)$, where D is maximum diagnostic depth, α = 0.54 dB/cm/MHz [5] is an ultrasound attenuation coefficient for soft biological tissue.

In Table 1 we present the measured parameters of our transducers compared to three Panametrics transducers analyzed in the paper [4]. Unfortunately, we did not have Panametrics transducers in our disposal nor were we able to find an etalon source of photoacoustic signal; therefore, we were not able to compare the sensitivity of all transducers in Table 1. However, we can conclude that PVDF transducer has characteristics better than $LiNbO_3$ for all analyzed parameters, such as spatial resolution, sensitivity and diagnostic depth. Therefore, we find PVDF to be a more promising base material for the photoacoustics measurements.

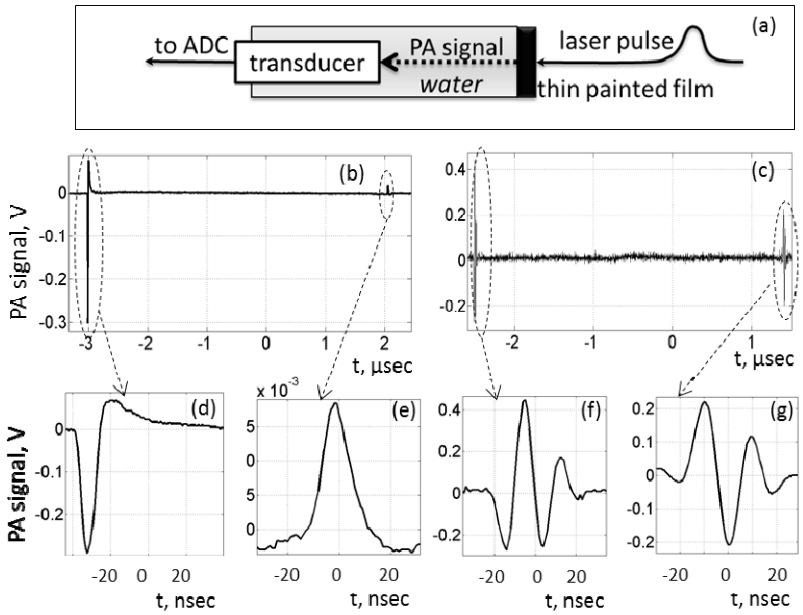

Fig. 1. Testing results for two high-frequency transducers.
(a) testing scheme, (b) A-scan data for PVDF-transducer (c) A-scan data for $LiNbO_3$-transducer (d) impulse response of PVDF-transducer after single laser shot on transducer surface, (e) PA signal measured by PVDF-transducer from thin painted film, (f) impulse response of $LiNbO_3$-transducer after single laser shot on transducer surface, (g) PA signal measured by $LiNbO_3$-transducer from thin painted film

Table 1. Joint comparison of acoustic transducers. Frequency, f. The length of impulse response, $T_{0.1}$. Number of periods in impulse response, $N = T_{0.1} \cdot f$. Relative spatial resolution, $d = T_{0.1} \cdot c$. Signal to noise ratio, SNR. Maximum diagnostic depth, D = (SNR–6dB)/($\alpha \cdot f$).

Transducers	f (MHz)	$T_{0.1}$ (µsec)	N	d (µm)	SNR (dB)	D (mm)
Panametrics V383[4]	3.5	0.7	2.45	1078	n/a	n/a
Panametrics XMS-310[4]	10	0.33	3.3	508	n/a	n/a
Panametrics V316-N [4]	20	0.17	3.4	262	n/a	n/a
PVDF-transducer	30	0.034	1.02	52	38	19.8
$LiNbO_3$-transducer	50	0.036	1.8	55	29	8.5

Acknowledgements

This work was partly supported by the Measures to Attract Leading Scientists to Russian Educational Institutions program and by the center for collective use of equipment Microwave and Laser Nanotechnologies.

References

1. H.F Zhang, K. Maslov, G. Stoica, and L.V. Wang, *Nature Biotechnology,* 2006, **24,** 848-851.
2. C. Kim, C. Favazza, and L.V.Wang, *Chemical Reviews*, 2010, **110**(5), 2756-2782.
3. W. Lu, Q. Huang, G. Ku, X. Wen, M. Zhou, D. Guzatov, P. Brecht, R. Su, A. Oraevsky, L.V. Wang, and C. Li, *Biomaterials*, 2010, **31**(9), 2617-2626.
4. G. Ku, X. Wang, G. Stoica, and L.V. Wang, *Phys. Med Biol.*, 2004, **49**, 1329-1338.
5. M.O. Culjat, D. Goldenberg, P. Tewari, and R.S. Singh, *Ultrasound in Medicine & Biology*, 2010, **36**(6), 861-873.

IMPROVED INTERFACE SYSTEM FOR SD-OCT WITH COHERENCE NOISE REDUCTION

V.M. Gelikonov, G.V. Gelikonov, D.A. Terpelov and **P.A. Shilyagin**

Institute of Applied Physics RAS, "BioMedTech" LLC, Nizhny Novgorod, Russia,
terpelov@ufp.appl.sci-nnov.ru

The work is devoted to developing the improved interface system (IS) for spectral-domain optical coherence tomography (SD-OCT) with coherent noise reduction. A compact and low-cost detection electronics scheme for SD-OCT is demonstrated. The efficiency of IS for the SD-OCT system is shown experimentally. An algorithm of exactly coherence noise reduction during lateral scanning is described.

Optical coherence tomography (OCT) is a technique capable of generating near-micron-scale images of structure in turbid media [1, 2]. In SD-OCT the resulting interference signal is spectrally dispersed and recorded by multiple detectors [3]. The individual spectral components of low coherence light are detected separately by means of a spectrometer and a charge-coupled device (CCD) array. Fourier transformation of this cross-spectral density yields a signal comprising several terms, including a component containing depth-resolved information on the structure of the backscattering sample and artifacts [4–6].

These artifacts are a strong DC signal, i.e. autocorrelation signal caused by the source light itself, the auto- and self-cross-correlated terms introduced by the reflections from various interfaces present in the optical system and the complex conjugate image [5, 7].

Our technique of these artifacts removing in SD-OCT is based on separate measurement of informative optical spectrum and artifacts. For this purpose the actual value of optical path difference should be precisely changed during exposition. The phase dependent term of interference between reference and sample waves is averaged during exposition while the path difference is modulated by a certain law [6]. So, the informative component in a registered spectrum is nulled (curve 1, fig. 1). It can be seen that after subtraction from the informative signal (curves 2, 3, fig. 1) of the signal received by such averaging method, we have a signal without autocorrelation terms and additional modulation caused by electrical circuit (curve 4, fig.1). Informative signal components (curves 2 and 3 in fig. 1) are used for complex field reconstruction aiming at eliminating conjugate artifacts.

We have developed a complex of electronic interface systems with coherent noise reduction for SD-OCT. These interface systems can be divided into 4 blocks: a block of controls and synchronization, a system of reading CCD-array, a control of optical path difference and a system of cross-section scanning.

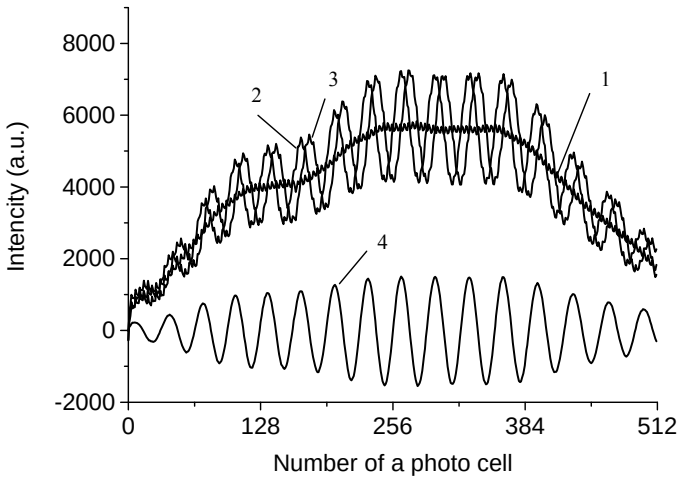

Fig. 1. Recorded spectrum. 1 – with modulation of optical path difference during exposition, 2 – without modulation, 3 – with relative delay into a quarter of length between reference and sample arms, 4 – result of subtraction (values 2 - values 1)

We have demonstrated a complex of interface systems for 1.3 μm SD-OCT that obtains diagnostic quality images at a rate of 40 fps (10,000 A-lines per second with 256x256 pixels) and can effectively eliminate complex conjugate images, DC noise terms, auto- and self-cross-correlation terms.

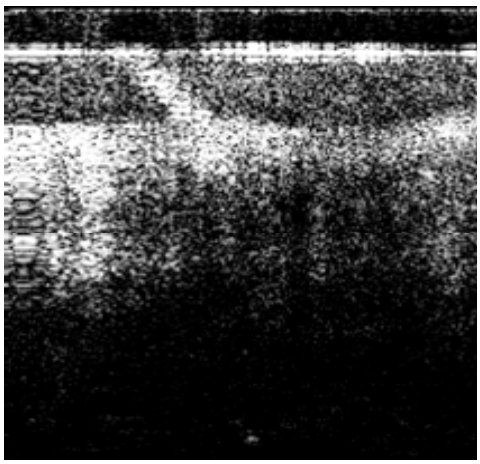

Fig. 2. Image of a human finger acquired *in vivo* with the SD-OCT system under the control of the developed interface system

The developed system setup was optimized for use in the OCT device produced by "BioMedTech" LLC. The system seems to be a base for a new generation of OCT devices.

Acknowledgements

This work was supported in part by FASIE (RF contract № 7379 p /10164 dated 28.12.2009) and the Ministry of Education and Science of the Russian Federation (RF contract № 16.512.11.2002 dated 10.02.2011).

References

1. D. Huang, E.A. Swanson, C.P. Lin, et al., *Science*, 1991, **254**, 1178-1181.
2. V.M. Gelikonov, G.V. Gelikonov, R.V. Kuranov, et al., *Pis'ma v ZhETF*, 1995, **61**, 149-153.
3. A.F. Fercher, C.K. Hitzenberger, G. Kamp, et al, *Opt. Commun*., 1995, **117**, 43-48.
4. S. Moon, S. Lee, W. Chen, *Opt. Express*, 2010, **18**(24), 24395-24404.
5. V.M. Gelikonov, I.V. Kasatkina, P.A. Shilyagin*, Radiophysics and Quantum Electronics*, 2009, **52**(11), 810-821.
6. V.M. Gelikonov, G.V. Gelikonov, I.V. Kasatkina*,* et al., *Optics and Spectroscopy*, 2009, **106**(6), 895-900.
7. Optical Coherence Tomography: Technology and Applications, Fujimoto J.G., Drexler W., Editors, Berlin, Springer, 2008, p. 177-207.

BACKSCATTERING ASSESSMENT DEVICE FOR CATARACT DIAGNOSTICS

E.R. Tkaczyk[1,2] and **K. Mauring**[1]

[1] Institute of Physics, Tartu University, 51014 Tartu, Estonia, etkaczyk@umich.edu
[2] Faculty of Medicine, Tartu University, 50411 Tartu, Estonia

Abstract

We present a diagnostic device to measure light scattering by the human eye lens, for assessment of cataract. Key elements include lock-in detection of backscattered light, a ring-shaped photodetector, and an ultrasonic distance meter.

1. Introduction: Motivation for quantitative cataract assessment

Cataract is a clouding of the eye's crystalline lens caused by aggregation of denatured proteins. Per World Health Organization statistics, cataracts currently are the reason for almost half of global cases of age-related blindness. The problem is becoming more acute as populations age; by the age of 75, over 90% of individuals exhibit age-related lenticular changes. Development of a portable, affordable device to quantitatively monitor cataract progression (Fig. 1) might permit cataract diagnosis at an early stage and assist in clinical studies of cataractogenesis and trials of disease-modifying treatments.

The device we are developing differs considerably from the current state of the art. Cataracts are traditionally diagnosed subjectively based on visual slit-lamp examination of the patient's eye by an experienced clinician. Although there are several grading systems available for discriminating the severity of disease, the diagnostic is inherently subjective. By contrast, we measure with a photodetector the fraction of light scattered backwards by the human lens when illuminated by a weak optical diode laser. As the signal arises directly from the fundamental pathology – increased scattering in the lens – it directly assesses cataract extent and progression. A more sophisticated related method is dynamic (quasi-elastic) light scattering (also known as photon-correlation spectroscopy), which follows temporal changes in and around random positions of scatterers [1]. This has previously yielded fundamental insight into ocular pathology by estimating the average size of particles in the interrogated region of the eye.

Fig. 1. Prototype device operated by a physician

2. Laser cataract assessment technology

Our apparatus comprises a modulated light source, ring-shaped photodetector, illumination optics, miniaturized lock-in detection electronics, and a distance meter (Fig. 2).

Ring-shaped photodetector: Previously, a stationary and bulky lens opacity meter has been manufactured by Interzeag [2] which measures scattered light at a single position, at a large angle

from the direction of the incident light. Due to masking by the human eye's iris, the device produced erroneous results for undilated patient eye pupils (less than 4 mm) [3]. A ring-shaped photodetector measuring the scattering light close to the optical axis of the eye should avoid this pitfall. This further ensures uniform detection over all azimuthal angles and detection in the region with most significant scattering (small angles).

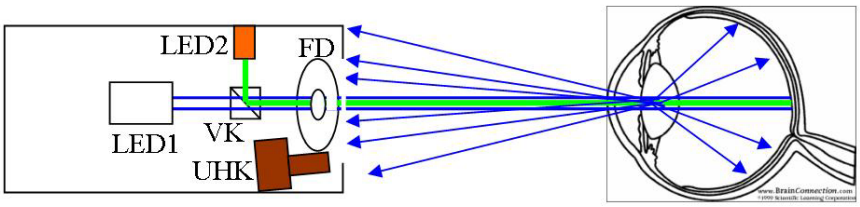

Fig. 2. Schematic of cataract assessment technology. LED1: Modulated light source. LED2: Gaze fixating light source. UHK: Ultrasound distance sensor. FD: Ring-shaped photodiode. VK: beam splitter. Scattering by cataractous lens is designated by thin arrows with arrowheads

Modulated light source and lock-in detection electronics: To enable operation with a sufficiently dim laser light to avoid discomfort to the patient, it is necessary to have a very sensitive scattered light detection scheme. This presupposes a photodetector with a very low dark current and low-noise amplifier. Additionally, the measurement should be independent of ambient light conditions. We therefore sinusoidally modulate the laser light of 650 nm and lock-in detect the amplified output of the ring-shaped photodiode. Optimized modulating and detection electronics are coordinated by a microcontroller inside of the device. In selecting the semiconductor laser and illumination optics, we have taken into account the cornea's small radius of curvature (ca 8 mm) and the divergence of the specularly reflected light that occurs when a parallel beam falls on it.

Ultrasonic distance meter: Measurement at a fixed distance between the photodetector and the patient's eye lens is essential to guarantee repeatability and accuracy. This is ensured by incorporation of an ultrasonic distance sensor which triggers measurement when the device is precisely positioned at a certain distance from the subject's cornea.

3. Conclusion

We anticipate that our efforts of miniaturization and costs reduction will result in a final product that fits easily into a physician's coat pocket and can subsequently be mass-produced at a cost of under $1000 per device.

Acknowledgements

We gratefully acknowledge support of Enterprise Estonia EAS grant ILOFY09016K as well as support of E.T. with a Fulbright Scholarship and a Whitaker Scholarship.

References

1. R. Ansari, *J. Biomed. Optics*, 2004, **9**, 22-37.
2. A.G. Interzeag, *European patent application*, EP 0231769, 1987.
3. M.P. Clark, J.C. Pearson, and J.C.Matthews, *British Journal of Ophthalmology*, 1990, **74**, 526-527.

HIGH PERFORMANCE ENGINE FOR 3D-VISUALIZATION AND RECONSTRUCTION OF VOLUMETRIC DATA IN BIOMEDICINE

V.E. Turlapov, **D.K. Bogolepov**, and **N.I. Gavrilov**

Lobachevsky State University of Nizhny Novgorod, Russia, vadim.turlapov@cs.vmk.unn.ru

Three-dimensional real-time visualization of experimental results with high spatial resolution is highly relevant to biomedicine, in general, and to biophotonics, in particular. Three-dimensional reconstruction of an object and manipulation of its parameters and properties in real-time is even more interesting. Biophotonics is characterized by high complexity of objects, and large amount of visualized data. For example, for the team of internationally acclaimed project Blue Brain [1] it is very important to have a biologically realistic model of neurons of rat cortical column and simulate them in real time. Rat's brain has about 100,000 columns each having about 10,000 neurons and 3×10^7 synapses. A mesh object of the reconstructed column (10,000 neurons) contains about 1 billion triangles and has a capacity of 100 GB. A model of columns, with the mapping of electrical activity has a capacity of 150 GB. One can get an insight into true complexity of rat's brain in the recent article of the Blue Brain team [2]. The human cortex may have as many as two million columns, each having of the order of 100,000 neurons. There are projects with a goal to bring biology object models down to the molecular level.

The same real-time problems we have for 3D visualization in electron, confocal, and multiphoton microscopy and in the 3D reconstruction of centimeter sized samples with a spatial resolution of several microns. The scientific community already perceived this problem and today we have the Open Microscopy Environment (OME) [3], which is a multi-site collaborative effort among academic laboratories and a number of commercial entities that produces open tools to support data management for biological light microscopy. Also, already the 12th Annual Bioinformatics Open Source Conference (BOSC 2011) sponsored by the Open Bioinformatics Foundation (O|B|F) will take place this year. There are a number of free special software products for 3D visualization in microscopy, such as ImageSurfer [4], and also 3D visualization software for each kind of microscopes. But often all of this does not work in real time in today's tasks. Also today we do not have software for 3D visualization of the volumes of data which are as large as 12 TB data of the mouse visual cortex [3].

This work presents a high performance engine and libraries for 3d-visualization, analyzing and reconstruction of volumetric data in biomedicine, oriented in perspective on huge sizes of data.

High performance engine for 3d-visualization

First of all this paper presents GPU-based implementation of the Direct Volume Rendering (DVR) method, included in the "InVols" visualization engine [5]. InVols provides new opportunities for scientific and biomedical visualization which are not available in due measure in similar software:

1) multi-volume rendering in a single space of up to 3 volumetric datasets determined in different coordinate systems and having sizes as big as up to 512x512x512 16-bit values;

2) performing the above process in real time on a middle class GPU, e.g. nVidia GeForce GTS 250 512 MB;

3) a custom bounding mesh for more accurate selection of the desired region in addition to the clipping bounding box;

4) simultaneous usage of a number of visualization techniques including the shaded Direct Volume Rendering via the 1D- or 2D- transfer functions, multiple semi-transparent discrete iso-surfaces visualization, MIP, and MIDA.

In the high performance DVR implementation we use such optimization strategies as *the early ray termination* and *the empty space skipping*. The clipping ability by custom 3D grid is also used as the *empty space skipping* approach to the rendering performance improvement.

We use the random ray start position generation and the further frame accumulation in order to reduce the rendering artifacts. The rendering quality can be also improved by the on-the-fly tri-cubic filtering during the rendering process. InVols supports 4 different stereoscopic visualization modes. Finally, we outline the visualization performance in terms of the frame rates for different visualization techniques on different graphic cards.

A volume rendering performance of the InVols obtained on different graphic cards for: screen resolution – 1280x1024; 16-bit dataset of size 512x512x512; the ray step – 0.2 of the voxel size; and the viewpoint used in Fig. 1c is outlined in Table 1.

Table 1. Visualization performance for different rendering techniques in terms of frame rates (fps). *Isos* means visualization of three semitransparent isosurfaces

GPU	DVR + Isos	Isos	MIP	DVR	Opaque iso-surface
NVIDIA GeForce GTS 250	9	10	10	12	30
NVIDIA GeForce 9500 GT	4	4	4	5	13
NVIDIA Quadro FX 5600	14	16	19	23	63
ATI Radeon HD 4870	18	21	35	38	81
ATI Radeon HD 4890	21	25	39	44	108

Figure 1 shows examples of real-time visualization via InVols.

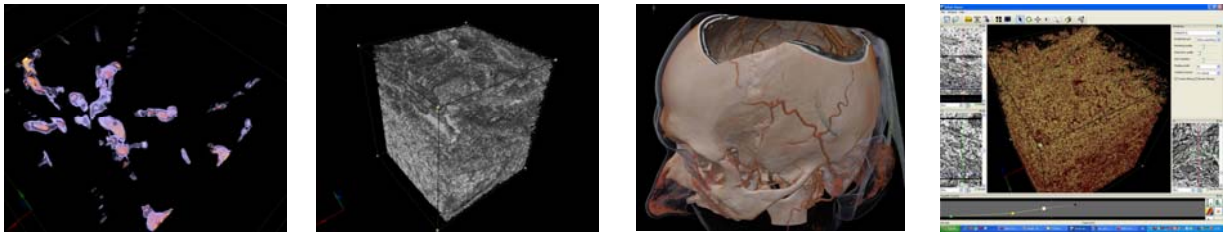

a b c d

Fig. 1. a) One frame of migrating macrophages in response to stimuli (800x800x30 px), 4D data set from Dirk Sieger and Francesca Peri, EMBL; b) 3D visualization for a part (4x4x10 μm => 512x512x210 px) of volume 12T B data of mouse visual cortex [6] accessible via [7]; c) 3D visualization for CT of a human head; d) interface of the program

Our software applications and libraries have also:

- Means of data segmentation for the 3D geometric reconstruction of different shells and blood vessels, separation of the bones in the joints, etc.
- Means of automated initial diagnosis from the diagnostic images and tomograms.
- Means to restore the three-dimensional geometric models of organs and humans in general in order to bind all the diagnostic data to a single 3D model and to add the functional modeling.
- Means of photorealistic real-time visualization of the complex biomedical objects as polygonal dynamic scenes on the GPU (real time for 10^7 triangles).

Acknowledgements

This work was supported by the Federal Program "Research and Research and Teaching Staff of Innovative Russia", State Contract No. 02.740.11.0839.

References

1. Official site of the Blue Brain Project (http://bluebrain.epfl.ch/).
2. S. Romand, Y. Wang, M. Toledo-Rodriguez, & H. Markram, "Morphological development of thick-tufted layer V pyramidal cells in the rat somatosensory cortex. [Original Research], *Frontiers in Neuroanatomy*, 2011, **5**.
3. Official site of the Open Microscopy Environment (OME, http://openmicroscopy.org).
4. ImageSurfer -Free 3D imaging software to visualize and analyze multi-channel volumes/ official site (http://imagesurfer.cs.unc.edu).
5. InVols Viewer. Free software for biomedical and scientific visualization (http://ngavrilov.ru/invols).
6. Official site of Open Connectome Project (http://openconnectomeproject.org/), 450x350x50 cubic micron volume of mouse visual cortex with spatial resolution of 4x4x45 cubic nanometers (resource).
7. S. Saalfeld, A. Cardona, V. Hartenstein, and P. Toman˘cák, "CATMAID: collaborative annotation toolkit for massive amounts of image data", *Bioinformatics*, 2009, **25**(15), 1984-1986.

Invited

NON-DESTRUCTIVE STEM CELL TRACKING IN HAIR FOLLICLES OF LIVING MICE

A. Uchugonova[1,2,3], R. Hoffman[1,3], M. Weinigel[4], and **K. Koenig[2,4]**

[1] Dept. of Surgery; University of California San Diego, San Diego, CA
[2] Dept. of Biophotonics and Laser Technology, Saarland University, Saarbruecken, Germany
[3] AntiCancer Inc., San Diego, CA;
[4] JenLab GmbH, Jena, Germany

In stem cell research there is a high demand for non-invasive imaging techniques that allow observation of stem cells under native conditions without significant input on cell metabolism, reproduction, and viability. Easy accessible hair follicle pluripotent stem cells in the bulge area and dermal papilla are potential sources for stem cell based therapy. It has been shown that these cells are able to generate hair, non-follicle skin cells, nerves, vessels, smooth muscles etc. and may participate in wound healing processes.

We report on the finding of nestin-GFP expressing stem cells in their native niche in the bulge of the hair follicle of living mice by using high-resolution *in-vivo* multiphoton tomography. The 3D imaging with submicron resolution was based on two-photon induced fluorescence and second harmonic generation (SHG) of collagen. Migrating stem cells from the bulge to their microenvironment have been detected inside the skin during optical deep tissue sectioning.

This method is non–invasive and helps to understand functional activity, migration behavior, and differentiation of stem cells by *in-vivo* monitoring of single stem cells in their native environment during new tissue generation and wound healing.

Material and Methods

Nestin-GFP transgenic nude mice, with GFP expression driven by the nestin promoter [nestin-driven GFP (ND-GFP)] were used for imaging. Mice were anesthetized by 30 µl ketamine solution and imaged with multiphoton tomography.

The multiphoton tomograph MPT*flex*™ (JenLab GmbH, Jena, Germany) uses a sealed turn-key tunable 80 MHz titanium: sapphire femtosecond laser (710 - 920 nm, 250 fs). The optical unit consists of an active optical power attenuator to regulate the *in situ* power of the laser in dependence on tissue depth and an active beam stabilization device. The scan head consists of a fast galvo-scanning device to generate 2D (XY) scans, a piezodriven z-scanner, and high NA focusing optics (NA 1.3). The optical arm is stabilized with a mechanical arm. The scan head also contains a dual photon detector unit for the measurement of autofluorescence and second harmonic generation (SHG).

Results and Discussion

In previous studies, we demonstrated the presence of nestin-expressing multipotent stem cells in the bulge area and dermal papilla of the hair follicle by multiphoton imaging [1, 2]. By long-term observation we were able to monitor non-synchronized behavior of nestin-expressing stem cell population of the isolated hair follicles during different stages of the hair growth and during skin wounding to the damaged skin side[2]. It has been shown that hair follicle stem cells have high potential to generate melanocytes, osteoblasts as well as neurons, blood vessels, and smooth muscle cells etc[1] in vitro conditions.

Multiphoton tomography allows non-destructive long-term analysis of living cells due to the absence of out-of-focus absorption, out-of-focus photobleaching, and out-of-focus phototoxicity[4].

Multiphoton excitation of endogeneous fluorophores is possible with a single near infrared (NIR) laser excitation wavelength due to broad multiphoton absorption bands of multiple fluorophores such as NADPH and green fluorescent proteins (GFP). During *in vivo* imaging, cellular autofluorescence (keratin, NAD(P)H, melanin, and elastin) was detected at different NIR excitation wavelengths (750 nm, 790 nm, 930 nm) in order to separate different native fluorescent molecules in the skin of ND-GFP transgenic mice and control mice. Intracellular GFP was very efficiently excited at 930 nm by two-photon effects with a fluorescence maximum of 520 nm. Extracellular matrix protein-collagen was detected at 790 nm excitation with a BP 395 nm due to the second harmonic generation signal of the collagen structure. However, optical sections with submicron resolution, based on

autofluorescence or two-photon excited GFP, as well as SHG of collagen can be obtained simultaneously with a excitation wavelength 790 nm (Fig. 1). 3D fluorescence imaging provided information on the morphology and size of the stem cells as well as enabled visualization of some cell structures and extracellular matrix components with submicron resolution (Fig. 1). 2-15 mW mean power was used to excite fluorophores in dependence on the depth of the skin tissue. Optical sections have been generated as deep as 300 µm in overall field-of-view of 350 x 350 μm^2 with an acquisition time 2 s for one optical section.

The hair follicles of four-week old nude mice have a typical lateral dimension of 50 µm and a depth of 200 µm and more [3]. GFP-expressing nestin stem cells have a diameter about 7 µm and with long extrusions (Figure 1) and found to be located at typical depths of 30-60 µm below the sebaceous glands and the hair bulb at depths of 150 µm and deeper [3]. The typical thickness of the epidermis was found to be 30-40 µm [3]. Therefore, high-resolution multiphoton tomography of the upper part of the hair follicles including the hair bulge in living mice was possible.

The movement of individual stem cells was recorded during long-term imaging with submicron resolution.

Conclusion

Hair follicle stem cells can be imaged non-invasively within their natural environment. Long–term in vivo monitoring helps to understand functional activity, migration behavior, and differentiation of stem cells during new tissue generation, wound healing and other environmental triggers.

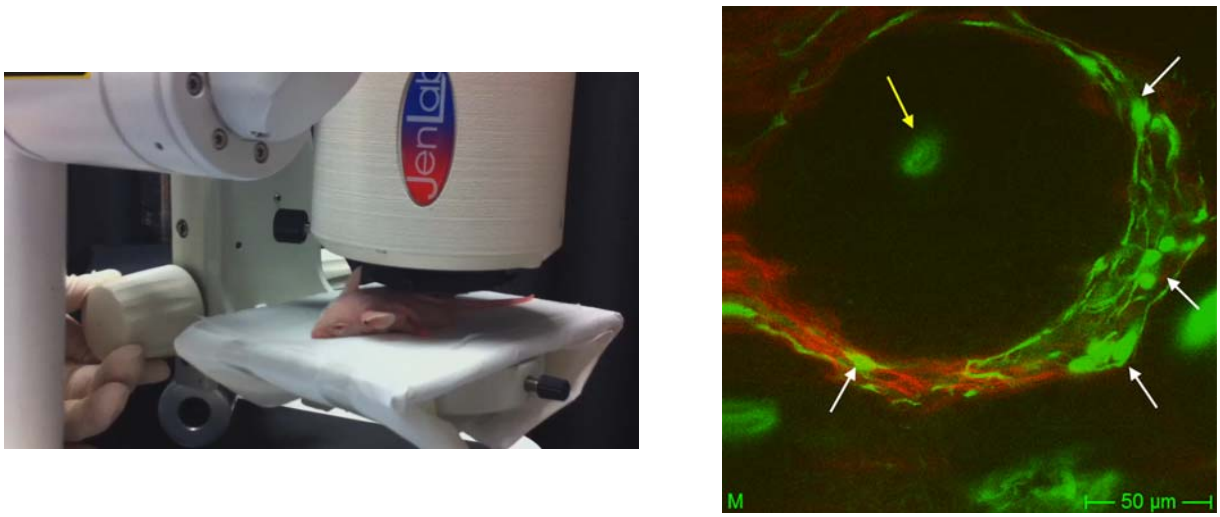

Fig. 1. Left: High resolution *in vivo* imaging of the skin with the Multiphoton Tomograph MPTflex™. Right: One optical section of the skin with one hair follicle of nestin–GFP expressing nude mouse. Hair shaft imaged by autofluorescence (yellow arrow), extracellular matrix collagen imaged by SHG signal (red color) and GFP imaged by two-photon excitation (green). White arrows demonstrate nestin-GFP stem cells in the bulge area of the hair follicle. Excitation wavelength 790 nm used to image autofluorescence, GFP and SHG signal simultaneously

References

1. F. Liu, A. Uchugonova, H. Kimura, C. Zhang, M. Zhao, L, Zhang, K. Koenig, J. Duong, R. Aki, N. Saito, S. Mii, Y. Amoh, K. Katsuoka, R.M. Hoffman, *Cell Cycle*, 2011, **5**, 830-9.
2. A. Uchugonova, J. Duong, N. Zhang, K. König, R.M. Hoffman, *J. Cell Biochem*., 2011, doi: 10.1002/jcb.23122.
3. A. Uchugonova, M.R. Hoffman, M. Weinigel, K. Koenig, *Cell Cycle*, 2011, **10**(12).
4. K. König, "Clinical multiphoton tomography", *J. Biophotonics*, 2008, **1**, 13-23.

FLUORESCENT ANALYSIS OF EXCITATION POTENTIALS GENERATION IN HIGHER PLANTS

V.A. Vodeneev[1], **E.K. Akinchits**[1], **L.A. Orlova**[1], and **I.V. Balalaeva**[1,2]

[1] N.I. Lobachevsky State University of Nizhny Novgorod
603950 Gagarin St., 23, Nizhny Novgorod, Russia; *kbf@unn.ru*
[2] Institute of Applied Physics of RAS
603950 Ulyanov St., 46, Nizhny Novgorod, Russia

The ability to generate and to extend excitation potentials is an unique property of all living creatures and higher plants in particular. It is connected with a need of translation the signal about external irritation from one part of an organism to it's another part. So research of the action potential generation and promotion properties appeared to be essential [1]. However, the process of action potential generation is better studied in animal cells and in giant alga cells. It first of all may be connected with some methodical problems. Higher plants cells have a comparatively small size, are integrated in complex structure of tissues and organs and owing to plasmodesms connecting them between each other, form the single electroconducting structure – symplast [2, 3]. One of the approaches allowing study of the nature of excitation potentials on the whole plants is use of fluorescent probes which allow to register ion concentration shifts with simultaneous recording of electrical activity. Use of fluorescent probes or proteins for analysis of nature of excitation potentials in plants was performed only in occasional works [4].The goal of the present work was analysis of applicability of the fluorescent analysis method for study of ion mechanisms of AP and VP generation in higher plants.

Materials and Methods

Objects of study were the 3-4-week seedlings of pumpkin Cucurbita pepo L. In this part of the work we studied participation of plasmatic membrane proton pump in AP and VP generation. As criteria of plasmatic membrane proton pump activity changes we used changes of apoplastic pH. Changes of pH were recorded with aid of pH-sensitive probe of fluorescein isothiocyanate probe (FITC) connected with molecule of dextran (FITC-dextran) (Hoffman, Cosegarten, 1995). Dependence of the FITC-dextran fluorescence parameters on pH value was determined by recording of the fluorescence and excitation spectra in buffer solutions (Tris-MES, 20 mM) with different pH values (from 4.5 to 8 with step of 0.5 unit). The fluorescence was recorded using a Shimadzu RF-5301 PC spectrofluorimeter. An increase of the fluorescence intensity (I) corresponded to a shift towards the alkaline side. The maxima of excitation and emission were not shifted.

To load the plant with the probe, at a site of the stem, from two sides, a strip of epidermis, about 1 cm in length and about 2 mm in width, was removed and immersed into the solution containing 10^{-3} M KCl, $5 \cdot 10^{-4}$M $CaCl_2$, $5 \cdot 10^{-4}$M NaCl, and $5 \cdot 10^{-7}$M FITC for 12—18 hours. Before performance of measurements, the plant stems were washed with flow water for removal of the probe from the surface. Fluorescence of the whole plant was recorded on a complex of laser scanning microscopy – an Axiovert 200M inverted microscope, a Carl Zeiss LSM 510 laser scanning module, and a Zeiss 23 META scanning module. Simultaneously with recording of fluorescence, electrical activity was recorded. This activity was recorded extracellularly by (Ag/AgCl) macroelectrodes. The measuring electrode was located in the zone of recording of fluorescence; the comparison electrode was in contact with the root-washing solution. The AP generation was produced by a local cooling – a drop of ice water was placed onto the stem at several centimeters more acropetal to the zone of recording of fluorescence. VP was induced by a damaging action in the form of burn of the cotyledon leaf with open flame.

Results and discussion

On the obtained images of plants loaded with the probe, it is clearly seen that fluorescence in the range of 500-550 nm is located in the intercellular space (fig. 1). Based on this, it can be concluded that the used here fluorescent probe FITC-dextran is selectively accumulated in apoplast.

To study dynamics of cell wall pH at the AP generation on the initially obtained 3D-image, the individual optical section was chosen, which corresponded to the third or fourth cell layer from the

surface, and determined fluorescence intensity in time from the chosen areas. Application of stimulation producing propagation of AP whose generation is accompanied by a transient enhancement of fluorescence, the kinetics of both processes being very close (fig. 2). The revealed fluorescence intensity changes indicate that at the AP generation there occurs the transient alkalization of apoplast on the background of AP depolarization that is replaced by acidification to the level close to the initial one at the repolarization phase.

A change of the apoplast pH was also revealed at propagation along the stem of VP induced by burn of the cotyledon leaf (data are not presented). Like in the case of AP, the apoplast pH changes had the reverse character; however, duration of alkalization was essentially higher and corresponded well to the longer development of the repolarization phase characteristic of AP (Julien., Frachisse, 1992, Rousset et al, 2002).

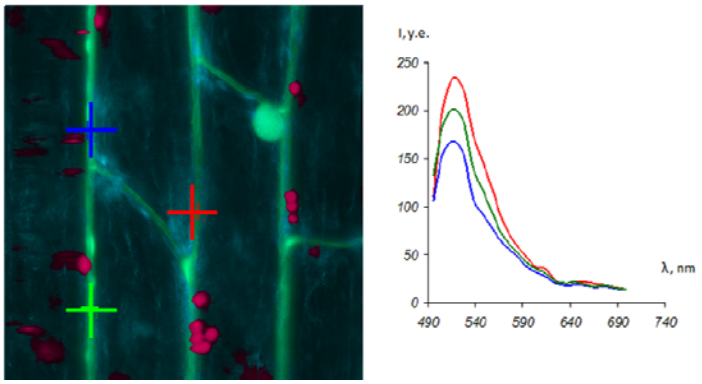

Fig. 1. Localization of FITC-dextran in apoplast. Markers show point from which fluorescence specters have been registered

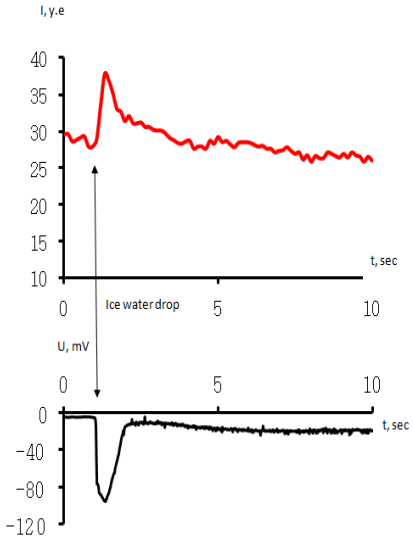

Fig. 2. Change of fluorescence intensity of FITC-dextran, loaded into plant stem at AP generation

The obtained results on changes of pH of cell walls indicate the following sequence of events: during the depolarization phase, protons enter the cell from apoplast, which causes its alkalization; at the repolarization phase there occurs their transfer from cell to apoplast, which leads to return of pH to values close to the initial ones. Such development of events can take place if there occurs the transient inhibition of proton ATPase – inactivation at the impulse depolarization phase and reactivation at the repolarization phase. The successful application of this method for analysis of the apoplast pH changes indicates the possibility of its use for study of dynamics of concentrations of other ions.

Acknowledgements

The work is supported in part by the Russian Foundation for Basic Research (project 09-04-97085) and by the Federal Agency of Science and Innovations (GK № 02.740.11.0086).

References

1. J. Fromm, S. Lautner, *Plant Cell Environ*., 2007, **30**, 249-257.
2. T. Shimmen, T. Mimura, M. Kikuyama, M. Tazawa, *Cell Struc. Funct*., 1992, **19**, 263-278.
3. M.J. Beilby, *Int. Rev. Cytol*., 2007, **257**, 43-82.
4. J. Fisahn, O. Herde, L. Willmitzer, H. Pena-Cortes, *Plant Cell Physiol*, 2004, **45**, 456-459.
5. B. Hoffman, H. Cosegarten, *Physiol. Plant*., 1995, **95**, 327-335.
6. J.L. Julien, J.M. Frachisse, *Can. J. Bot.,* 1992, **70**, 1451-1458.
7. M. Rousset, M. de Roo, J.-Y. Guennec, O. Pichon, *Physiol. Plant*., 2002, **115**, 197-203.

PROGRESS IN BIOMEDICAL APPLICATIONS OF TERAHERTZ TECHNOLOGY

V.P. Wallace

School of Physics, University of Western Australia, Crawley, 6009, Australia
vincent.wallace@uwa.edu.au

Introduction and Background

Microscopic imaging methods used in histopathology provide structural and functional information from preserved tissue specimens, whereas current medical imaging methods like MRI and CT provide images of living tissues at the macroscopic level, but at much lower resolution and specificity.

High-resolution *in vivo* subsurface imaging of tissue would provide the best information for the early detection of disease but such techniques are not yet available. One of the biggest unsolved problems in medical imaging is how to combine macroscopic and microscopic imaging advances so that, for example, the precise margins of cancers can be delineated [1]. Many new optical technologies have the potential to bridge this resolution/function gap, but as yet very few are in routine clinical use. A contributing factor is that a single technique may not provide enough information for clinical use, e.g. it is difficult to differentiate cancer from scarring using optical coherence tomography (OCT).

Eighty-five percent of cancers originate in the epithelial tissues [2] that form the external and internal surface structures of the body. It is widely accepted that in most cancers early detection is essential for long-term survival and, thus, there is a need to improve the detection of pre-cancers and small early cancers. There is also a need to improve the surgical removal of tumours by accurately locating tumour margins, especially in the case where conservation of normal tissue is essential, as in breast or brain surgery. An increasing amount of work is focussing on THz imaging of healthy and cancerous breast tissues [3, 4], where it is hoped that it may be possible to develop an intra-operative tool to aid in the conservation of healthy issue during the removal of tumour tissue [5].

Terahertz

Terahertz radiation is non-ionising and has the capability to penetrate a wide variety of non-conducting materials such as clothing, paper, cardboard, wood, plastics and ceramics, but is strongly absorbed by polar molecules, such as water, and reflected by metals [6]. THz imaging and spectroscopy is currently being developed for use in medical imaging [7, 8]. The first demonstration of biomedical THz imaging [9] concluded that a distinction could be made between porcine muscle and fat with the hypothesis that the difference in water content of the two materials was responsible for the contrast. Water is one of the main constituents of biological tissue: penetration depths range from typically a few hundred microns in high water content tissues to approximately a centimetre in tissues with a high fat content [10].

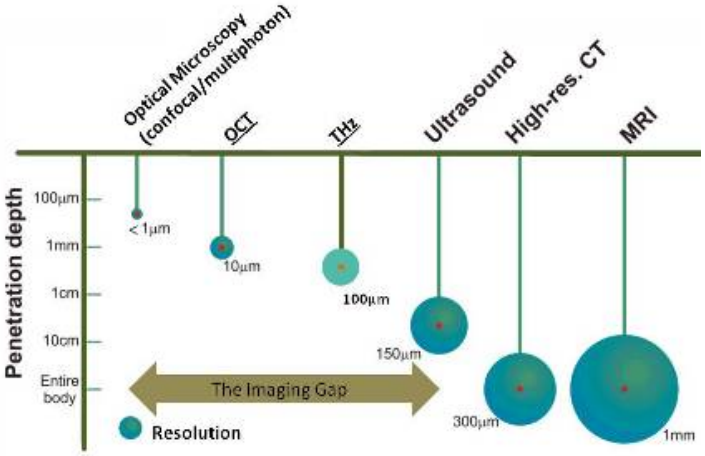

Fig. 1. Can we bridge the microscopy-medical imaging gap with and THz technologies? Disease normally manifests via large-scale symptoms: tumours, deformities, lesions; but it has a microscopic and molecular basis. Early detection depends on microscopic/molecular diagnosis, often advantageous to perform *in situ*

Since the first demonstration, the number of reported biomedical studies using THz imaging has increased greatly to include teeth and artificial skin models [11] healthy skin and basal cell carcinoma both *in vitro* and *in vivo* [12, 13], excised breast tumours [14], cortical bone [15] and burns [16].

THz images of tumours show good contrast between diseased and normal tissues [13, 14] and THz spectroscopy studies have also found significant differences between the tissues' optical properties [4, 17]. In a recent study we have shown that THz spectroscopy is capable of recovering material composition [18]. Continued technological advances in the field which increase the output power and SNR of the systems may enable improved tissue identification in the future. We conclude that there is indeed a role for novel technologies to fill gaps in medical imaging (Fig. 1), which include THz or a combination of THz with other modalities. THz can be added to the arsenal of techniques that clinicians can use to battle disease.

References

1. W. Hendee, "And now for the next 20 years", in *Physics World*. 2008, Institute of Physics: Bristol. 54.
2. V. Backman and J.A. McGilligan, "Detection of preinvasive cancer cells", *Nature*, 2000, **408**(6811), 428-428.
3. A.J. Fitzgerald, V.P. Wallace, M. Jimenez-Linan, L. Bobrow, R.J. Pye, A.D. Purushotham, D.D. Arnone, "Terahertz pulsed imaging of human breast tumors", *Radiology*, 2006, **239**, 533–5409.
4. P.C. Ashworth, E. Pickwell-MacPherson, E. Provenzano, S.E. Pinder, A.D. Purushotham, M. Pepper, V.P. Wallace, "Terahertz pulsed spectroscopy of freshly excised human breast cancer", *Opt. Express*, 2009, **17**, 12444-12454.
5. P.C. Ashworth, P.O'Kelly, A.D. Purushotham, S.E. Pinder, M. Kontos, M. Pepper, V.P. Wallace, "An intraoperative THz probe for use during the surgical removal of breast tumors", *Infrared, Millimeter and Terahertz Waves*, 2008, IRMMW-THz 2008. 33rd International Conference on 1–3 (2008).
6. V.P. Wallace, E. MacPherson, J.A. Zeitler, and C. Reid, "Three-dimensional imaging of optically opaque materials using nonionizing terahertz radiation", *J. Opt. Soc. Am. A*, 2008, **25**(12), 3120-3133.
7. E. Pickwell-MacPherson and V.P. Wallace, "Terahertz pulsed imaging-a potential medical imaging modality?", *Photodiagnosis and Photodynamic Therapy*, 2009, **6**(2), 128-134.
8. E. Pickwell and V.P. Wallace, "Biomedical applications of terahertz technology", *J. Physics D: App. Phys*, 2006, **39**, R301-R310.
9. B.B. Hu and M.C. Nuss, "Imaging with terahertz waves", *Opt. Lett*., 1995, **20**(16), 1716-1718.
10. D.D. Arnone, C.M. Ciesla, A. Corchia, S. Egusa, M. Pepper, J.M. Chamberlain, C. Bezant, E.H. Linfield, R. Clothier, and N. Khammo, "Applications of terahertz (THz) technology to medical imaging. *Proc. SPIE*, 1999, **3828**(1), 209-219.
11. A.J. Fitzgerald, E. Pickwell, V.P. Wallace, A. Purushotham, S. Pinder, M. Linan, R. Pye, and T. Ha, "Medical applications of broadband terahertz pulsed radiation", *Lasers and Electro-Optics Society*, 2005. LEOS 2005. The 18th Annual Meeting of the IEEE, pp. 120-121, 2005.
12. R.M. Woodward, B.E. Cole, V.P. Wallace, R.J. Pye, D.D. Arnone, E.H. Linfield, and M. Pepper, "Terahertz pulse imaging in reflection geometry of human skin cancer and skin tissue", *Physics in Medicine and Biology*, 2002, **47**, 3853-3863.
13. V.P. Wallace, A.J. Fitzgerald, S. Shankar, N. Flanagan, R.J. Pye, J. Cluff, and D.D. Arnone, "Terahertz pulsed imaging of basal cell carcinoma ex vivo and *in vivo*", *Brit J. Derm.*, 2004, **151**, 424-432.
14. A.J. Fitzgerald, V.P. Wallace, M. Jimenez-Linan, L. Bobrow, R.J. Pye, A.D. Purushotham, and D.D. Arnone, "Terahertz pulsed imaging of human breast tumors", *Radiology*, 2006, **239**(2), 533-540.
15. M.R. Stringer, N.D. Lund, A.P. Foulds, A. Uddin, E. Berry, R.E. Miles, and A.G. Davies, "The analysis of human cortical bone by terahertz time-domain spectroscopy", *Physics in Medicine and Biology*, 2005, **50**, 3211-3219.
16. Z.D. Taylor, R.S. Singh, M.O. Culjat, J.Y. Suen, W.S. Grundfest, H. Lee, and E.R. Brown, "Reflective terahertz imaging of porcine skin burns", *Opt. Lett.*, 2008, **33**(11), 1258-1260.
17. V.P. Wallace, A.J. Fitzgerald, E. Pickwell, R.J. Pye, P.F. Taday, N. Flanagan, and T. Ha, "Terahertz pulsed spectroscopy of human basal cell carcinoma", *Appl. Spectrosc.*, 2006, **60**(10), 1127-1133.
18. C.B. Reid, A.P. Gibson, J.C. Hebden, J.G. Laufer, E. Pickwell-MacPherson, and V.P. Wallace, "Spectroscopic capabilities of THz reflection measurements for medical imaging", *Physics in Medicine and Biology* (Accepted 28th June 2010).
19. Y.W. Sun, B.M. Fischer, E. Pickwell-MacPherson, "Effects of formalin fixing on the terahertz properties of biological tissues", *J. Biomed. Optics*, 2009, **14**(6), 1083-3668.

LABEL-FREE FLUORESCENCE MICROSCOPY OF GLIOBLASTOMA CELLS WITH DIFFERENT MALIGNANCY

P. Weber[1], **M. Wagner**[1], **P. Kioschis**[2], and **H. Schneckenburger**[1]

[1] Hochschule Aalen, Institut für Angewandte Forschung, Beethovenstr. 1, 73430 Aalen, Germany
petra.weber@htw-aalen.de
[2] Hochschule Mannheim, Institut für Molekular- und Zellbiologie, Paul-Wittsack-Strasse 10
68163 Mannheim, Germany

In label-free diagnostics of cells and tissues, measurements of intrinsic fluorescence revealed to be promising. Presently, autofluorescence spectra, decay kinetics and images of U251-MG glioblastoma cells prior and after activation of tumor suppressor genes are compared. Differences are observed upon excitation by near ultraviolet light when fluorescence ratios between the protein bound and the free coenzyme NADH depend on the state of malignancy. Additional information is obtained from intensity images, spectral images and fluorescence lifetime images (FLIM).

Introduction

Measurements have been used increasingly for early diagnosis of cancer in various organs (e.g. bronchus, colon, bladder, lung or skin) [1]. However, a comparison between tumor cells and less malignant cells revealed to be difficult, so far, due to the lack of comparable cell lines. In this case, this difficulty was circumvented by use of so-called isogenic cells with switchable tumor relevant genes. When exited by near ultraviolet light, autofluorescence of the coencymes nicotinamid adenine dinucleotide (NADH) as well as flavin mono- and dinucleotid (FMN/FAD) seems to play an important role, since it reflects their state of oxidation and, consequently, cell physiology [2]. For this reason, we combined spectral and time resolved methods as well as corespondending images.

Materials and Methods

Experiments were carried out with genetically engineered U251-MG glioblastoma cells kindly supplied by Prof. Jan Mollenhauer, Dept. of Molecular Oncology, University of South Denmark, Odense. In two subclones, of those U251-MG glioblastoma cells, the tumor suppressor genes TP53 or PTEN were overexpressed using a Tet-On inducible expression system. In this case, cells show reduced tumorigenic characteristics, like slow groth in contrast to the control cells with inactive tumor suppressor genes. These control cells are unaltered malignant and present distinctive features of cancer cells. Cells were seeded in at a density of 100 Zellen/mm^2 and cultivated for 24 h until the induction with doxicyclin, and another 48 h at 37°C and 5% CO_2 as monolayers on glass slides in DMEM supplemented with fetal calf serum, antibiotics and hygromycin.

For microscopic measurements, a wide-field microscope (Axioplan 1, Carl Zeiss Jena, Germany) was used with a 375 nm Picosecond laser diode (LDH 375 with driver PDL 800-B, Picoquant, Berlin, Germany; pulse energy: 12 pJ, pulse duration: 55 ps, repetition rate: 40 MHz) for fluorescence excitation. Fluorescence was detected at $\lambda \geq 415$ nm (using a long pass filter). Fluorescence images were recorded with 63x/0.90 water immersion objective lens and an electron multiplying (EM-)CCD camera (DV557DC, ANDOR Technology, Belfast, U.K.) with Peltier cooling and a sensitivity below 10-16 W/pixel. This camera was replaced by an image intensifying camera system (Picostar HR 12 image intensifier coupled to a cooled CCD camera; La Vision, Göttingen, Germany) triggered by the laser diode for fluorescence lifetime measurements with a time resolution of 200 ps.

Results and Discussion

Prior and after activation of tumor suppressor genes autofluorescence spectra, decay kinetics and images of U251-MG cells are compared. Particularly with regard to excitation by 375 nm, all spectra are dominated by broad bands with maxima around 440-450 nm and 470-490 nm, which have previously been attributed to protein-bound and free NADH as depicted in Figure 1. The fluorescence ratio of the protein bound and free coenzyme NADH gives evidence of the state of malignancy. Obviously, the short wave band is more pronounced for the cells with activated tumor suppressor gene than for the malignant control cell.

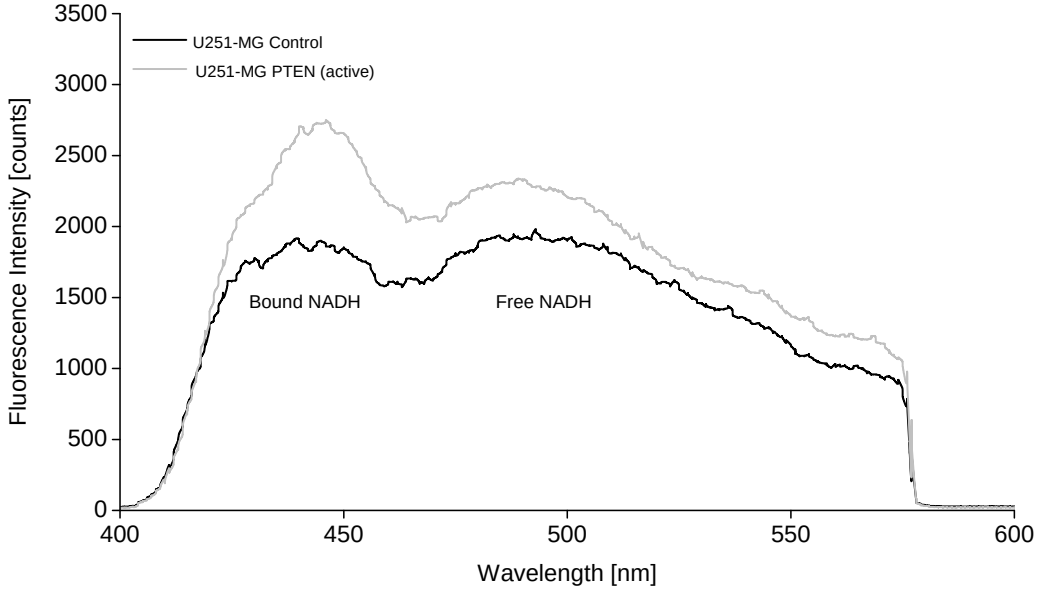

Fig. 1. Autofluorescence spectra of U251-MG cells (control and cell with activated suppressor gene PTEN); excitation wavelength: 375 nm). The two broad bands are representative for bound and free NADH

These effects were further evaluated with multivariate data analysis. For spectral imaging, we are using two additional interference filters for 450 ± 20 nm and 490 ± 20 nm to measure in different spectral ranges and determined a protein binding parameter $PBP = (I_{450} - I_{490}) / (I_{450} + I_{490})$ [3]. We observed small differences in granules around the cell nucleus.

Furthermore we compared fluorescence decay kinetics as well as fluorescent lifetime imaging (FLIM) of control cells and cells with activated tumor suppressor genes TP53 or PTEN. While the fluorescence lifetime of these activated cells are showing a tendency to longer lifetimes in comparison to the control cells, these findings were confirmed with lifetime images. In this case, we find again shorter lifetimes around the cell nucleus, possibly indicating an increasing amount of free NADH. When combining these measurements, it seems that these are promising parameters to distinguish tumor cells and less malignant cells of the same genotype.

Acknowledgements

This project is funded by the Bundesministerium für Bildung und Forschung (BMBF; grant no. 17 92C 08) and Baden-Württemberg-Stiftung gGmbH. Skilful technical assistance by C. Hintze is gratefully acknowledged.

References

1. T. Galeotti, GD. van Rossum, D.H. Mayer and B. Chance, *Eur J Biochem*., 1970, **17**(3), 485-496.
2. B. Banerjee, B. Miedema and HR. Chandrasekhar, *Am J Med Sci*., 1998, **3167**(3), 220-226.
3. H. Schneckenburger, P. Weber, M. Wagner, M. Brantsch, P. Biller, P. Kioschis, W. Kessler, *Proc. SPIE*, Bellingham, 2011, Vol. 7902.

FLUORESCENT TUMOR ANIMAL MODELS AS A PERSPECTIVE TOOL FOR ANTICANCER DRUG TESTING

V.V. Zherdeva[1], **L.R. Arslanbaeva**[1], **M.M. Shchigreva**[1], **I.G. Meerovich**[1], **A.L. Rusanov**[1], **T.V. Ivashina**[2], **L.M. Vinokurov**[3], and **A.P. Savitsky**[1]

[1] Bach Biochemistry Institute RAS, Moscow, Russia, vjerdeva@inbi.ras.ru
[2] Institute of Biochemistry and Physiology of Microorganisms RAS, Pushchino
[3] Branch of the Institute of Bioorganic Chemistry RAS, Pushchino

Introduction

Modern trends in treatment of tumor diseases are to develop targeted drugs with minimal side effects. A lot of modern antitumor drugs either known and new chemo or targeted drugs start the programmed cell death, apoptosis. To assess the validity of new antitumor drugs, one of the determining factors is the activation of enzymes of apoptosis in particular caspase-3.

When using the fluorescent genetically encoded FRET- sensors it is possible to track activation of caspase *in vivo*. In such a models cleavage of enzyme specific fragment like DEVD lead to the change in fluorescent signal intensity which could be measured.

This study is devoted to getting of fluorescent tumor models encode fluorescent proteins (FP) and FP-based sensor of caspase -3, monitoring and detection of caspase activity *in vivo* by the methods of fluorescence molecular imaging.

Materials and Methods

The prokaryotic plasmids encoded red fluorescent protein TagRFP and fluorescent substrate for caspase-3 TagRFP- 23-KFP on the base of pair red fluorescent proteins.

TagRFP and KFP linked with 23 a.a. including DEVD fragment were developed in our laboratory.

Lentiviral particle containing TagRFP-23-KFP (TR23K) and TagRFP (TR) were obtained from Evrogen (Russia) and used for transfection of human lung adenocarcinome A549, human larynx carcinome Hep-2 and ductal breast carinome HBL-100.

Transduced cells ($1 \cdot 10^6$ in 100 μL) were inoculated subcutaneous to *nude* mice in order to obtain xenograft tumor models expressing constructions above.

Established subcutaneous models were characterized by different fluorescent techiniques including epifluorescense (iBox Spectra Imaging System (UVP, USA), laser spectrometry (SpectrCluster (Cluster Ltd, Russia)), fluorescence diffuse tomography (DFT-3(IAP RAS, Russia).

The animal models for drug testing were *nude* mice with grafted tumors A549-TR23K and A549-TR. Taxol was administered with 8 days of tumor growth for 5 days every day in a concentration of 15 mg/kg. Etoposide was administered with 8 days of tumor growth for 5 days every day in a concentration of 12 mg/kg.

Inhibition of tumor growth was estimated by palpation and by fluorescence method. Caspase activation was estimated as the ratio o fluorescence intensity in the control to experiment.

Processing of the fluorescence images was performed using the program Vision Works (UVP, USA), and NIH Images J.

Resutls and Disscussion

Previous study of caspase-3 genetically encoded substrate TagRFP- 23-KFP *in vitro* showed the presence of FRET beween TagRFP and KFP [1]. Cleavage of caspase-3 specific DEVD fragment was demonstated both *in vitro* and on transduced cells by FLIM [2].

The transduced cell lines were study for their responsiveness to apoptosis inductors *in vitro*. Sensitivity to anticancer drugs was expressed as a percentage, the number of dead cells to the total number of cells in the control group. Cell line Hep-2 demonstrated the most sensitive to etoposide (88%), doxorubicin (86%) taxol (82%), cell line A549 – doxorubicin (89%), taxol (75%) etoposide (60%), cell line HBL-100 – to etoposide (97%), doxorubicin (90%) taxol (83%). The caspase activation was detected at least as twofold increase of fluorescent signal of TagRFP in the TR23K cell models. Also the caspase activation were confirmed by commercial caspase-3 detection kits.

Tumor animal model A549-TR remains the ability of expressing RFP for the month in an amount more than sufficient for detecting fluorescence *in vivo*. The tumor growth well correlated with the TagRFP- fluorescent signal intensity Inhibition of tumor growth were estimated by fluorescence decrease as 30% от the 15-16-th days after initiation of treatment. This approach allows tracking the tumor growth in depth, as well as assessing the initial stages of tumor regression without apparent reduction of tumor nodes after treatment.

A549-TRK23 model was characterized by the initial level of fluorescence signal of about 30% of the fluorescence A549-TagRFP. In the treatment of etoposide the caspase activation efficacy was about 1.2- fold increase comparing to untreated control. In the treatment of taxol the caspase activation efficacy was about 2-fold increase comparing to untreated control. Inhibition of tumor growth in both cased was about 30%. Iincrease in life expectancy of treated of animals was not obtained.

If fluorescence in the model A549-TR decreases due to the inhibition of its growth, in the case with the model A549-TRK23 fluorescence increases due to the cleavage of genetically encoded substrate of caspase-3, which in turn would initiate the launch of apoptosis *in vivo*. In a series of experiments on the detection of apoptosis *in vivo* in a model A549-TRK23 was demonstrated an increase in caspase activity under the action of antitumor means more for taxol (2.2–2.3-fold) and to a lesser extent to etoposide (1.2-fold*). In vitro* these inducers cause the death of about 60-70% of the cultivated cells. These differences in the effect *in vivo* can be explained by peculiarities of the pharmacokinetics of drugs, limitations associated with the type of transplantation of xenografts, as well as the degree of tumor vascularization.

Conclusions

Fluorescent subcutaneous tumor models of lung adenocarcinoma A549, expressing the protein TagRFP and genetically encoded substrate of caspase-3 TRK23 (caspase sensor) in *nude* mice were obtained and characterized. It was shown that changes in the level of fluorescence can be monitored tumor growth and development, inhibition of tumor growth and, most importantly, evaluate activation of caspase-3 that may be useful for preliminary assessment of the effectiveness of anticancer drug.

Acknowledgements

This study was supported by grants No. 02.512.12.2036 and No. 16.512.11.2137 from the Federal Agency for Science and Innovation.

References

1. A.L. Rusanov, T.V. Ivashina, and A.P. Savitsky, *Proc. II International symposium Topical problems of biophotonics*, Nizhny Novgorod, 2009, p. 11.
2. A.L. Rusanov, T.V. Ivashina, L.M. Vinokurov, I.I. Fiks, A.G. Orlova, I.V. Turchin, I.G. Meerovich, V.V. Zherdeva, and A.P. Savitsky, *J. Biophotonics*, 2010, **3**(12), 774-783.